Developing a Numerical Inverse-Theory-Based Extraction of Orientation-Dependent Relaxation Rates from Partially-Relaxed Spectra

by

Mohammad Sedigh Ghamari

A THESIS SUBMITTED IN PARTIAL FULFILMENT OF
THE REQUIREMENTS FOR THE DEGREE OF

MASTER OF SCIENCE

in

The Faculty of Mathematics and Sciences

Department of Physics

BROCK UNIVERSITY

October 19, 2009

In presenting this thesis in partial fulfilment of the requirements for an advanced degree at the Brock University, I agree that the Library shall make it freely available for reference and study. I further agree that permission for extensive copying of this thesis for scholarly purposes may be granted by the head of my department or by his or her representatives. It is understood that copying or publication of this thesis for financial gain shall not be allowed without my written permission.

(Signature) _____

Department of Physics

Brock University
St.Catharines, Canada

Date _____

Abstract

Second-rank tensor interactions, such as quadrupolar interactions between the spin-1 deuterium nuclei and the electric field gradients created by chemical bonds, are affected by rapid random molecular motions that modulate the orientation of the molecule with respect to the external magnetic field. In biological and model membrane systems, where a distribution of dynamically averaged anisotropies (quadrupolar splittings, chemical shift anisotropies, *etc.*) is present and where, in addition, various parts of the sample may undergo a partial magnetic alignment, the numerical analysis of the resulting Nuclear Magnetic Resonance (NMR) spectra is a mathematically ill-posed problem. However, numerical methods (de-Pakeing, Tikhonov regularization) exist that allow for a simultaneous determination of both the anisotropy and orientational distributions. An additional complication arises when relaxation is taken into account. This work presents a method of obtaining the orientation dependence of the relaxation rates that can be used for the analysis of the molecular motions on a broad range of time scales. An arbitrary set of exponential decay rates is described by a three-term truncated Legendre polynomial expansion in the orientation dependence, as appropriate for a second-rank tensor interaction, and a linear approximation to the individual decay rates is made. Thus a severe numerical instability caused by the presence of noise in the experimental data is avoided. At the same time, enough flexibility in the inversion algorithm is retained to achieve a meaningful mapping from raw experimental data to a set of intermediate, model-free

parameters suitable for further analysis in terms of specific kinds of molecular motions such as vibrations, flexing, kink and jog deformations, *etc.*

Contents

List of Tables

List of Figures

Acknowledgements

First, I would like to express my heartfelt gratitude to my supervisor Prof. Edward Sternin who patiently guided me through this research and generously offered his help whenever it was needed. Without his constant support I wouldn't have been able to accomplish this project. I also wish to thank my supervisory committee members Prof. David A. Crandles and Prof. Kirill Samokhin for their guidance and counseling over the course of this project.

I'm greatly indebted to my teachers Prof. Shyamal K. Bose, Prof. Thad Harroun, Dr. Anton Knigavko, and once again Prof. Kirill Samokhin for all things I learned from them during my Master at Brock University. My academic life at Brock wouldn't have been that enjoyable without the kind help of Frank Benko and Elizabeth Horvath. Also, I wish to thank all my friends at Brock and in particular Ivana Komljenovic for all her helps and for proof reading this thesis and Mojtaba Hajialamdari for his helpful advises.

Last but not the least, I wish to express my deepest gratefulness to my father and my aunts for all their support, encouragement, and patience during these years. Their guidance and wisdom has always helped me overcome difficulties.

Chapter 1

Introduction

Nuclear Magnetic Resonance (NMR) spectroscopy is a powerful and flexible analytical tool in exploring microscopic properties of matter. NMR is capable of detecting molecular motions and interactions through their effect on the macroscopic net nuclear magnetization of the sample. Since nuclei have almost no effect on electron clouds and chemical bonds in a molecule, detecting molecular motions and interactions by NMR is expected to produce no or negligible perturbation. In addition, because the magnetogyric ratio of a nucleus is several orders of magnitude smaller than that of an electron (*e.g.*, $\gamma_H = 267.51 \times 10^6 \text{rad s}^{-1} T^{-1}$ or $\gamma_D = 41.064 \times 10^6 \text{ rad s}^{-1} T^{-1}$ versus $\gamma_e = -1.76 \times 10^{11} \text{ rad s}^{-1} T^{-1}$ [1, 2]), nucleus-nucleus and nucleus-electron interactions such as the dipole and quadrupole couplings are much weaker than electron-electron interactions. As a result, according to Heisenberg energy-time uncertainty principle, the time required to determine the energy associated with these nucleus-nucleus and nucleus-electron interactions is much longer than the time required to detect electron-electron interactions. This lower bound on the duration of the detection of interactions sets forth an intrinsic time scale for NMR spectroscopy known as *NMR time scale*, τ_M [3].

The significance of a longer time scale becomes clear once disordered and partially ordered systems are to be dealt with, wherein all interactions are subject to extensive thermal fluctuations. Molecular tumblings with long correlation times compared to the NMR time scale result in an ensemble averaged and hence, a broad spectrum. On the other hand, fast motions, which are designated as motions with correlation times much shorter than the NMR time scale, translate into averaged interactions with sharply determined observables. Spectroscopically, this means having shifts in the position of resonance peaks as the indication of modified interactions rather than changes in spectral line widths. The advantage of NMR over other similar spectroscopies is in the fact that the NMR time scale is typically longer (for instance $\tau_M \approx 6 \times 10^{-6}\, s$ in ^{2}H NMR) than most molecular motions. The resulting fast motion averages of tensorial interactions such as the quadrupole interaction, manifested in NMR spectral parameters such as splittings and relaxation rates, contain valuable information about the molecular structure and dynamics that may not be directly accessible otherwise [4, 5, 6, 7].

Interpreting and mapping obtained spectra to microscopic properties of the sample is the ultimate goal and, at the same time, the most challenging task in any spectroscopy. This is particularly true in case of disordered and partially ordered materials where simplifications based on various symmetries like those of periodic

crystals or totally random, isotropic liquid like systems are unavailable. NMR is one of the few spectroscopic techniques available wherein not only qualitative interpretation of spectra but also, in principle, quantitative analysis on the basis of fairly simple and manageable interaction models is possible [8]. However, in practice the presence of experimental noise superimposed on spectra over the course of data acquisition poses a serious difficulty in quantitative interpretation of the spectra [9].

Solid state NMR, as opposed to solution NMR, is a branch of NMR spectroscopy that primarily deals with anisotropic systems. It has proven to be particularly useful in studying soft condensed matter systems such as polymers, liquid crystals, proteins, and lipid membranes which are typical examples of partially ordered, anisotropic systems. These materials neither posses perfect periodic structure of crystals nor totally random structure of liquids. This heterogeneity in structure and order imparts unique properties to these materials and makes them very susceptible to order-disorder interplay that dictates their organization. Studying lipid membranes is one of the areas that solid-state NMR has been extensively used in examining the structure and dynamics of lipids in membranes, due to its capability of discriminating order from disorder [10].

1.1 Lipids in Biological and Model Membranes

Lipids are the main component of cell membranes in all living organisms. A cell membrane not only contains the cell and separates it from the outside environment but also is a medium through which the cell can function and interact with the outside world. According to the current view of cell membranes known as *fluid mosaic model*, the functioning of biological systems critically depends on membrane microfluidity [11] which, in turn, is closely related to dynamical and structural properties of constituent lipid molecules in the membrane. Despite the fact that cell interactions with their environment often involve specific receptor proteins on their membranes, there are many fundamental cell phenomena which are membrane-based and mostly dependent on the micro-mechanical properties of the membrane. These include anesthesia [12], antimicrobial effect of some bactericides [13], and the effect of cholesterol on the cell membranes. Even the conformation of embedded receptor proteins, a crucial factor in their functioning, is closely related to the mechanical properties of the membrane such as pressure profile and rigidity.

Lipids are amphiphilic molecules (Fig. 1.1) , that is, they have a hydrophilic polar headgroup and hydrophobic apolar fatty acid chains. Because of this structural heterogeneity, lipid molecules in aqueous dispersions prefer to form aggregations with the least exposure of the hydrophobic chains to water. This preference leads to a self-assembly phenomenon and the spontaneous formation of lipid aggregations with various topologies and thermodynamical properties. The topology and thermodynamic phase of these aggregates critically depends on the lipid molecule properties such as chain length or headgroup charge, and on thermodynamical parameters such

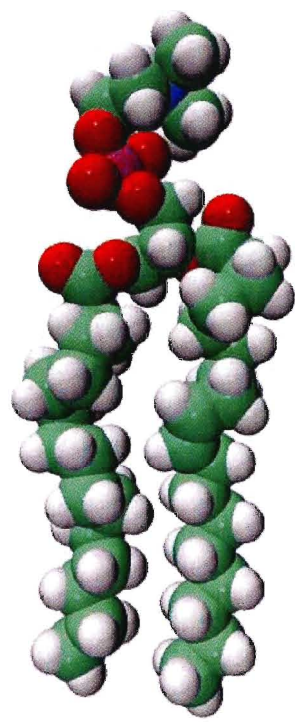

Figure 1.1: **POPC lipid molecule** (1-palmitoyl-2-oleoyl-sn-glycero-3-phosphocholine) Green spheres represent carbon atoms and white spheres are hydrogens. Reproduced from [14].

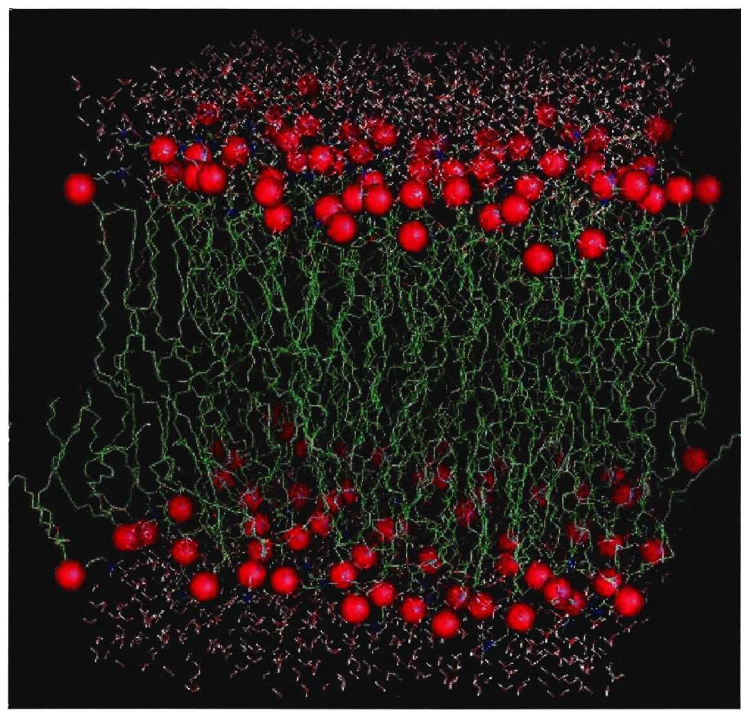

Figure 1.2: **Lipid bilayer** A portion of a lipid membrane. Reproduced from [15].

as temperature, concentration of lipids, hydration, pressure, and ionic strength. The introduction of any additive capable of affecting the process of lipid aggregation such as another lipid molecule with different chain length or headgroup charge, other amphiphilic molecules (*e.g.,* cholesterol), *etc.,* can promote significant modification in the structural phase of the membrane. When water is abundant in aqueous dispersions, lipids typically organize themselves in a lamellar structure with hydrophilic headgroups on either sides of the bilayer and hydrophobic chains in between (Fig. 1.2). Other structural arrangements (hexagonal-packed cylinders, cubic phase, *etc.*) are also possible.

Depending on temperature and other thermodynamical parameters, liquid bilayers may also exhibit different *thermodynamic* phases with different dynamical properties. At low temperatures where the van-der-Waals attraction between hydrocarbon chains is dominant, lipid chains are rigid and ordered. This state of the lipid aggregation is referred to as the *gelphase* (L_β) or solid ordered (s.o.) phase. Under biological conditions, where thermal fluctuations are strong enough to overcome the van der Waals

attraction but yet too weak to overcome hydrophobic and hydrophilic forces, lipids form a *lamellar liquid crystal* (L_α) or liquid ordered (l.o.) phase. Transition from the gelphase to the liquid-crystal phase significantly increases inter- and intramolecular motions and lipids' freedom. In L_α phase lipid molecules are free to diffuse laterally just like a 2D liquid [16]. Also, in this phase, across the bilayer there exists a characteristic order profile such that chain segments away from the headgroups are more free (and less ordered) [17]. In general, the more extensive fluctuations at segments close to the free end of the fatty acid chains of lipids result from the cumulative effect of motions in above segments that affect not only those segments but also the rest of the chain. In contrast, the end of the chain attached to the glycerol backbone is constrained by the massive headgroup and experiences less motional freedom.

A variety of modes of motion can occur in a lipid membrane in the lamellar liquid crystalline phase. The most common ones are the following [17]:

- Rotation around C-C bond that occurs about the long axis of hydrocarbon chains. Because it requires less energy than other modes it is the fastest mode of motion with the time scale on the order of 100ps.

- cis-kinks in hydrocarbon chains have a lifetime about 10 times longer than the time scale of rotation around the C-C bond, of the order of 1ns.

- Lipid molecules bending (flexing) is another possible mode of intramolecular motions (Fig. 1.3) .

- Rotational diffusion, which is the rotation of the entire lipid molecule including the headgroup about its long axis, can also occur with the correlation rate of $2\pi/10$ns.

- Lateral diffusion in membranes, which is the most important mode of motions from the biological point of view, in essence is similar to Brownian motion in 2D. It is a process well-described by a series of "jumps" of the lipid molecule from one vacancy in the liquid crystalline lattice to another. The rate of these jumps is about $10^7\,\mathrm{s}^{-1}$ to $10^8\,\mathrm{s}^{-1}$ with a diffusion constant of $\sim 10^{-7}\mathrm{cm}^2\,\mathrm{s}^{-1}$.

- The slowest mode among all these motions is the trans-membrane flip-flop of lipids (Fig. 1.4). Due to the enormous energy barrier required to move the the polar headgroup through hydrophobic interior of the membrane, the rate of this flip-flop process is significantly longer than other motions. The fastest reported rate is of the order of minutes but frequently the equilibration time in experiments with initially labeled lipids on one side of the bilayer ranges from hours to weeks [17].

In additions to these general motional modes there are two other motions that can modulate the orientation of H nuclei in C-H bonds which are important from the NMR perspective. They are the vibrational mode of the C-H bond with the time

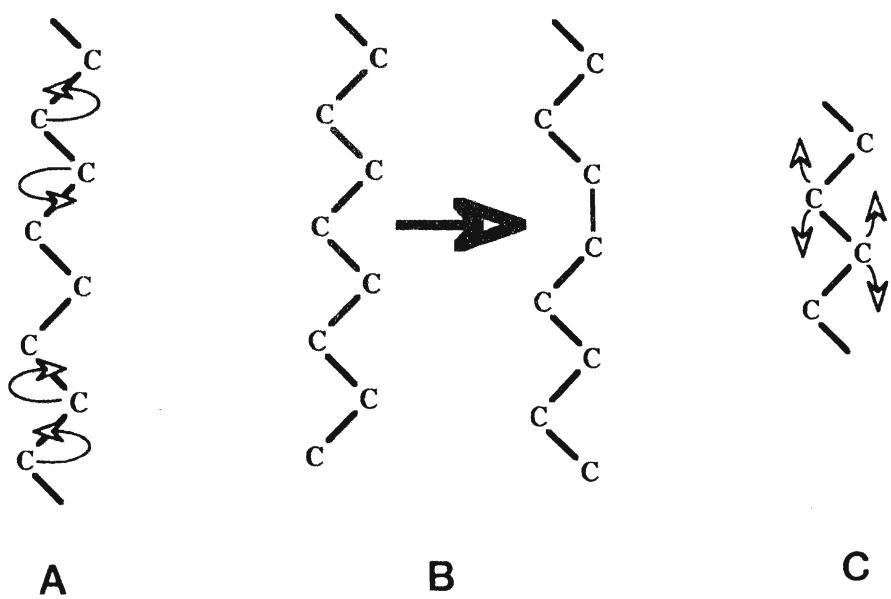

Figure 1.3: **Intramolecular motions of lipids**, (A) Interchain rotation around C-C bonds. (B) Kink formation. (C) Bending of the hydrocarbon chain. Reproduced from [17]

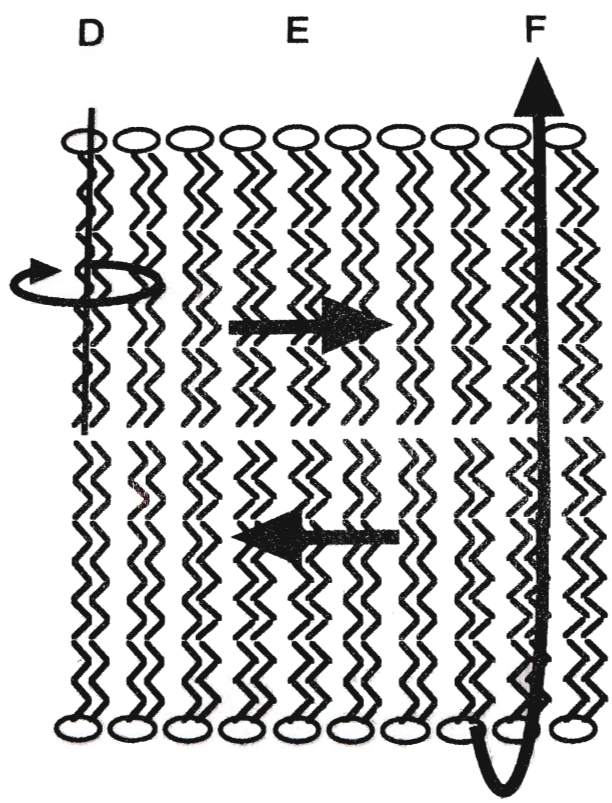

Figure 1.4: **Intermolecular motions of lipids** (D) Rotational diffusion. (E) Lateral diffusion. (F) Trans-membrane flip-flop movement. Reproduced from [17].

scale of 10^{-14}-10^{-15}s [18] and the quantum mechanical exchange of H nuclei on the same methylene groups (or the methyl groups at the end each chain). An important property of lipid membranes in the L_α phase is that the net effect of these motions on the orientation of C-H bonds is an axially symmetric modulation with the long axis of the molecular or approximately, the bilayer normal as the symmetry axis.

Current theoretical models for lipid aggregations are not yet offering a full and comprehensive description of lipid membranes. Most of these models either account for modifications in the membrane properties due to small modulations in pH, temperature *etc.*, or are phenomenological and based on the concept of "shape" of lipid molecules and on similar empirical information. Molecular simulations have been successful in predicting the behavior of membrane proteins or a bilayer region under some simplifications. However, due to the large number of lipids involved in lipid membranes and the large number of parameters required to describe a lipid molecule, the short-time molecular modeling simulations are far from complete. Inevitably, studying complex phenomena associated with model membranes and real biological membranes, which may involve other complex molecules as additives must involve experimental approaches. It is at the convergence of quantitative analysis of spectroscopic data and the growing sophistication of molecular models that the true understanding of biomembranes lies. This necessitates more sophisticated data analysis techniques.

1.2 ^{2}H NMR in studying lipid membranes

Various NMR techniques are routinely used in studying biological and model membranes, each more suited for studying a particular region of lipids in membranes. For instance, ^{31}P NMR is particularly useful in studying the hydrophilic headgroup region of phospholipid membranes. ^{13}C NMR, ^{1}H NMR and ^{2}H NMR are in turn useful in studying the hydrocarbon region of membranes.

Spectra obtained from the lipid membranes are generally dominated by strong proton-carbon dipolar interactions which result in a large number of overlapping resonance peaks and broadenings. Because of these broadenings, the analysis of ^{13}C NMR and ^{1}H NMR spectra is rather difficult. Deuterium magnetic resonance offers some advantages:

- Replacing ^{1}H atoms by ^{2}H atoms through appropriate chemical substitution allows for labeling both the fatty-acid chains and the headgroups. Unlike labeling in other spectroscopies such as electron paramagnetic resonance (ESR) or fluorescence spectroscopy, labeling by deuterium is expected to introduce negligible perturbation in structural and dynamical properties of lipids.

- Observed resonance lines in ^{2}H NMR spectra can be assigned unambiguously to labeled sites.

- Magnetogyric ratio of ^{2}H nucleus is smaller than that of ^{1}H nucleus ($\gamma_D/\gamma_H = 1/6.5$) which results in much weaker dipolar coupling of ^{2}H nuclei compared to the dipolar coupling in proton NMR, and a longer time scale of deuterium NMR. However, as a drawback, smaller magnetogyric ratio results in a weaker coupling of deuterium nuclei to magnetic fields hence, a lower sensitivity of deuterium NMR.

- Since deuterium nuclei in its ground state has an angular quantum number of 1, it possesses a non-zero quadrupole moment. As a result, deuterium NMR can easily detect anisotropic fast motions through the quadrupole coupling of deuterium nuclei to their surrounding electric field gradient. For a rapid isotropic motion only a single line can be observed in the spectrum while for an anisotropic fast motion each deuteron contributes a doublet to the spectrum (Fig. 1.5). The doublet spacing, $\Delta\nu_Q$, which is called *splitting parameter*, depends on the degree of anisotropy and on the orientation of the deuterium nucleus with respect to the static magnetic field[10].

In studying pure lipid membranes two properties of lipids are primarily sought: variation of motional order along the lipid chains known as the "order profile", and the correlation times of various molecular motions. The order profile represents how constrained segments on the hydrocarbon chains are in performing thermal motions, while the correlation times associated with various modes of motions indicate how fast those motions are. The structural and dynamical information about the lipid molecules is contained in the segmental order parameter $S_{CD}(n)$ and the relaxation rates of deuterium NMR spectra.

Different segments on the fatty acid chains experience fluctuations with different amplitudes which, if labeled by ^{2}H, results in differently averaged quadrupole interaction. Averaged quadrupole interactions at different segments result in the presence of doublets with different quadrupole splittings in spectra and, thus, in *anisotropy distributions*(Fig.1.6). Experimentally, these distributions are given by ^{2}H NMR spectra from an oriented bilayer sample, (Fig. 1.7) referred to as *oriented spectra*. In dealing with oriented spectra, the determination of segmental order parameters from quadrupolar splittings is straight forward. S_{CD} is related to the splitting $\Delta\nu_Q$ by following relationship:

$$\Delta\nu_Q = \frac{3}{2}\frac{e^2qQ}{h}S_{CD}\frac{3\cos^2\beta - 1}{2} \tag{1.1}$$

where β is the angle between the symmetry axis of fast modulations of the C-D bond (the bilayer normal in lipid membranes) and the magnetic field of the spectrometer, and $\omega_Q = \frac{e^2qQ}{h}$ is the characteristic quadrupole frequency ($\omega_Q \approx 170$kHz for C-D bonds). Also, relaxation rates can be simply determined by separately fitting the peaks of each doublet to an exponential in a series of partially relaxed spectra [10].

Unlike oriented samples, typical biological and model-membrane samples form spherical or nearly spherical vesicles, often elongated by the external magnetic field

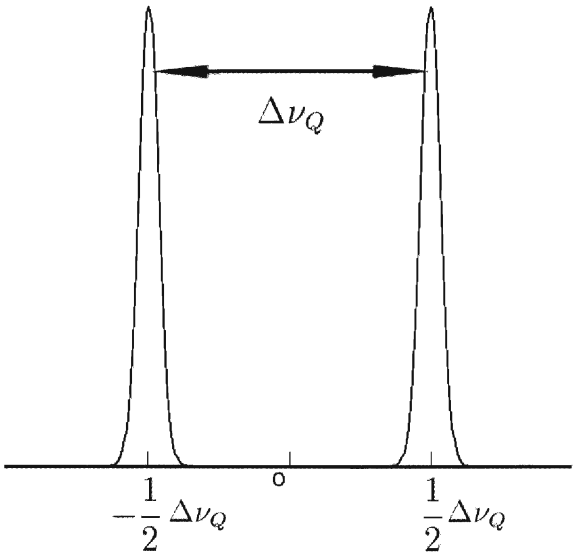

Figure 1.5: **Quadrupolar splitting**: Anisotropic fast motions result in partial averaging of the quadrupole interaction which results in having two resonance peaks separated by $\Delta\nu_Q$. The quadrupolar splitting parameter $\Delta\nu_Q$ is directly related to the averaged part of the quadrupole interaction and the structural order parameter at the location of the deuteron. More extensive fluctuations result in a smaller order parameter and hence, a smaller $\Delta\nu_Q$.

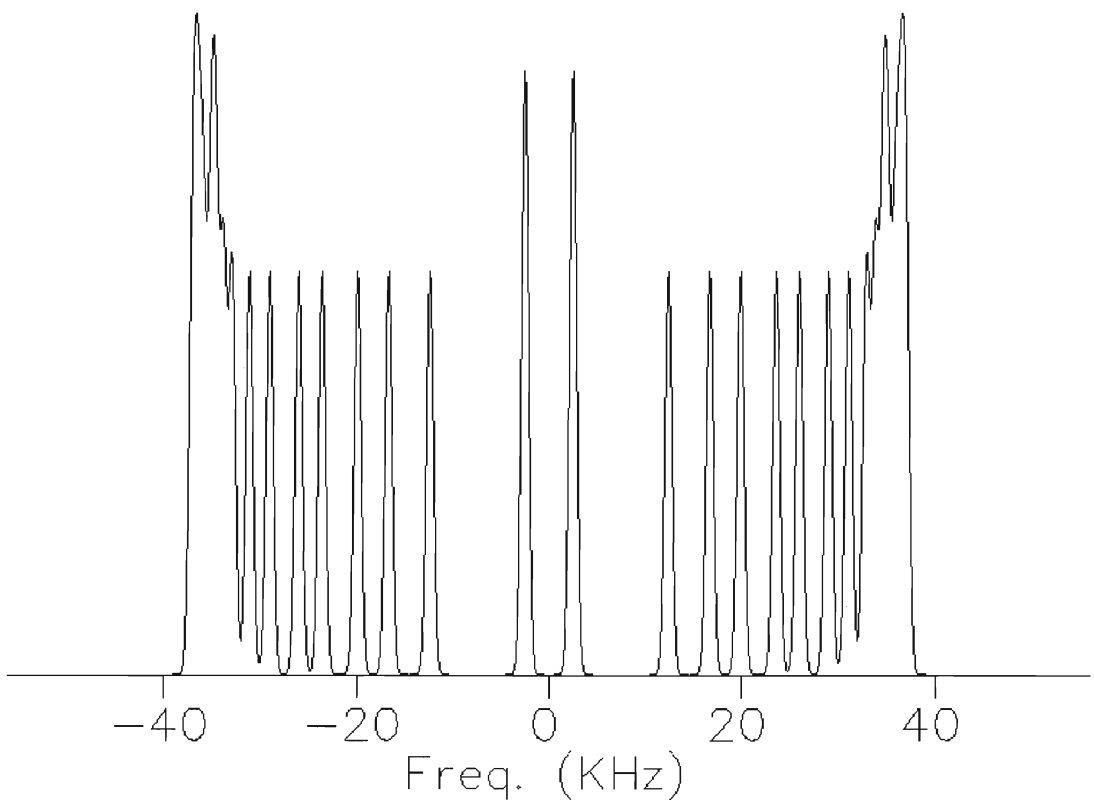

Figure 1.6: **Anisotropy distribution** of fully deuterated POPC lipid with 16 carbon positions on each chain.

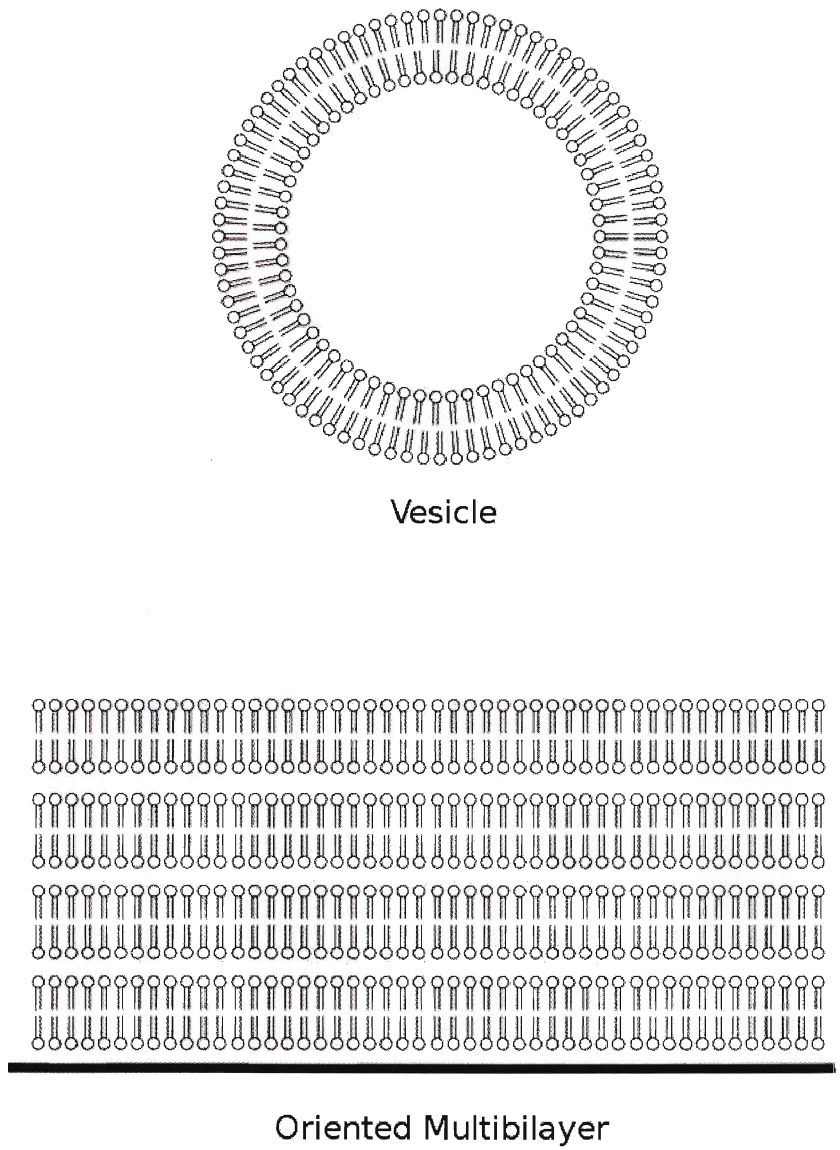

Figure 1.7: **Oriented multibilayer vs a unilamellar vesicle**: An oriented multibilayer is a stack of lipid bilayers on a flat substrate with water layers separating lipid bilayers. The orientations of lipids as determined by their long molecular axes are all the same and perpendicular to the substrate. On the other hand, vesicle domains have different orientations. For instance, the above spherical vesicle is described by a powder distribution, *i.e.* $p(\beta) = \sin(\beta)$.

[9, 19], which gives rise to an orientation distribution of molecular domains (Fig. 1.7). Each labeled position on the lipid chains contributes a doublet to the observed spectrum with a quadrupolar splitting given not only by the order parameter at each position on the chain, but also by the motionally averaged orientation of the C-D bond with respect to the static magnetic field. When there is an orientation distribution of microscopic domains, the superposition of doublets corresponding to these differently oriented domains produces a *powder spectrum* (Fig. 1.8).

Mathematically, a powder spectrum is nothing but a convolution of the two distributions. If $g(\nu)$ and $p(\beta)$ respectively represent the anisotropy and orientation distributions, then the resultant powder spectrum $f(\omega)$ can be written as:

$$f(\omega) = \int g(\nu) \left[p(\beta) \frac{\partial \beta}{\partial \omega} \right] d\nu \tag{1.2}$$

where $\omega = \nu \frac{3\cos^2\beta - 1}{2}$ [20, 21].

Low sensitivity associated with ^{2}H NMR makes preparing oriented bilayers with enough deuterium concentration required for obtaining a clean spectrum a laborious task [10]. Also, oriented bilayers are slightly different from a vesicular membrane in their mechanical properties. Because of the non-zero natural curvature of vesicular membranes, tension in the two leaflets of the lipid bilayer is slightly different. Therefore, obtained information from an oriented sample may not reflect exactly the same properties of a vesicular or a real biological membrane [17]. Consequently, it is more favorable to obtain structural and dynamical properties of lipid membranes directly from powder spectra of vesicular model or real membranes.

Extracting the two anisotropy and orientation distributions from a powder spectrum is known as the *de-Pakeing* problem and requires solving the convolution integral of Eq. 1.2. Integral equations like this convolution equation are usually unstable and mathematically *ill-posed*, that is, they may not posses a unique or a stable solution. Besides, extracting the two anisotropy and orientation distributions from only one powder distribution is a highly under-determined problem. Due to these two restrictions and the unavoidable presence of noise in ^{2}H NMR spectra, any attempt to solve the problem through routine solving procedures are likely to fail. However, regularization algorithms can be used to extract information from ill-posed problems like the de-Pakeing problem. Regularization incorporates prior physically reasonable expectations and external information, such as continuity of the underlying distribution function. For example, it can be assumed that the anisotropy distribution is continuous and that the orientation distribution, on the basis of physical models for elongation of a vesicle in a strong magnetic field, is restricted to a family of ellipsoidal shapes. In this way the problem can be solved and the distributions can be fairly accurately determined, subject to the validity of the underlying assumptions [9, 19, 22, 23]. It must be noted that in a broad range of inverse problems the assumptions required to achieve regularization are quite generic, rigorous, and physically reasonable. Because of that, inverse theory methods found use in a variety

(a)

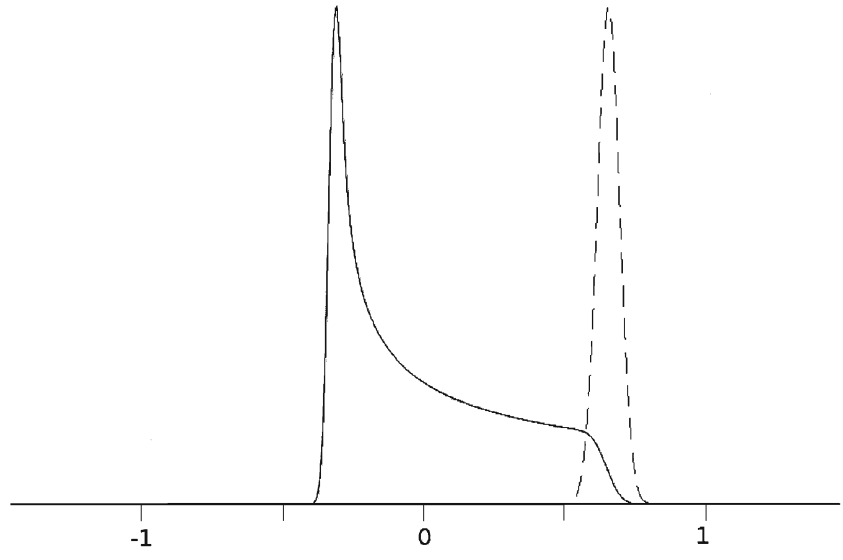

(b)

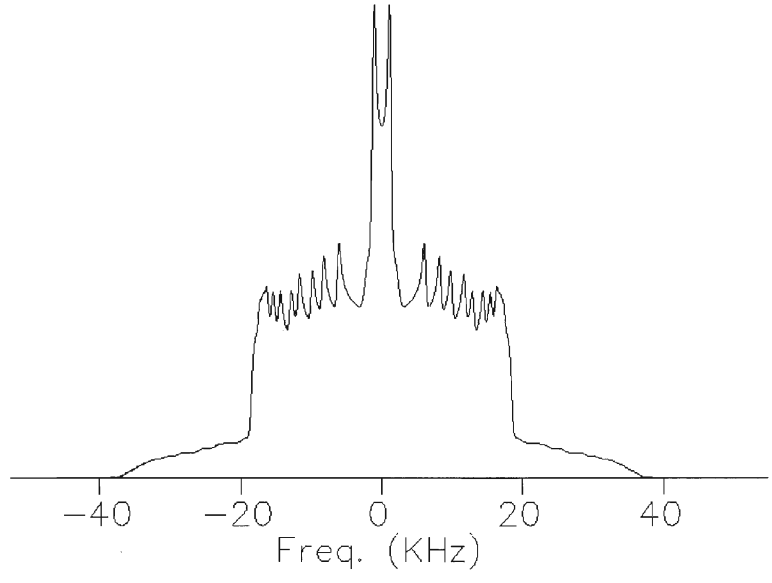

Figure 1.8: **Powder spectrum**: (a) broadening of a single peak due to the powder orientation distribution. (b) powder spectrum of a fully deuterated POPC sample.

of physical fields as discussed in Chapter 3.

Site-specific relaxation rates contain additional information about the order profile of the fatty acid chains and the nature of molecular motions; they are also directly related to the correlation times of fast motions at any labeled site. For example, measuring relaxation rates makes it possible to investigate the correlation time of fast motions through the dependence of relaxation rates on the Larmor frequency ω_0 [4]. In ^{2}H NMR, the dominant relaxation mechanism is the fluctuation of the quadrupole Hamiltonian caused by molecular motions which, unlike relaxation due to the dipole interaction, offers the great advantage of unambiguously relating the observed relaxation rates to molecular motions at each segment along the chain [10].

Analogous to the quadrupolar splitting parameter, various relaxation rates associated with different observables of the deuterium nuclei, such as transverse and longitudinal relaxations, are orientation-dependent (Fig. 1.9). The orientation dependence of relaxation rates can be expressed in terms of three relaxation parameters scaled by known scaling functions [4]. These relaxation parameters can be determined experimentally from an oriented sample by changing its orientation with respect to the direction of the static magnetic field and fitting each decaying doublet in the obtained partially-relaxed oriented spectra separately to an exponential. Repeating this procedure for different orientations allows for finding relaxation parameters corresponding to each doublet [24]. Alternatively, it is possible to determine this information from partially-relaxed powder spectra of samples that have been labeled only at one position on the chain by measuring decay rates of three specific points on the powder pattern spectra corresponding to the shoulder with 0^o, the edge with 90^o, and the centre with 54.74^o which are easy to identify [4, 6].

Observing relaxation in order to extract relaxation parameters from the orientation dependence of relaxation rates not only is limited by the signal-to-noise ratio which can be considered as a technical difficulty, but is also fundamentally limited by lateral diffusion. Lateral diffusion in non-oriented samples randomly changes the orientation of individual lipids and mixes lipids from different domains with different relaxation histories. Thus it tends to obscure the orientation dependence of relaxation rates that eventually, after complete mixing, results in just one relaxation rate at all orientations. Lateral diffusion is usually slow enough compared to the relaxation rates and what is considered as domains in membranes are big enough (containing $\sim 10^4$ lipid molecules) to allow observing a partial relaxation.

The resulting difficulties in interpreting the measured relaxation rates are the likely reason why few experimental observation have been attempted in multiply-site labeled samples, even though the experiments are not particularly difficult to do. Similar to the convolution-integral formulation of the de-Pakeing problem (Eq. 1.2), the longitudinal relaxation of ^{2}H NMR powder spectra can be described by following convolution integral:

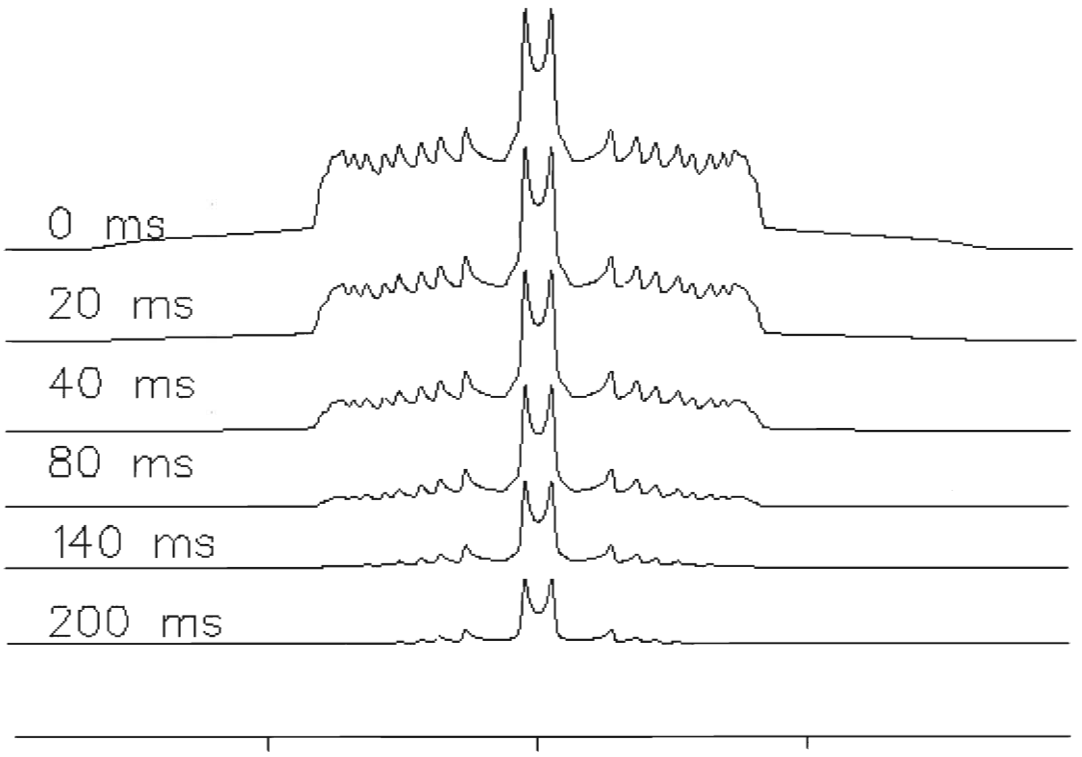

Figure 1.9: **Simulated partially-relaxed spectra** based on longitudinal relaxation rates obtained from oriented single site labeled POPC samples from [24]. As the time goes on not only does the amplitude of the powder spectrum decrease, but its shape also changes such that the shoulders of the spectrum experience a faster relaxation than the center of it. This is typical of most biological and model membrane systems.

$$f(\omega,\tau)=\int\sum_{i}^{n}g_i(\nu)\left[p(\beta)\frac{\partial\beta}{\partial\omega}\right]e^{-\tau/T_1^{(i)}(\beta)}\,d\nu \tag{1.3}$$

where i is the segment position on the chain and $g_i(\nu)$ is the doublet corresponding to the ith segment. In fact, the above relation can be considered as the generalized de-Pakeing problem. The orientation-dependence of the relaxation rate associated with the ith position on the hydrocarbon chain, $\frac{1}{T_1^{(i)}(\beta)}$, is usually in the form of:

$$\frac{1}{T_1^{(i)}(\beta)}=J_{0,0}^{(i)}p_0(\beta)+J_{1,1}^{(i)}(\omega_0)p_1(\beta)+J_{2,2}^{(i)}(2\omega_0)p_2(\beta) \tag{1.4}$$

where $p_k(\beta)$ are known scaling functions and $J_{0,0}^{(i)}$, $J_{1,1}^{(i)}(\omega_0)$ and, $J_{2,2}^{(i)}(2\omega_0)$ are the relaxation parameters ought to be found. Further justification for this form of the relaxation-rate parameterization will become clear in Chapter 2.

The aim of this thesis is to propose a numerical pseudo-inversion procedure based on advanced regularization tools. Solving ill-posed inverse problems to extract relaxation parameters as well as a more accurate estimations for the anisotropy and orientation distributions from a series of partially-relaxed powder spectra is the ultimate goal.

Chapter 2

Theory of ^{2}H NMR

Generally, what can be directly observed in any NMR experiment is the in-phase precession of nuclear spins manifested in the precession of the sample's net nuclear magnetization around the magnetic field of the spectrometer. The observation duration of this precessing nuclear magnetization is severely limited by its fast decay due to local magnetic field inhomogeneities that result in slightly different precession frequencies of the nuclear spins. The term *free induction decay* (FID) is used to refer to this decaying nuclear magnetization. The Fourier transform of the FID signal is what is referred to as the spectrum and consists of one or several resonance peaks corresponding to photons radiated by the nuclear spins. The location of these resonance peaks depend on the interactions of the nuclei, while the amplitudes are related to the pre-observation history of the nuclear ensemble. Changes in the amplitudes of resonance peaks that result from different pre-observation evolutions can be attributed to various relaxations, exchange processes, and so forth.

When the sample is placed in the spectrometer and exposed to its strong magnetic field, the Zeeman interaction between this strong magnetic field and the nuclear spins lifts the degeneracy in the energy levels of the nuclear ensemble. Consequently, the population of nuclei in different quantum states is given by the Boltzmann factors (Fig. 2.1). The partial alignment of nuclear spins along the magnetic field of the spectrometer produces a net longitudinal magnetization, but since this magnetization is typically four orders of magnitude smaller than the diamagnetic field of electronic spins, its direct detection is impractical [26].

Irradiating the sample with a sequence of radio-frequency pulses with precise frequency, amplitude, and durations makes it possible to manipulate its net nuclear magnetization. An RF pulse in NMR is basically an oscillating magnetic field at the Larmor frequency of the intended nuclear species in the direction perpendicular to the external magnetic field. Applying a sequence of RF pulses with the precise timing and durations allows to rotate nuclear spins arbitrarily[1]. A simple though important instance of such RF pulses is the so-called 90^o_x pulse that starts most of NMR experiments by rotating the nuclear spins by 90^o about the x-axis of the rotating frame. This rotation brings the net nuclear magnetization into the xy-plane and makes it observable through its precession around the magnetic field of the spectrometer.

[1]The magnetic field of an RF pulse with exactly the same frequency of the Larmor precession frequency of the intended nuclei species is effectively static in the rotating frame of nuclear spins. Nuclear spins precess around this magnetic field of the RF pulse in the rotating frame which allows for manipulating their orientation by controlling the duration of the RF pulse.

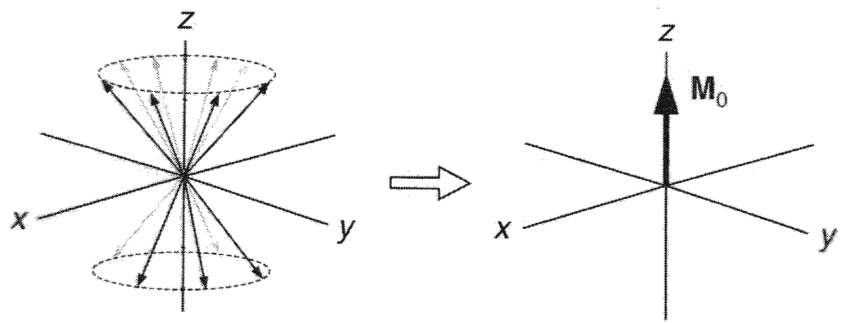

Figure 2.1: **Partial alignment of nuclear spins along the strong magnetic field of the spectrometer** represent the classical view of the Boltzmann distribution of the populations in various quantum-mechanical states. Reproduced from [25]

Since the magnetogyric ratio of different nuclear species are different and because of the very high Larmor frequency (hundreds of MHz) in a typical several-Tesla magnetic field, applied RF pulses rotate the nuclear magnetization of only the intended nuclei.

The above description summerizes the so-called classical picture of NMR. However, nuclear magnetic resonance is intrinsically a quantum mechanical phenomena. Classical models that treat nuclear spins as classical magnetic dipoles are useful in modeling general aspects of nuclear resonance, but fail to account for phenomena such as orientation-dependence of relaxation rates or shifts in the location of resonance peaks due to fast-motion averaging of tensorial interactions. Knowing these relations is vital in analyzing NMR spectra, and thus necessitates a rigorous and precise quantum-mechanical formulation of the evolution of the nuclear ensemble.

2.1 ^{2}H NMR Hamiltonian

After the Zeeman interaction, the dominant interaction between a deuterium nucleus and its surroundings is the quadrupole interaction. The total Hamiltonian of the deuterium nucleus can be written as [10]:

$$\hat{H} = \hat{H}_Z + \hat{H}_Q \tag{2.1}$$

where $\hat{H}_Z = -\gamma_D \hat{\vec{I}} \cdot \vec{B}_0$ and $\hat{H}_Q$ are respectively the Zeeman and the quadrupole Hamiltonians. In the Zeeman Hamiltonian γ_D is the magnetogyric ratio of the deuterium nucleus, $\vec{B}_0$ is the static magnetic field of the spectrometer which is usually along the $\hat{z}$ axis of the lab coordinate system, and $\hat{\vec{I}}$ is the total angular momentum operator of the deuterium nucleus. The Larmor frequency, $\omega_0 = -\gamma B_0$, for a deuterium nucleus in a $7T$ magnetic field is about $2\pi \times 46$MHz.

2.1.1 Quadrupole Hamiltonian

A nucleus is a distribution of charge and can experience an electrostatic interaction with its surrounding electron cloud. The quadrupole interaction is the third term in the expansion of this electrostatic interaction of the nucleus. The first term is the point charge approximation and has no effect on the orientation of the nucleus. The second term is the electric dipole approximation that vanishes based on the parity symmetry of all known nuclei. The third term is the quadrupole approximation for the charge distribution of the nucleus. The Wigner-Eckart theorem provides the link to relate the distribution of nucleons to the total angular momentum state of the nucleus [27]. Moreover, it states only nuclei with quantum numbers greater or equal to 1 can possess quadrupole moments. Note that in the case of ^{2}H nuclei there is no 4^{th} or higher terms in the expansion of the electrostatic interaction of the nucleus with its surrounding electron cloud [26].

The quadrupole Hamiltonian in its most general form can be written as [28]:

$$\hat{H}_Q = \frac{eQ}{2I(2I-1)\hbar} \hat{\vec{I}} \cdot \mathbf{V} \cdot \hat{\vec{I}} \tag{2.2}$$

where I and Q are the quantum number and the quadrupole moment of the nucleus, $\mathbf{V}$ is the electric field gradient tensor (EFG) related to the electric field at the location of the nucleus by:

$$V_{ij} = \frac{\partial E_i}{\partial r_j} \tag{2.3}$$

By definition, $\mathbf{V}$ is a symmetric tensor and hence diagonalizable. The principal axis coordinate system (PACS) of the EFG tensor is the particular coordinated system in which $\mathbf{V}$ becomes diagonal. Indicating axes of the PACS by XYZ, the EFG tensor in the PACS will have the form:

$$\mathbf{V} = \begin{pmatrix} V_{XX} & 0 & 0 \\ 0 & V_{YY} & 0 \\ 0 & 0 & V_{ZZ} \end{pmatrix} \tag{2.4}$$

The diagonal entries of the EFG tensor must satisfy the Laplace's equation, *i.e.*, $V_{XX} + V_{YY} + V_{ZZ} = 0$. Therefore, in the PACS, $\mathbf{V}$ is totally determined by only two parameters. These two parameters can be chosen as:

$$q = \frac{V_{ZZ}}{e} \tag{2.5}$$

$$\eta_{EFG} = \frac{V_{XX} - V_{YY}}{V_{ZZ}} \tag{2.6}$$

where q and η_{EFG} are known as the strength and the asymmetry of the EFG tensor. In the PACS the quadrupole Hamiltonian can be written as:

$$\hat{H}_Q = \frac{eQ}{2I(2I-1)\hbar}\frac{1}{2}\left(V_{ZZ}(3\hat{I}_Z^2 - I^2) + (V_{XX} - V_{YY})(\hat{I}_-^2 + \hat{I}_+^2)\right) \tag{2.7}$$

For a deuterium nucleus in a C-D bond, since the surrounding electron clouds of the bond is axially symmetric, η_{EFG} vanishes, and the quadrupole Hamiltonian becomes:

$$\hat{H}_Q = \frac{1}{4}\omega_Q\left(3\hat{I}_Z^2 - I^2\right) \tag{2.8}$$

$\omega_Q = \frac{e^2qQ}{\hbar}$ is the characteristic frequency of the quadrupole interaction, and about $2\pi \times 170$kHz for deuterium nuclei in C-D bonds [10].

The above expression for the quadrupole Hamiltonian is only valid in the PACS of the C-D bond. To transform it to an arbitrary coordinate system, the angular momentum operator $\hat{I}_Z$ in the above expression should be rewritten in the new coordinate system operators $\hat{I}_x$, $\hat{I}_y$, and $\hat{I}_z$. Because of the axial symmetry of the EFG tensor, only two angles θ, ϕ (instead of the three Euler angles) suffice to specify the transformation of the quadrupole Hamiltonian from the PACS to the new coordinate system $x\,y\,z$. It turns out that the transformed quadrupole Hamiltonian can be written in a compact and elegant form by means of 2^{nd}-rank irreducible tensor operators and 2^{nd}-rank spherical harmonics as following [6],[27]:

$$\hat{H}_Q = \omega_Q \sum_{m=-2}^{2} \hat{T}_m^{(2)} Y_{2,-m}(\theta, \phi) \tag{2.9}$$

where $\hat{T}_m^{(2)}$ are 2^{nd}-rank irreducible tensor operators given in Table 2.1 [27].

The appearance of 2^{nd} rank irreducible tensor operators in Eq. 2.9 is not surprising as the derivation of the quadrupole Hamiltonian by the Wigner-Eckart theorem is based on the irreducible tensor operators. The characteristic frequency of the quadrupole interaction, ω_Q, represents the strength of the quadrupole coupling between the nuclei and the gradient of their surrounding electric field; its reciprocal, as was mentioned before, defines the so-called "NMR time scale".

The presence of molecular motions provides continuous orientational modulation of the C-D bond and thus the time-dependence of the PACS orientation which gives rise to the time-dependence of the quadrupole Hamiltonian. The instantaneous orientation of the PACS with respect to the lab frame can be represented by $\theta(t), \phi(t)$ where $\theta(t)$ is the angle between the C-D bond and the $\hat{z}$ axis of the lab frame. Fast

$T_2^{(2)}$	$\hat{I}_+^2$
$T_1^{(2)}$	$-(\hat{I}_z\hat{I}_+ + \hat{I}_+\hat{I}_z)$
$T_0^{(2)}$	$\sqrt{\frac{2}{3}}(3\hat{I}_z^2 - \hat{I}^2)$
$T_{-1}^{(2)}$	$(\hat{I}_z\hat{I}_- + \hat{I}_-\hat{I}_z)$
$T_{-2}^{(2)}$	$\hat{I}_-^2$

Table 2.1: **2^{nd}-rank irreducible tensor operators**

molecular motions with time scales much shorter than ω_Q^{-1} result in averaging this time-dependent quadrupole Hamiltonian. The averaging can be conceived either as averaging EFG tensor to get an averaged EFG tensor with an averaged PACS, or as averaging the quantum operator part of the quadrupole Hamiltonian (Eq. 2.2). From the definition of vector operators in quantum mechanics, it can be readily seen that these two averaging procedures are the same and translatable to each other[2].

To distinguish the static orientation of the averaged quadrupole interaction from its fluctuating part, transformation from the instantaneous orientation of the PACS into the lab frame can be performed in two steps. First, the orientation of the instantaneous PACS with respect to the averaged PACS determined by $\theta'(t)$,$\phi'(t)$ and then the orientation of the averaged PACS with respect to the lab frame indicated by β, α (Fig. 2.2). To accommodate this two-step transformation, Eq. 2.9 should be recast explicitly in terms of $\theta'(t)$, $\phi'(t)$, β, and α. Second-rank spherical harmonics transform from one coordinate system to another according to the following transformation rule:

$$Y_{2,m}(\theta,\phi) = \sum_{n=-2}^{2} D_{n,m}^{(2)}(\alpha,\beta,\varphi) Y_{2,n}(\theta',\phi') \tag{2.10}$$

where $D_{n,m}^{(2)}(\alpha,\beta,\varphi)$ is the mn entry of the Wigner D-matrix and α,β,φ are the Euler angles of the transformation from the coordinate system of $Y_{2,n}(\theta',\phi')$ to the coordinate system of $Y_{2,m}(\theta,\phi)$. The Wigner D-matrix is related to the reduced Wigner D-matrix (or d-matrix, see Table 2.2) by:

$$D_{m',m}^{(2)}(\alpha,\beta,\varphi) = e^{im'\alpha} d_{m',m}^{(2)}(\beta) e^{im\varphi} \tag{2.11}$$

[2]Vector operators transform from one coordinate system to another just like ordinary vectors. More specifically, spherical harmonics transform exactly in the same way that 2^{nd}-order irreducible tensors do, *i.e.,* by the Wigner D-Matrix.

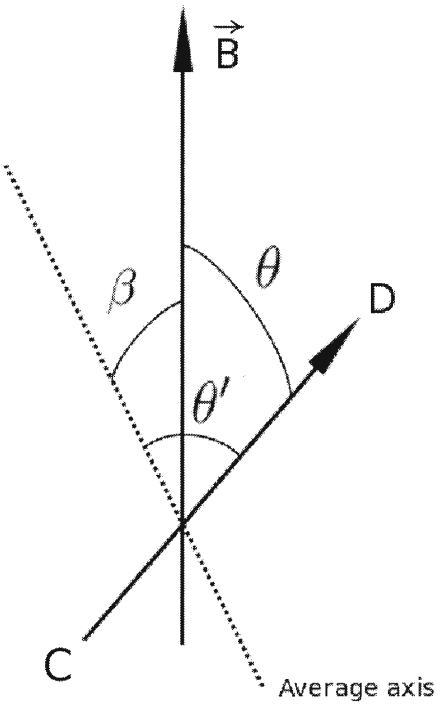

Figure 2.2: **Orientation of the C-D bond**

where for a "z-y-z" Euler transformation $d^{(2)}_{m',m}$ will be all real [29].

m'	2	1	0	−1	−2
2	$\frac{(1+\cos\beta)^2}{4}$	$\frac{1+\cos\beta}{2}\sin\beta$	$\sqrt{\frac{3}{8}}\sin^2\beta$	$\frac{1-\cos\beta}{2}\sin\beta$	$\frac{(1-\cos\beta)^2}{4}$
1	$-\frac{1+\cos\beta}{2}\sin\beta$	$\cos^2\beta-\frac{1-\cos\beta}{2}$	$\sqrt{\frac{3}{8}}\sin 2\beta$	$-\cos^2\beta+\frac{1+\cos\beta}{2}$	$\frac{1-\cos\beta}{2}\sin\beta$
0	$\sqrt{\frac{3}{8}}\sin^2\beta$	$-\sqrt{\frac{3}{8}}\sin 2\beta$	$\frac{3\cos^2\beta-1}{2}$	$\sqrt{\frac{3}{8}}\sin 2\beta$	$\sqrt{\frac{3}{8}}\sin^2\beta$
−1	$-\frac{1-\cos\beta}{2}\sin\beta$	$-\cos^2\beta+\frac{1+\cos\beta}{2}$	$-\sqrt{\frac{3}{8}}\sin 2\beta$	$\cos^2\beta-\frac{1-\cos\beta}{2}$	$\frac{1+\cos\beta}{2}\sin\beta$
−2	$\frac{(1-\cos\beta)^2}{4}$	$-\frac{1-\cos\beta}{2}\sin\beta$	$\sqrt{\frac{3}{8}}\sin^2\beta$	$-\frac{1+\cos\beta}{2}\sin\beta$	$\frac{(1+\cos\beta)^2}{4}$

Table 2.2: **Wigner small d-matrix entries** [29]

The quadrupole Hamiltonian in this two-step representation of the orientation will be:

$$\hat{H}_Q(t)=\omega_Q\sum_{m=-2}^{2}\hat{T}^{(2)}_m\left[\sum_{n=-2}^{2}D^{(2)}_{n,-m}(\alpha,\beta,\varphi)Y_{2,n}(\theta'(t),\phi'(t))\right] \tag{2.12}$$

As a direct consequence of axial symmetry of the EFG tensor of C-D bonds there will be a class of equivalent PACSs rather than a unique PACS. Consequently, only two angles β,α suffice to determine the orientation of the averaged PACS with respect to the lab frame, and the third angle φ in Eq. 2.12 has no effect on the transformation and can be ignored. It should be stressed that in spite of axial symmetry of the EFG tensor of the C-D bond, the averaged EFG tensor over a non-axially symmetric fluctuation may not be axially symmetric in general [10].

The molecular motions in lipid membranes are such that the averaged orientation of C-D bonds do possess axial symmetry with the bilayer normal as the axis of symmetry. Because of this axial symmetry, among the five spherical harmonics in Eq. 2.9 only $Y_{0,0}$ survives the averaging. Representing the averaged quadrupole Hamiltonian by $\hat{\bar{H}}_Q$, Eq. 2.12 becomes:

$$\hat{\bar{H}}_Q=\omega_Q S_{CD}\sum_{m=-2}^{2}\hat{T}^{(2)}_m D^{(2)}_{0,-m}(\alpha,\beta,0) \tag{2.13}$$

where the previously introduced order parameter S_{CD} is given by:

$$S_{CD}=\langle\frac{3\cos^2\theta'(t)}{2}\rangle_t \tag{2.14}$$

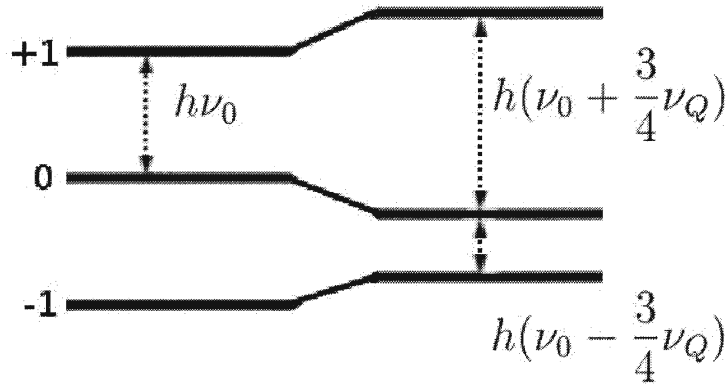

Figure 2.3: **Energy levels of a ^{2}H nucleus** ν_0 is the Larmor frequency and ν_Q is the quadrupolar splitting parameter in units of Hz. This energy diagram is highly exaggerated for the sake of representation, in ^{2}H NMR $\nu_0 \gg \nu_Q$.

Since only $Y_{0,0}(\theta'(t), \phi'(t))$ survives the averaging with $n = 0$, Eq. 2.13 is independent of α and the whole orientation dependence is determined only by β. Here $\langle \ldots \rangle_t$ represents averaging over time which, since this averaging originates from the energy-time uncertainty principle, is subject to $t \ll \omega_Q^{-1}$ constraint (averaging over times shorter than the NMR time scale) [10].

2.1.2 Energy Levels

Because the Zeeman interaction of a deuterium nucleus with the high magnetic field of the spectrometer is much stronger than the quadrupole interaction ($\omega_0 \gg \omega_Q$), the Zeeman energy levels of a ^{2}H nucleus will be the weakly perturbed by the quadrupole interaction (Fig. 2.3). The modification in the Zeeman energy levels due to the presence of the quadrupole interaction can be obtained from the first-order perturbation theory. The first-order perturbation only takes into account the diagonal elements of the quadrupole Hamiltonian in the eigenbasis representation of the Zeeman Hamiltonian. The resultant projected quadrupole Hamiltonian is usually referred to as

the *secular part* of the quadrupole Hamiltonian [26]. The total Hamiltonian in this high-field approximation can be written as:

$$\hat{H}_0 = -\gamma_D B_z \hat{I}_z + \frac{1}{4}\omega_Q S_{CD} \frac{3\cos^2\beta - 1}{2}(3\hat{I}_z^2 - \hat{I}^2) \tag{2.15}$$

where B_z is the magnetic field seen at the nucleus that may be different from B_0 due to the presence of chemical shifts[3], and β is the angle between the symmetry axis of the averaged PACS axis and the magnetic field of the spectrometer.

As seen in Fig. 2.3, the perturbation in the Zeeman energy levels due to the quadrupole Hamiltonian, despite being very weak, has a significant effect on the spectrum. In the absence of the quadrupole interactions the spectrum will only contain a single resonance line at ω_0 corresponding to two photons with the same frequency. The introduction of the quadrupole interaction (for $I = 1$ nuclei) results in having two photons with slightly different frequencies, and hence two resonance lines separated by $\frac{3}{4\pi}\omega_Q S_{CD}$ [10]. For deuterium nuclei in lipid membranes $S_{CD} \approx 0.2$ or less [4].

2.2 Relaxation

Relaxation is the macroscopic manifestation of the incoherent evolution of the nuclear ensemble. Relaxation is inherently irreversible, and should not be confused with the reversible loss of coherence due to chemical shifts, which causes different nuclei to experience different local magnetic fields and precess at different Larmor frequencies. More severe local magnetic field inhomogeneities translates into a faster loss of coherence in the nucleus ensemble which causes a rapid de-phasing of the observed signal during the FID period. However, if the chemical shift tensor remains constant over the course of the experiment, it is possible to reverse the evolution of the nuclear ensemble by applying appropriate RF pulse sequences to refocus nuclear spins and recover the coherence. This reestablishment of coherence and recovering the seemingly lost order is known as the *echo phenomenon*[4].

Overcoming the fast decay of the FID signal due to reversible de-phasing allows for observing slower irreversible relaxations with stochastic origins. Irreversible relax-

[3]The strong magnetic field of the spectrometer, $\vec{B}_0$, affects the electron spins. The way the local diamagnetic fields are affected by these electrons is described by the chemical-shift tensor σ_{cs} [28]:

$$\vec{B}_z = \sigma_{cs}\vec{B}_0$$

[4]NMR echo is analogous to mixing a drop of ink in a highly viscous fluid. Stirring the fluid seemingly obliterates the initial order, but by reversing the stirring direction the drop can be restored. Since the diffusion rate in viscous fluids is slow this mixing process is reversible over the stirring time scale. Similarly, since the lateral diffusion in lipid membranes is much slower than the FID time scale, it is possible to reverse the decay of the FID signal.

ation due to a fluctuating interaction such as the quadrupole or dipole interaction is separated empirically into two categories, *spin-lattice* and *spin-spin* relaxations [25]. The spin-lattice relaxation which is also known as the longitudinal relaxation is the evolution of the nuclear ensemble toward thermal equilibrium with the lattice and regaining its initial alignment along the magnetic field. The relaxation rate associated with this longitudinal relaxation is denoted by T_1. Despite the misleading terminology, the spin-spin relaxation or transverse relaxation, which is the phenomena of irreversible loss of coherence during the precession of nuclear spins in the xy-plane, is not necessarily caused by dipolar interactions between two nuclei. The fundamental distinction that defines the spin-spin relaxation, also referred to as the transverse relaxation, is that it doesn't involve energy exchange with the lattice.

Felix Bloch in his phenomenological formulation of relaxation in terms of exponentially decaying functions, distinguished the two relaxations by attributing them with two distinct time constants, T_1 for the longitudinal relaxation and T_2 for the transverse relaxation. Indicating nuclear magnetism with $\vec{M}$ and the equilibrium magnetization with M_0, Bloch's equation can be written as [30]:

$$\frac{d\vec{M}}{dt} = -\gamma_D \vec{M} \times \vec{B}_0 - \frac{M_x \hat{i} + M_y \hat{j}}{T_2} - \frac{M_z - M_0}{T_1}\hat{k} \tag{2.16}$$

The inclination of nuclei toward reestablishment of thermal equilibrium state is the origin of longitudinal relaxation. Immediately after any RF pulse that moves nuclear spins away from their thermal equilibrium state, the nuclear ensemble evolves to resume its equilibrium state. Unlike transverse relaxation, longitudinal relaxation involves exchange of energy with the lattice[5] and dissipation of absorbed energy from the RF pulse.

2.2.1 Observing Longitudinal and Transverse Relaxations

The relaxation times of the longitudinal and transverse relaxations are typically much longer than the duration of the FID decay, and the effective duration of the the experiment should be somehow extended beyond the FID period. Also, in the case of longitudinal relaxation where direct observation of nuclear magnetization along the $\hat{z}$ axis is not possible, indirect detection experiments should be devised. These requirements can be met by applying the *solid (quadrupole) echo* pulse sequence in observing transverse relaxation and the *inversion recovery sequence* in the case of longitudinal relaxation [25].

The basic idea of the solid-echo pulse sequence is very similar to that of the spin-echo sequence. In spin-echo experiments after the starting 90^o_x pulse, another 180^o_x pulse is applied after some time (τ) which reverses the precession of nuclear spins in the x-y plane and results in refocusing and recovering the full signal after waiting the

[5] In spin-lattice relaxation theory, lattice is anything that can interact with the nuclei and serves as a thermal reservoir for the nuclear ensemble.

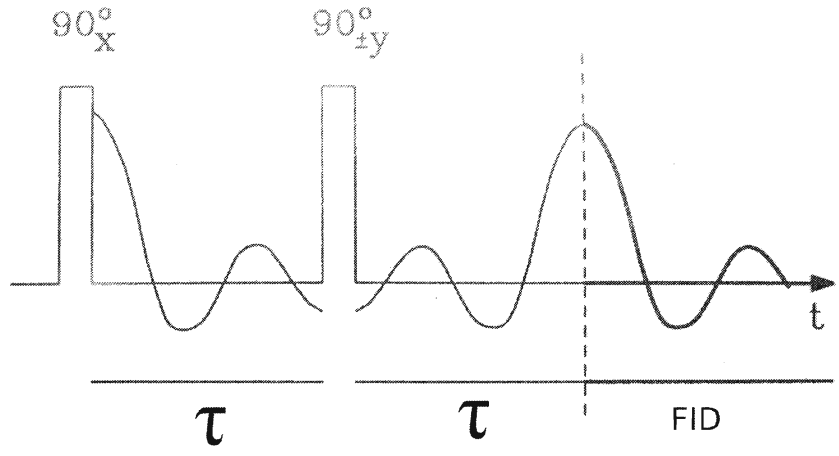

Figure 2.4: **Quadrupole echo pulse sequence**

exact same time that it took for nuclear spins to de-phase, *i.e.*, τ.

Spin-echo pulse sequence cannot be applied to nuclei that possess quadrupole interactions. The problem with applying this $90^o_x - \tau - 180^o_x - \tau$ spin echo sequence to nuclei with $I > \frac{1}{2}$ is that it fails to reverse the evolution due to the secular part of the averaged quadrupole Hamiltonian. However, the spin echo sequence can be modified by replacing the second 180_x pulse with an $90^o_{\pm y}$ pulse which results in the solid-echo pulse sequence [28] (Fig. 2.4).

Unlike the spin-echo and solid-echo pulse sequences, the inversion recovery sequence starts with a 180^o_x pulse which inverts the direction of the nuclear magnetization of the sample. As expected, right after this pulse the nuclear ensemble evolves to resume its thermal equilibrium state that results in the decay of the reversed magnetization which is now in the $-\hat{z}$ direction. To track this decay, after a time τ another 90^o_x is applied to bring the magnetization to the xy-plane and observing the FID signal [4, 25]. Obviously, a longer delay between the two pulses results in a weaker obtained FID signal which allows the tracking of the longitudinal magnetization decay (Fig. 2.5).

2.2.2 Spin-lattice Relaxation Theory

In the framework of the spin-lattice relaxation theory, relaxation is assumed to be the result of evolution under a fluctuating Hamiltonian with a vanishing time average. In

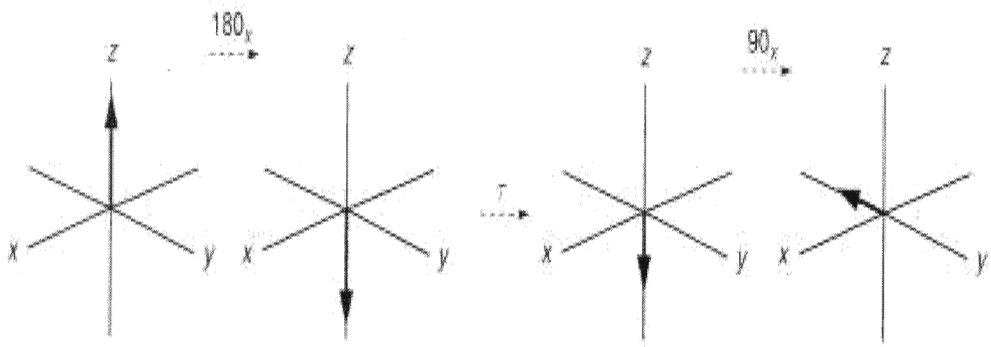

Figure 2.5: **The inversion recovery process** (reproduced from [25]).

the case of deuterium nuclei this relaxation Hamiltonian is the averaged part of the quadrupole Hamiltonian:

$$\hat{H}_R(t) = \hat{H}_Q(t) - \langle \hat{H}_Q(t) \rangle \tag{2.17}$$

More explicitly this relaxation Hamiltonian can be written as:

$$\hat{H}_R(t) = \omega_Q \sum_{m=-2}^{2} \hat{T}_m^{(2)} \left[Y_{2,-m}(\theta(t), \phi(t)) - \langle Y_{2,-m}(\theta(t), \phi(t)) \rangle_t \right] \tag{2.18}$$

Since only ensemble-averaged observables matter rather than observables of a single nucleus, the best way of formulating the relaxation is in terms of density matrix. The evolution of the density matrix $\rho(t)$ under the complete, un-averaged Hamiltonian is given by:

$$\frac{d\rho(t)}{dt} = -i \left[\hat{H}, \rho(t) \right] \tag{2.19}$$

or equivalently:

$$\frac{d\rho(t)}{dt} = -i \left[\hat{H}, \rho(0) \right] - \int_0^t \left[\hat{H}, \left[\hat{H}, \rho(t') \right] \right] dt' \tag{2.20}$$

which, as it will be seen shortly, is more suitable in obtaining the master equation of relaxation. Transforming this density matrix evolution equation to the interaction representation singles out the effect of the relaxation Hamiltonian:

$$\frac{d\tilde{\rho}(t)}{dt} = -i \left[\hat{\tilde{H}}(t), \tilde{\rho}(0) \right] - \int_0^t \left[\hat{\tilde{H}}(t), \left[\hat{\tilde{H}}(t'), \tilde{\rho}(t') \right] \right] dt' \tag{2.21}$$

where $\tilde{\rho}(0)$ and $\hat{\tilde{H}}(t)$ are the density matrix and the total Hamiltonian in the interaction representation. The transformation to the interaction representation is usually constructed from the averaged, time-independent part of the total Hamiltonian, $\hat{H}_0 = \hat{H}_z + \langle \hat{H}_Q(t) \rangle$, which results in:

$$\hat{\tilde{H}}(t) = \hat{\tilde{H}}_R(t)$$

However, transforming to intermediate representations with just part of the time-independent Hamiltonian is also possible [31]. Since in ^{2}H NMR the Zeeman interaction is much stronger than the averaged quadrupole Hamiltonian ($\hat{H}_z \gg \langle \hat{H}_Q(t) \rangle$), the averaged quadrupole Hamiltonian in $\hat{H}_0$ can be ignored.

This semi-classical formulation of relaxation treats the lattice as a classical system that can exchange energy with the nuclei unrestrictedly. However, the precise approach to relaxation requires taking into account the fact that the lattice itself is a quantum mechanical system that has its own finite temperature density matrix and population distribution. To accommodate the finite temperature of the lattice in this

semi-classical picture, the thermal equilibrium density matrix of the nuclear ensemble should be phenomenologically inserted into the relaxation equation by replacing $\tilde{\rho}(t)$ with $\tilde{\rho}(t) - \tilde{\rho}_{eq}$ [31] where:

$$\rho_{eq} = \frac{e^{-\hat{H}_0/k_BT}}{Tr[e^{-\hat{H}_0/k_BT}]}$$

Then the modified equation becomes:

$$\frac{d\tilde{\rho}(t)}{dt} = -i\left[\hat{\tilde{H}}_R(t), (\tilde{\rho}(0) - \tilde{\rho}_{eq})\right] - \int_0^t \left[\hat{\tilde{H}}_R(t), \left[\hat{\tilde{H}}_R(t'), (\tilde{\rho}(t') - \tilde{\rho}_{eq})\right]\right] dt' \quad (2.22)$$

Since it is assumed that there are no correlations between remote parts of the nuclear ensemble, separate parts of the ensemble relax independently of each other. Hence, each of them experiences a different evolution history that leads to a different density matrix $\tilde{\rho}$. Therefore, to obtain an equation that describes the evolution of the ensemble observables, Eq. 2.22 should be averaged over the whole ensemble:

$$\frac{d\bar{\tilde{\rho}}(t)}{dt} = -i\overline{\left[\hat{\tilde{H}}_R(t), (\tilde{\rho}(0) - \tilde{\rho}_{eq})\right]} - \int_0^t \overline{\left[\hat{\tilde{H}}_R(t), \left[\hat{\tilde{H}}_R(t'), (\tilde{\rho}(t') - \tilde{\rho}_{eq})\right]\right]} dt' \quad (2.23)$$

Based on the ergodic theorem, the ensemble average of the oscillating relaxation Hamiltonian is equivalent to its time average which by definition is zero. In addition, since the initial and equilibrium density matrices are the same for all nuclei in the system, the first term on the right hand side of Eq. 2.22 vanishes. However, the second term, which contains the product of the relaxation Hamiltonian with itself does not vanish after averaging. Inserting the quadrupolar relaxation Hamiltonian (Eq. 2.18) into Eq.2.23 gives:

$$\frac{d\bar{\tilde{\rho}}(t)}{dt} = -\omega_Q^2 \sum_{m,m'} \int_0^t \overline{\left[\hat{\tilde{T}}_m^{(2)}(t), \left[\hat{\tilde{T}}_{m'}^{(2)\dagger}(t'), (\tilde{\rho}(t') - \tilde{\rho}_{eq})\right]\right] F_m(t) F_{m'}^*(t')}\, dt' \quad (2.24)$$

where $F_m(t) = Y_{2,-m}(\theta(t), \phi(t)) - \langle Y_{2,-m}(\theta(t), \phi(t))\rangle_t$ are random functions with a vanishing average but a non-vanishing *auto-correlation*:

$$G_{m,m'}(\tau) = \overline{F_m(t) F_{m'}^*(t+\tau)} \quad (2.25)$$

Also, from the definition of 2^{nd}-rank irreducible tensors, $\left[\hat{T}_m^{(2)}, \hat{I}_z\right] = m\hat{T}_m^{(2)}$, and, as mentioned, the fact that $\hat{H}_0$ is dominated by the Zeeman Hamiltonian, the 2^{nd}-rank irreducible tensor operators in the interaction representation will be:

$$\hat{\tilde{T}}_m^{(2)}(t) = e^{im\omega_0 t}\hat{T}_m^{(2)} \quad (2.26)$$

where ω_0 is the Larmor frequency.

Since Eq. 2.24 contains the sought density matrix $\bar{\tilde{\rho}}(t)$ in the argument of the integral on the right hand side, its solution will have dependence on the past history of $\bar{\tilde{\rho}}(t)$. Hence, it has memory and cannot represent a master equation [32]. Also, for the same reason an analytical solution to Eq. 2.24 is almost impossible. However, under some conditions it is possible to approximate Eq. 2.24 with another equation by replacing $\bar{\tilde{\rho}}(t')$ with $\bar{\tilde{\rho}}(t)$ which satisfies conditions of a Markovian process and allows for an analytical solution.

Typically, $F_m(t)F^*_{m'}(t')$ is a fast decaying function with a characteristic decay time τ_c. When the evolution time scale of $\tilde{\rho}(t)$ (in fact, the relaxation time T) is much longer than τ_c, then the replacement of $\tilde{\rho}(t')$ with $\tilde{\rho}(t)$ and the extension of the upper limit of the integration to infinity is justified. In addition, $T \gg \tau_c$ means each density matrix in the ensemble has already gone through evolution under the fluctuating relaxation Hamiltonian long enough such that $\bar{\tilde{\rho}}(t) = \tilde{\rho}(t)$. Also, in systems like lipid membranes where the net effect of molecular motions has axial symmetry, only auto-correlations with the same indices are non-vanishing *i.e.*, $G_{m,m'}(\tau) = \delta_{m,m'}G_{m,m}(\tau)$. Incorporating the above approximation and axial symmetry in Eq. 2.24 and transforming it back to the laboratory representation, the master equation of relaxation for the deuterium nucleus ensemble is obtained [31]:

$$\frac{d\rho(t)}{dt} = -i\left[\hat{H}_0, \rho(0)\right] - \omega_Q^2 \sum_m \int_0^\infty e^{im\omega_o\tau}\left[\hat{T}_m^{(2)}, \left[\hat{T}_m^{(2)\dagger}, (\rho(t) - \rho_{eq})\right]\right] G_{m,m}(\tau)\, d\tau \tag{2.27}$$

The above equation can be simplified further by rewriting it in terms of *spectral densities* which are defined as the Fourier transformation of the auto-correlations on positive time. Spectral densities associated with random functions $F_m(t)$ are defined as:

$$J_{m,m}(m\omega_0) = \int_0^\infty G_{m,m}(t)e^{im\omega_o t}\, dt \tag{2.28}$$

Also, reduced spectral densities can be introduced to separate the dynamical and structural information encoded in the spectral densities as:

$$J_{m,m}(m\omega_0) = G_{m,m}(0)j_{m,m}(m\omega_0) \tag{2.29}$$

Reduced spectral densities are Fourier transform of the reduced auto-correlation functions $g_{m,m'}(\tau)$ over positive time where reduced auto-correlations are defined by [24]:

$$G_{m,m}(\tau) = \left[\langle Y_{2,m}(\theta,\phi)Y^*_{2,m}(\theta,\phi)\rangle - |\langle Y_{2,m}(\theta,\phi)\rangle|^2\right] g_{m,m'}(\tau) \tag{2.30}$$

The advantage of using spectral densities is that the relaxation rates, as it will be shown, are linear combinations of the spectral densities. The spectral densities for a motion with a single correlation time τ_c will be:

$$J_{m,m}(m\omega_0) = G_{m,m}(0)\frac{\tau_c}{1+(m\omega_0\tau_c)^2} \tag{2.31}$$

Finally the master equation of relaxation becomes:

$$\frac{d\rho(t)}{dt} = -i\left[\hat{H}_0, \rho(0)\right] - \omega_Q^2 \sum_m \left[\hat{T}_m^{(2)}, \left[\hat{T}_m^{(2)\dagger}, (\rho(t) - \rho_{eq})\right]\right] J_{m,m}(m\omega) \tag{2.32}$$

Most of the time the evolution of the expectation value of some observable is desired rather than that of the density matrix itself. The expectation value of an observable $\hat{Q}$ is given by:

$$\langle\hat{Q}\rangle = Tr[\rho\hat{Q}]$$

For any time-independent observable $\hat{Q}$ the evolution of its expectation value is governed by:

$$\frac{d\langle\hat{Q}\rangle(t)}{dt} = -i\langle\left[\hat{Q}, \hat{H}_0\right]\rangle(0) - \omega_Q^2 \sum_m \left(\langle\left[\left[\hat{Q}, \hat{T}_m^{(2)}\right], \hat{T}_m^{(2)\dagger}\right]\rangle(t) - \langle\left[\left[\hat{Q}, \hat{T}_m^{(2)}\right], \hat{T}_m^{(2)\dagger}\right]\rangle_{eq}\right) J_{m,m}(m\omega_0) \tag{2.33}$$

where $\langle\hat{Q}\rangle_{eq} = Tr[\hat{Q}\rho_{eq}]$ and $\langle\hat{Q}\rangle(t) = Tr[\hat{Q}\rho(t)]$. For example, the evolution of the longitudinal magnetization as the expectation value of $\hat{I}_z$ operator is given by:

$$\frac{d\langle\hat{I}_z\rangle(t)}{dt} = -\omega_Q^2 \sum_m \left(\langle\left[\left[\hat{I}_z, \hat{T}_m^{(2)}\right], \hat{T}_m^{(2)\dagger}\right]\rangle(t) - \langle\left[\left[\hat{I}_z, \hat{T}_m^{(2)}\right], \hat{T}_m^{(2)\dagger}\right]\rangle_{eq}\right) J_{m,m}(m\omega_0) \tag{2.34}$$

Finally, it should be noticed that in the derivation of the master equation non-secular parts of the averaged quadrupole Hamiltonian have been neglected which based on the dominance of Zeeman Hamiltonian in $\hat{H}_0$ is expected to not appreciably affect the master equation of relaxation and its solutions.

2.2.3 Solutions of the Master Equation

The master equation of relaxation for deuterium nuclei (Eq. 2.32) is a coupled first-order linear ordinary differential equation. This differential equation can be solved in two ways, either by going through the routine way of solving ODEs by means of Laplace transformation, or by finding a basis for the density matrix that decouples the differential equation (at least partially).

When $\hat{H}_0$ is proportional to $\hat{I}_z$ operator (neglecting the averaged quadrupole Hamiltonian), spin-1 basis operators given in Table 2.3 decouple the master equation [33].

$$P_1 = \frac{1}{\sqrt{2}}\hat{I}_x \quad , \quad P_2 = \frac{1}{\sqrt{2}}\hat{I}_y \quad , \quad P_3 = \frac{1}{\sqrt{2}}\hat{I}_z$$

$$P_4 = \frac{1}{\sqrt{6}}(3\hat{I}_z^2 - 2)$$

$$P_5 = \frac{1}{\sqrt{2}}(\hat{I}_x\hat{I}_z + \hat{I}_z\hat{I}_x) \quad , \quad P_6 = \frac{1}{\sqrt{2}}(\hat{I}_y\hat{I}_z + \hat{I}_z\hat{I}_y)$$

$$P_7 = \frac{1}{\sqrt{2}}(\hat{I}_x^2 - \hat{I}_y^2) \quad , \quad P_8 = \frac{1}{\sqrt{2}}(\hat{I}_x\hat{I}_y + \hat{I}_y\hat{I}_x)$$

Table 2.3: **Spin-1 basis operators**

The commutation relations between the operators of Table 2.3 are given in Table 2.4.

Table 2.5 represents the expansion of the 2^{nd}-rank irreducible tensor operators in terms of the basis operators of Table 2.3. For instance, from the above commutation relations and Eq. 2.34 and Tables 2.3, 2.4, 2.5 the longitudinal relaxation rate can be determined:

$$\frac{1}{T_1} = 4\omega_Q^2(J_{1,1}(\omega_0) + 4J_{2,2}(2\omega_0)) \tag{2.35}$$

Similarly the transverse relaxation rate will be:

$$\frac{1}{T_2} = 2\omega_Q^2(3J_{0,0}(0) + 3J_{1,1}(\omega_0) + 2J_{2,2}(2\omega_0)) \tag{2.36}$$

When there are terms containing $\hat{I}_z^2$ in $\hat{H}_0$ the basis functions of Table 2.3 fail to decouple the master equation. However, it is still possible to write the density matrix ρ as a linear combination of these basis operators and then solve the resultant linear set of equations. Alternatively, Laplace transformation can be applied to the master equation which implicitly uses another basis operators. The density matrix of deuterium nuclei system is a 3×3 Hermitian, traceless matrix whose entries can be determined by eight time-dependent real functions.

$$\rho = \begin{pmatrix} \rho_{11} & \rho_{12} + i\varrho_{12} & \rho_{13} + i\varrho_{13} \\ \rho_{12} - i\varrho_{12} & \rho_{22} & \rho_{23} + i\varrho_{23} \\ \rho_{13} - i\varrho_{13} & \rho_{23} - i\varrho_{23} & 1 - (\rho_{11} + \rho_{22}) \end{pmatrix}$$

Then the master equation of relaxation can be written explicitly in these eight real

	P_1	P_2	P_3	P_4	P_5	P_6	P_7	P_8
P_1	0	P_3	$-P_2$	$-\sqrt{3}P_6$	$-P_8$	$\sqrt{3}P_4+P_7$	$-P_6$	P_5
P_2	$-P_3$	0	P_1	$\sqrt{3}P_5$	$-\sqrt{3}P_4+P_7$	P_8	$-P_5$	$-P_6$
P_3	P_2	$-P_1$	0	0	P_6	$-P_5$	$2P_8$	$-2P_7$
P_4	$\sqrt{3}P_6$	$-\sqrt{3}P_5$	0	0	$\sqrt{2}P_2$	$-\sqrt{3}P_1$	0	0
P_5	P_1	$\sqrt{3}P_4-P_7$	$-P_6$	$-\sqrt{3}P_2$	0	P_3	P_2	$-P_1$
P_6	$-\sqrt{3}P_4-P_7$	$-P_8$	P_5	$\sqrt{3}P_1$	$-P_3$	0	P_1	P_2
P_7	P_6	P_5	$-2P_8$	0	$-P_2$	$-P_1$	0	$2P_3$
P_8	$-P_5$	P_6	$2P_7$	0	P_1	$-P_2$	$-2P_3$	0

Table 2.4: **Commutation relations between spin-1 basis operators** (given in Table 2.3)

functions.

$$\frac{d}{dt}\begin{pmatrix}\rho_{11}(t)\\ \rho_{22}(t)\\ \rho_{12}(t)\\ \rho_{13}(t)\\ \rho_{23}(t)\\ \varrho_{12}(t)\\ \varrho_{13}(t)\\ \varrho_{23}(t)\end{pmatrix} = \mathcal{M}\begin{pmatrix}\rho_{11}(t)\\ \rho_{22}(t)\\ \rho_{12}(t)\\ \rho_{13}(t)\\ \rho_{23}(t)\\ \varrho_{12}(t)\\ \varrho_{13}(t)\\ \varrho_{23}(t)\end{pmatrix} \tag{2.37}$$

where $\mathcal{M}$ is the 8×8 kernel of the re-written master equation in the basis of those eight real functions. Using Laplace transformation, solving the master equation of relaxation reduces to solving an eigenvalue/eigenvector problem with relaxation rates given by the real part of solutions of:

$$det(\mathcal{M} - \lambda I) = 0 \tag{2.38}$$

For $\hat{H}_0 = \omega_0 \hat{I}_z + \epsilon(3\hat{I}_z^2 - \hat{I}^2)$ the relaxation rates obtained from Eq. 2.32 will be given by the real part of the evolution frequencies given in Table: 2.6. with basis operators given in Table: 2.6 that decouple the master equation of relaxation when the secular part of the quadrupole Hamiltonian hasn't been neglected:

These eigenstates are neither orthonormal nor real, but real orthonormal basis function can be constructed from their linear combinations. Such combinations are automatically realized to meet the boundary conditions at $t = 0$.

$$\hat{T}^{(2)}_{\pm 2} = \sqrt{2}(P_7 \pm iP_8)$$

$$\hat{T}^{(2)}_{\pm 1} = \mp\sqrt{2}(P_5 \pm iP_6)$$

$$\hat{T}^{(2)}_{0} = 2P_4$$

Table 2.5: **2^{nd}-rank irreducible operators in terms of Table 2.3**

2.2.4 Orientation-dependence of Relaxation Rates

As in de-Pakeing problem where the determination of segmental order parameters is desired regardless of the orientation of microscopic domains, in finding relaxation rates desired quantities are the averages of auto-correlations $G_{m,m}(0)$ and the reduced spectral densities $j_{m,m}(m\omega_0)$. Orientation dependence of spectral densities $J_{m,m}(m\omega_0)$ arises from the orientation dependence of spherical harmonics through $G_{m,m}(0)$. Following the same two step transformation approach from the local molecule-bond system of reference to the laboratory frame that was used in determining the orientation dependence of the quadrupole splitting and using the transformation rule for spherical harmonics (Eq. 2.10) the orientation dependence of auto-correlations and therefore spectral densities can be determined.

Assuming no correlation between motions with different correlation times, spectral densities can be written in the form of Eq. 2.31. The only orientation dependent parts of spectral densities in this form are $G_{m,m}(0)$. Hereafter subscripts "*domain*" and "*LAB*" will be used to distinguish $G_{m,m}(0)$ in molecule-bond system of reference from the laboratory frame. The transformation of auto-correlations from the local molecule-bond system to the laboratory system can be written as:

$$G_{m,m'}(0)_{LAB} = \sum_{n=-2}^{2} \sum_{n'=-2}^{2} D^{(2)}_{n,m}(\alpha,\beta,\varphi) \left(D^{(2)}_{n',m'}(\alpha,\beta,\varphi)\right)^* G_{n,n'}(0)_{domain} \qquad (2.39)$$

where α, β, and φ are the Euler angels of the transformation. Following the same line of reasoning that led to Eq.2.13 and considering anisotropic motional averaging, the above equation reduces to:

$$\lambda_1 = -12\omega_Q^2 J_1(\omega_0) \quad , \quad \lambda_2 = -16\omega_Q^2 J_2(2\omega_0) - 4\omega_Q^2 J_1(\omega_0)$$

$$\lambda_3 = -4\omega_Q^2 J_1(\omega_0) - 8\omega_Q^2 J_2(2\omega_0) + 2i\omega_0$$

$$\lambda_4 = -8\omega_Q^2 J_2(2\omega_0) - 4\omega_Q^2 J_1(\omega_0) - 2i\omega_0$$

$$\lambda_5 = -4\omega_Q^2 J_2(2\omega_0) - 6\omega_Q^2 J_1(\omega_0) - 6\omega_Q^2 J_0(0) + i\omega_0 - \sqrt{16J_1^2 - \epsilon^2}$$

$$\lambda_6 = -4\omega_Q^2 J_2(2\omega_0) - 6\omega_Q^2 J_1(\omega_0) - 6\omega_Q^2 J_0(0) + i\omega_0 + \sqrt{16J_1^2 - \epsilon^2}$$

$$\lambda_7 = -6\omega_Q^2 J_0(0) - 4\omega_Q^2 J_2(2\omega_0) - 6\omega_Q^2 J_1(\omega_0) - i\omega_0 - \sqrt{16J_1^2 - \epsilon^2}$$

$$\lambda_8 = -6\omega_Q^2 J_0(0) - 4\omega_Q^2 J_2(2\omega_0) - 6\omega_Q^2 J_1(\omega_0) - i\omega_0 + \sqrt{16J_1^2 - \epsilon^2}$$

Table 2.6: **Evolution frequencies**

$$G_{m,m}(0)_{LAB} = \sum_{n=-2}^{2} \left[D^{(2)}_{n,m}(\alpha, \beta, 0)\right]^2 G_{n,n}(0)_{domain} \tag{2.40}$$

Since the entries of the Wigner d-matrix in Euler transformations with the "z-y-z" convention are all real, the above equation simplifies to:

$$G_{m,m}(0)_{LAB} = \sum_{n=-2}^{2} \left[d^{(2)}_{n,m}(\beta)\right]^2 G_{n,n}(0)_{domain} \tag{2.41}$$

where again β is the angle between the symmetry axis of fluctuations and the $\hat{z}$ direction of the laboratory frame.

The orientation dependence of longitudinal relaxation rate $\frac{1}{T_1}$ based on the above orientation dependence of $G_{m,m}(0)$ will be:

$$\frac{1}{T_1}_{LAB} = 4\omega_Q^2 \left[j_{1,1}(\omega_0) G_{1,1}(0)_{LAB} + 4j_{2,2}(2\omega_0) G_{2,2}(0)_{LAB}\right]$$

$$\rho_1 = \begin{pmatrix} 1 & 0 & 0 \\ 0 & -2 & 0 \\ 0 & 0 & 1 \end{pmatrix} \quad , \quad \rho_2 = \begin{pmatrix} 1 & 0 & 0 \\ 0 & 0 & 0 \\ 0 & 0 & -1 \end{pmatrix}$$

$$\rho_3 = \begin{pmatrix} 0 & 0 & 0 \\ 0 & 0 & 0 \\ 1 & 0 & 0 \end{pmatrix} \quad , \quad \rho_4 = \begin{pmatrix} 0 & 0 & 1 \\ 0 & 0 & 0 \\ 0 & 0 & 0 \end{pmatrix}$$

$$\rho_5 = \begin{pmatrix} 0 & 0 & 0 \\ 1 & 0 & 0 \\ 0 & \frac{4J_1}{\sqrt{16J_1^2-\epsilon^2}-i\epsilon} & 0 \end{pmatrix} \quad , \quad \rho_6 = \begin{pmatrix} 0 & 0 & 0 \\ 1 & 0 & 0 \\ 0 & \frac{-4J_1}{\sqrt{16J_1^2-\epsilon^2}+i\epsilon} & 0 \end{pmatrix}$$

$$\rho_7 = \begin{pmatrix} 0 & 1 & 0 \\ 0 & 0 & \frac{4J_1}{\sqrt{16J_1^2-\epsilon^2}+i\epsilon} \\ 0 & 0 & 0 \end{pmatrix} \quad , \quad \rho_8 = \begin{pmatrix} 0 & 1 & 0 \\ 0 & 0 & \frac{-4J_1}{\sqrt{16J_1^2-\epsilon^2}-i\epsilon} \\ 0 & 0 & 0 \end{pmatrix}$$

Table 2.7: **The basis operators for the master equation with secular part of the quadrupole Hamiltonian**

$$= 4\omega_Q^2 \left[j_{1,1}(\omega_0) \sum_{n=-2}^{2} \left[d_{n,1}^{(2)}(\beta) \right]^2 G_{n,n}(0)_{domain} + 4 j_{2,2}(2\omega_0) \sum_{n=-2}^{2} \left[d_{n,2}^{(2)}(\beta) \right]^2 G_{n,n}(0)_{domain} \right] \tag{2.42}$$

For fast motions ($\tau_c\omega_0 \ll 1$), reduced spectral densities can be assumed to be the same for all three spectral densities and equal to $j_{0,0}(0)$ which is ω_0 independent. With this approximation the transformation equation simplifies to:

$$\frac{1}{T_1}_{LAB} = 4\omega_Q^2 j_{0,0}(0) \left[\sum_{n=-2}^{2} \left[d_{n,1}^{(2)}(\beta) \right]^2 G_{n,n}(0)_{domain} + 4 \sum_{n=-2}^{2} \left[d_{n,2}^{(2)}(\beta) \right]^2 G_{n,n}(0)_{domain} \right] \tag{2.43}$$

Indicating spectral densities at $\beta = 0^o$, which are also referred to as relaxation parameters, with $J_{0,0}(0)|_{\beta=0}$, $J_{1,1}(\omega_0)|_{\beta=0}$, and $J_{2,2}(2\omega_0)|_{\beta=0}$, the longitudinal relaxation rate at any orientation can be written as a linear combination of these relaxation parameters in the following way:

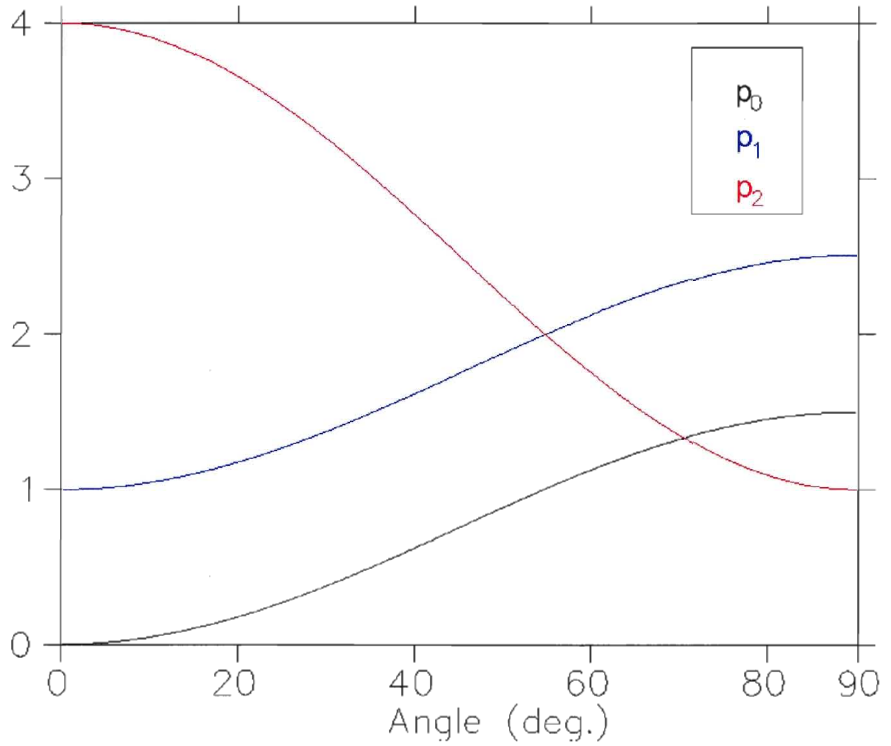

Figure 2.6: **Functionality of the three scaling functions of longitudinal relaxation rate, $p_0(\beta)$, $p_1(\beta)$, and $p_2(\beta)$**

$$\frac{1}{T_1} = p_0(\beta)J_{0,0}(0)|_{\beta=0} + p_1(\beta)J_{1,1}(\omega_0)|_{\beta=0} + p_2(\beta)J_{2,2}(2\omega_0)|_{\beta=0} \tag{2.44}$$

where the scaling functions $p_0(\beta)$, $p_1(\beta)$, and $p_2(\beta)$ can be determined from Table 2.2, Eq. 2.43 :

$$p_0(\beta) = \frac{3}{2}\sin^2\beta \qquad p_1(\beta) = 1 + \frac{3}{2}\sin^2\beta \qquad p_2(\beta) = 1 + 3\cos^2\beta \tag{2.45}$$

The orientation dependence of these three orientation scaling functions is shown in Fig 2.6. It should be noted that other ways of parameterizing the orientation dependence of relaxation rates are possible. For example, the first three even Legendre polynomials have been suggested as a general basis functions for the orientation de-

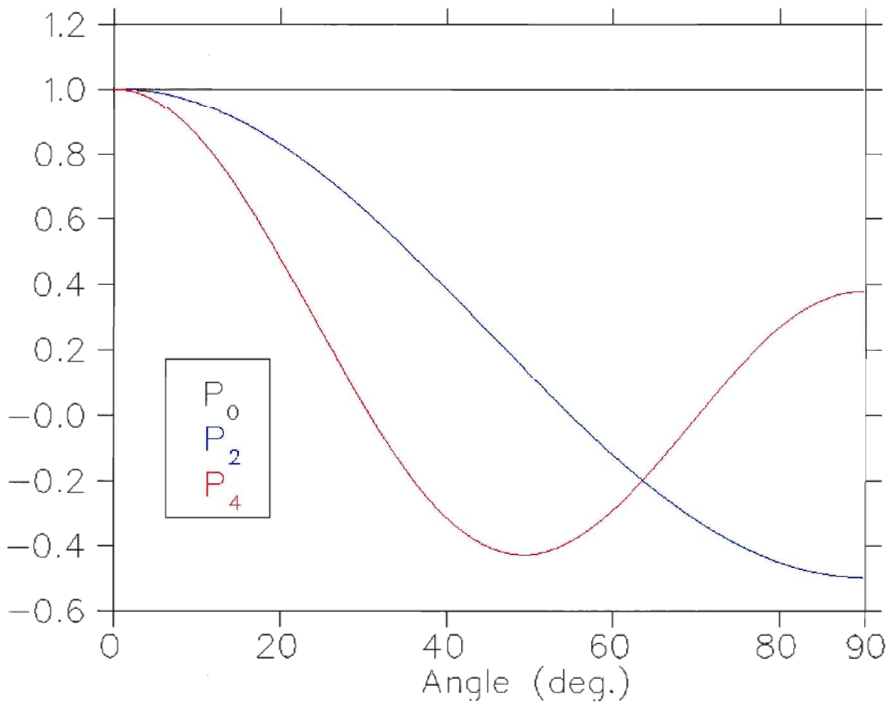

Figure 2.7: **The first three even Legendre polynomials** as candidate basis for representing a general orientation dependence of relaxation rates.

pendence of relaxation rates [4] as:

$$\frac{1}{T_1} = C_0 P_0(\cos(\beta)) + C_2 P_2(\cos(\beta)) + C_4 P_4(\cos(\beta)) \tag{2.46}$$

where,

$$P_0(\cos(\beta)) = 1 \quad , \quad P_2(\cos(\beta)) = \frac{3}{2}\cos^2(\beta) - \frac{1}{2}$$
$$P_4(\cos(\beta)) = \frac{35}{8}\cos^4(\beta) - \frac{15}{4}\cos^2(\beta) + \frac{3}{8} \tag{2.47}$$

Fig 2.7 depicts these three Legendre polynomials.

2.3 Relaxation and Order Profiles of Lipids in the L_α Phase

Molecular motions in deuterated lipid bilayers average the quadrupole Hamiltonian over motions with correlation times shorter than the NMR time scale; and give rise to the appearance of relaxation due to the stochastic time-dependence of the quadrupole Hamiltonian, and as a result, to non-zero spectral densities. The time averaging of the quadrupole interaction can only differentiate fast from slow motions: any motion with a correlation time longer than the NMR time scale results in averaging the observables of the averaged quadrupole Hamiltonian over fast motions. On the other hand, according to the spin-lattice relaxation theory the only thing that matters to relaxation is the correlation time of the motion, τ_c, compared to ω_0^{-1}. Care must be taken in treating the effect of very slow motions on relaxation through the master equation which gives a valid description of relaxation as long as the decay time, T, of auto-correlations satisfies $\tau_c \ll T$.

Since relaxation emerges from averaging the incoherent evolution of spins over an ensemble, it is crucial to properly define the ensemble in formulating relaxation. This definition itself depends on the time scale of the experiment and the correlation times of various motional modes. In an extreme case of the time scale of the experiment and observation being long enough to allow lateral diffusion to completely mix all orientations, the ensemble will be the whole system. It should be noted that the preceding description of spin-lattice relaxation based on the relaxation Hamiltonian of the Eq. 2.17 is merely based on disregarding slow motions.

2.3.1 A Puzzle

From the structure of lipid bilayers in the L_α phase, it is expected that segments close to the end of hydrocarbon chains of lipids experience more extensive fluctuations. Indeed, all experiments with oriented or powder samples of various lipids indicate a decreasing segmental order parameter along the chain. This characteristic order parameter profile typically has a plateau region corresponding to carbon positions on roughly the upper half of the chain, and a rapidly decreasing region associated with segments on the lower half of the chain [4, 10, 6]. This plateau region is not seen for lipids in the hexagonal H_{II} phase, which suggests geometrical and packing origins for the presence of this plateau region in the L_α phase (Fig. 2.9). Also, it can be anticipated that increasing the temperature results in more pronounced fluctuations and thus smaller overall order parameters. This agrees with experimental results.

When there are no correlations between motions with different correlation times, auto-correlations can be written as linear combinations of exponentially decaying functions with different decay rates associated with various motional modes and the spectral densities can be written as:

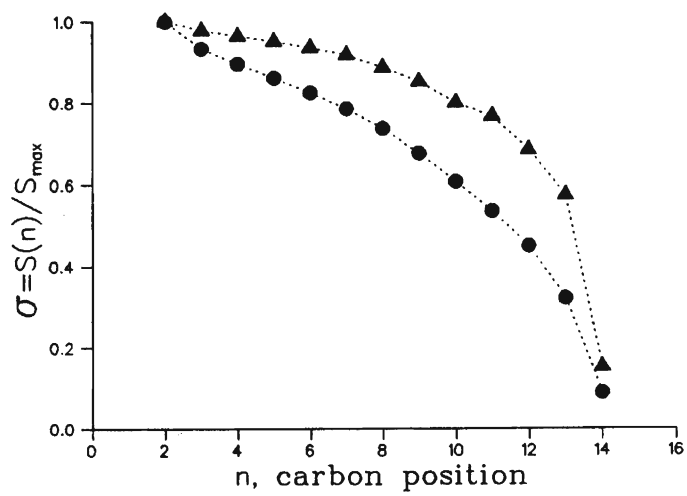

Figure 2.8: **Normalized segmental order parameter profiles of lipids in L_α ($\triangle$) and H_{II} ($\bullet$) phases** (reproduced from [4]).

$$J_{m,m}(m\omega_0) = \sum_N G^{(N)}_{m,m}(0) \frac{\tau_c^{(N)}}{1 + (m\omega_0 \tau_c^{(N)})^2} \tag{2.48}$$

where N is the index of the modes of motions characterized by correlation times $\tau_c^{(N)}$ [6]. Each term in the above equation corresponds to a spectral density for a single correlation time (Eq. 2.31). The dependence of auto-correlations and spectral densities of the form of Eq. 2.31 on the correlation time is represented in Fig. 2.9. Following the same line of reasoning as above and assuming no significant difference in the nature of fast intramolecular motions at different carbon positions, it can be expected that since segments down the chain have a smaller order parameter, they should possess more extensive fluctuations and hence bigger spectral densities and faster relaxation. In addition, it can also be argued that analogous to the effect of increasing temperature on the order parameter, relaxation rates associated with different segments along the chain should increase as the temperature increases.

Surprisingly, the relaxation rates of segments close to the end of the hydrocarbon chains are slower than those of sites close to the head group region; and also as the temperature increases the relaxation rates tend to decrease (Fig. 2.10 and Fig. 2.11) [6, 5, 24].

All experiments indicate that the relaxation profile follows the order profile and has the same plateau region or, more precisely, that the relation between the relaxation rate and the square of the order parameter, S^2_{CD}, is linear within experimental errors [6]. Despite the fact that the relation between the spectral densities and molecular motions is more complicated than that of the order parameter, such a significant discord is surprising.

From Figure 2.9b it can be seen that for the intermediate correlation time regime marked by τ_c comparable to ω_0^{-1}, T_1, the relaxation time assumes its minimum and the relaxation is very effective. In the short correlation time regime, as the correlation time decreases, either through increasing temperature or through going down the chain where van der Waals attractions are weaker, the relaxation rate increases. The opposite effect is expected in the long correlation time regime. On this basis, one may argue that increasing the temperature results in shorter correlation times and thus longer relaxation time T_1. Applying the same logic to the case of relaxation profile and assuming the dominance of the change in the correlation times of motions, τ_c, over the extent of motions, $G_{m,m}(0)$, along the chain, the descending relaxation profile of lipid bilayers in the L_α phase can be rationalized. However, numerical values for the longitudinal relaxation rates suggest correlation times much shorter than ω_0^{-1} which is in direct conflict with the experimentally observed decrease in longitudinal relaxation rates as the Larmor frequency increases.

Typically the longitudinal relaxation rate in lipid bilayers is on the order of tens of milliseconds [4, 24, 6] while the transverse relaxation is one the order of tens of microseconds [4, 33]. These values suggest a very short-correlation-time regime, since defining spectral densities for a single correlation time, as in Eq. 2.31 yields

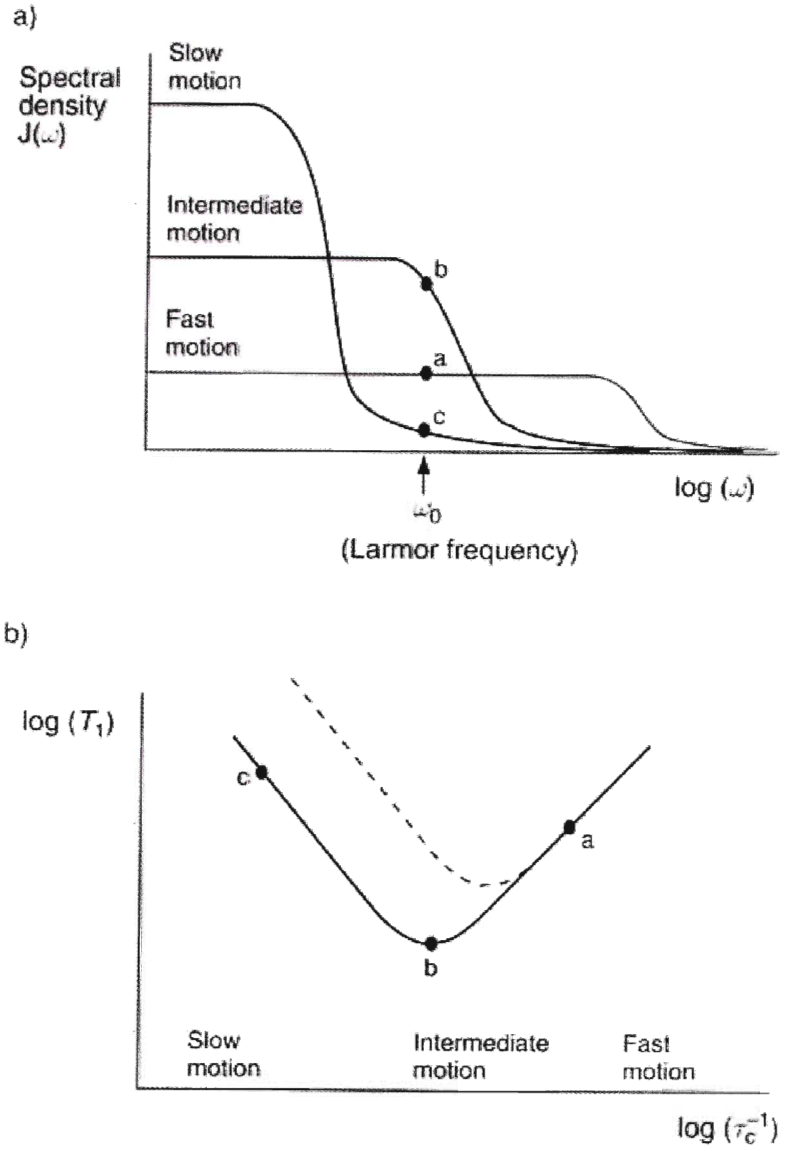

Figure 2.9: **Spectral density and longitudinal relaxation rate dependence on** τ_c: (a) The spectral densities as a function of the Larmor frequency. (b) The longitudinal relaxation rate T_1 as a function of molecular motions rate (τ_c^{-1}). The dashed line represents T_1 functionality for a higher Larmor frequency. Fast and slow motions here are designated based on their correlation time compared to the ω_0^{-1} which is typically much shorter than the NMR time scale. The curves are calculated under the assumption that a single random motion with a correlation time τ_c causes relaxation. Reproduced from [25].

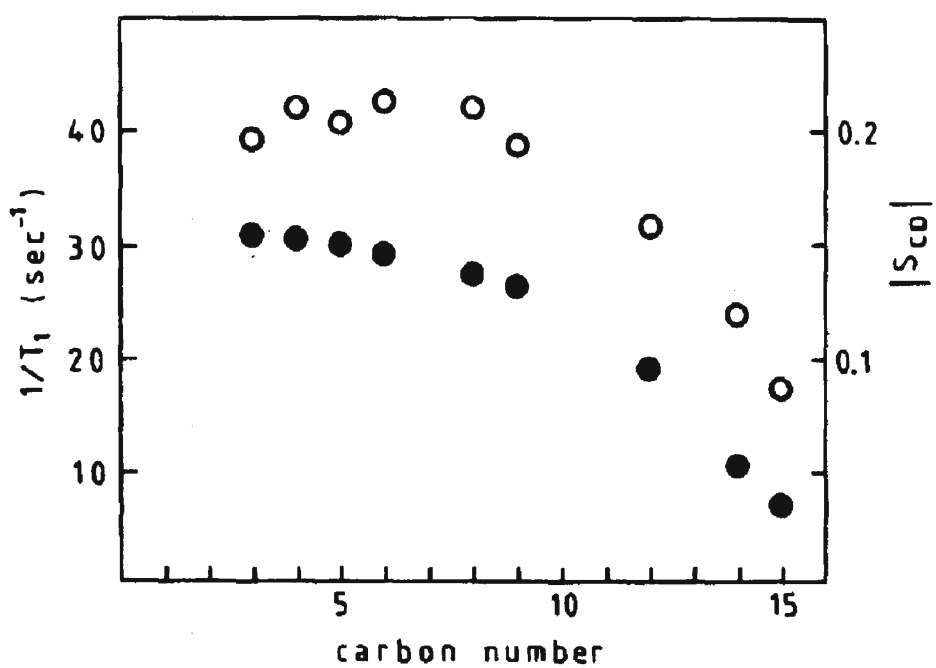

Figure 2.10: **Relaxation and order profiles of DPPC** Comparison between relaxation rates (•) and segmental order parameters (○) at 51°C (reproduced from [34]).

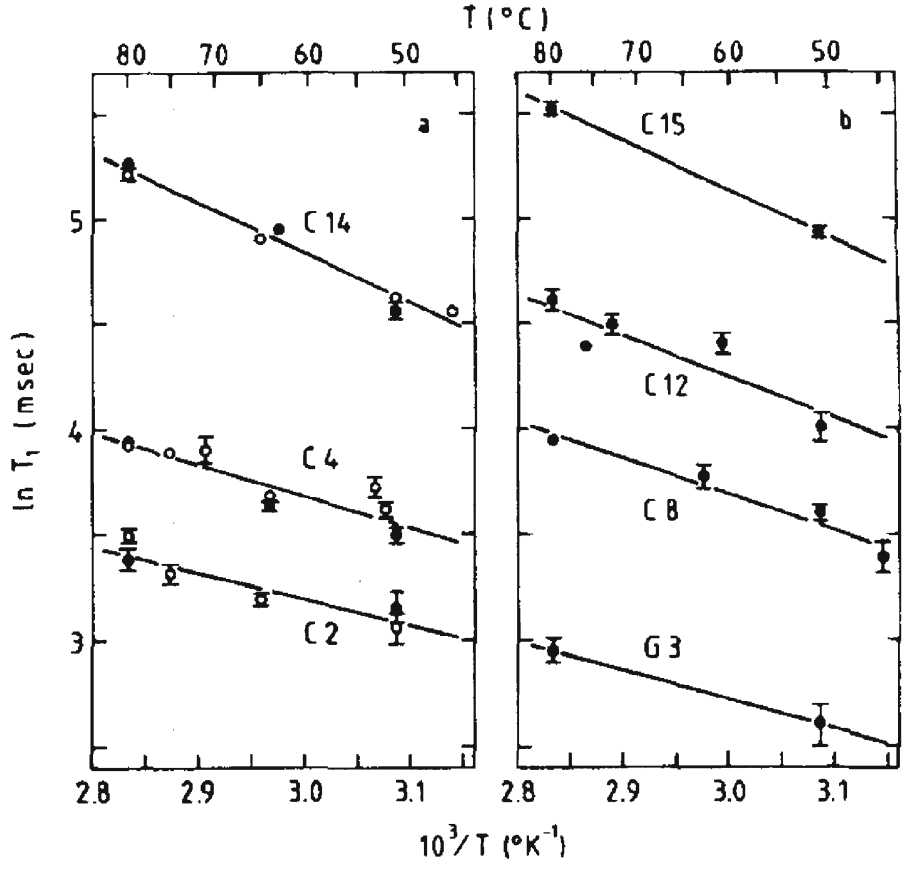

Figure 2.11: **Relaxation time T_1 versus temperature for various carbon positions in DPPC**(reproduced from [5]).

comparable relaxation rates for longitudinal and transverse relaxations.

2.3.2 Non-Collective versus Collective Models for Slow Motions

It has been suggested that [7] when there is no correlation between motions, fast and slow motions (on the NMR time scale) contribute to the longitudinal relaxation rate differently:

$$\frac{1}{T_1} = \frac{1}{T_{1f}} + \frac{1}{T_{1s}} \tag{2.49}$$

where $1/T_{1f}$ and $1/T_{1s}$ are the contributions from the fast and slow motions, respectively. The fast motion is treated as a single correlation rate motion, while it has been advocated that slow motions result in direct averaging of relaxation rates [6]. Slow motions in this treatment are assumed to have correlation times longer than ω_Q^{-1} but still much shorter than the relaxation time T_1. Two models for slow motions can be considered: (*i*) *non-collective models* in which each of the slow motions can be described with a single correlation time, without explicitly considering long-range cooperative motions; and (*ii*) *collective models* where slow motions are described by a continuous distribution of, for instance, bilayer disturbances. It has been shown in [6] that unlike the non-collective models which result in ω_0^{-2} dependence, the collective models give rise to $\omega_0^{-\frac{1}{2}}$ dependence.

Experimentally observed linear dependence of relaxation rates on S_{CD} has been explained by averaging the orientation-dependent relaxation rates due to fast motions. This averaging results in S_{CD}^2 dependence [7].

2.3.3 Resolution

Interpretation of experimentally measured longitudinal relaxation rates as a function of the Larmor frequency is not without difficulty. Initial reports concluded that $\omega_0^{-\frac{1}{2}}$ represents a better fit to the data and hence that collective motions are the dominant mechanism for the longitudinal relaxation in the long-correlation-time regime [35]. Later, more precise investigations along with the data from ^{1}H relaxation led to the interpretation that the longitudinal relaxation rates of ^{2}H NMR spectra exhibit a ω_0^{-2}-dependence on the Larmor frequency and there is no need to appeal to collective models for slow motions to explain the relaxation phenomena in lipid bilayers [36, 37, 38].

It was therefore concluded that two types of molecular motions are mainly responsible for the relaxation in lipid bilayers: motions in the very short correlation time regime and non-collective motions in the intermediate or long correlation time regime, with the latter contributing only to the transverse relaxation. In this way, large differences between the longitudinal and transverse relaxation rates in lipid bilayers can

be explained.

Chapter 3

Ill-posed Inverse Problems and Regularization

Inverse problem, in the sense of Eqs. 1.2 or 1.3, where the distribution of, say, anisotropies $g(\nu)$ needs to be extracted from the measured data, $f(\omega)$, presents unique computational challenges [39]. The two central difficulties are: (i) typically, the determination of model parameters from data in non-linear inverse problems requires direct search of the parameter space which poses a serious difficulty as the number of model parameters increases; and (ii) most of the inverse problems, regardless of being linear or non-linear, are not *well-posed*. In mathematics a well-posed problem is defined to have the following properties [40] :

1. For all admissible data, a solution exists
2. For all admissible data, the solution is unique
3. The solution depends continuously on data and is stable, namely, arbitrarily small variation of coefficients, parameters, initial or boundary conditions, *etc.*, gives rise to small solution changes.

Consequently, any problem that fails to fulfill even one of these criteria is considered an ill-posed problem.

Thus ill-posed problems may not possess a unique or stable solution. However, instead of finding an exact solution, one might modify the inverse problem slightly by imposing some external constraints such as non-negativity, smoothness, *etc.*, on its expected solution in order to construct a stable pseudo-inverse solution. Methods and algorithms implemented to improve stability of ill-posed pseudo-inverse solutions are known as *regularization techniques*. It should be noted that among all ill-posed problems those which arise from the violation of the third condition are the most problematic ones.

Ill-posed inverse problems are abundant in real-world problems. They are frequently encountered in astronomy, geophysics, high-energy physics, and in all disciplines requiring data analysis. Paradoxically, even some mathematicians like Hadamard, who himself pioneered the concept of ill-posed problems, believed that ill-posed problems are artificial and irrelevant to real physical systems [41]. However, if one overcomes this bias, pseudo-inverse solutions offer a powerful tool for making progress in data-analysis that seen intractable at first.

3.1 Discrete Linear Ill-posed Problems

Most of the inverse problems arising in physics are structurally linear and usually in the form of convolution integral equations. An important class of such problems are Fredholm integral equations the of 1^{st}-kind that can be written in the following generic form:

$$\int K(s,t)g(t)\,dt = f(s) \tag{3.1}$$

where $f(s)$ is the available distribution (measured data) and $g(t)$ is the unknown distribution (desired parameters) that needs to be determined. $K(s,t)$ is called the kernel of the integral equation and is known. As can be readily shown, Eq. 3.1 does not possess a unique solution. If $g_{\text{ans}}(t)$ is an answer to the above equation then any $g_{\text{ans}}(t) + ag_{\text{null}}(t)$ will also be a solution where a is a real number and $g_{\text{null}}(t)$ is a null solution to 3.1:

$$\int K(s,t)g_{\text{null}}(t)\,dt = 0 \tag{3.2}$$

It is possible to get around the non-uniqueness of the solution by confining possible solutions to a subspace of the whole solution space by disregarding null solutions. However, as a direct result of it being an integral equation, not only Eq. 3.1 does not have a unique solution, but also the non-unique solutions are highly unstable. To see the origin of this instability, consider the effect on $g(t)$ of adding an oscillating function $n(s)$ with vanishing average to $f(s)$ in Eq. 3.1. If oscillations of $n(s)$ are much faster than the scale over which $K(s,t)$ as a function of s changes appreciably then the integration will averaging them out. Hence, small changes in $f(s)$ may correspond to large fluctuations in $g(t)$, leading to an instability. In practice, a discretized version of Eq. 3.1 is used:

$$\sum_j K(s_i,t_j)g(t_j) = f(s_i) \tag{3.3}$$

or using $K_{i,j} = K(s_i,t_j)$ and $\vec{f} = \{f(s_i)\}$, $\vec{g} = \{g(t_j)\}$, for a discrete set of $\{s_i\}$, $\{t_j\}$ values, Eq. 3.3 can be written in a more compact form as:

$$K\vec{g} = \vec{f} \tag{3.4}$$

It should be noted that the sizes of the sets of $\{s_i\}$ and $\{t_j\}$ are not completely arbitrary. A fine-grid discretized $g(t_j)$ combined with a coarse-grid $f(s_i)$ results in an under-determined problem which will be severely ill-posed. On the other hand, choosing a more coarse-grid discretization of $g(t_j)$ may address the severe instability of the original problem, but at the same time, its loss of flexibility may introduce errors in compatibility with $f(s_i)$. In fact, discretization itself is an elementary and often not very effective way of regularizing an inverse ill-posed problem.

Despite the fact that finite-dimensional linear maps, like K in Eq. 3.4, are continuous in rigorous mathematical terms, they still can result in a numerically unstable problem. To make this point more clear and gain more insight into the behavior of finite dimensional linear equations it is necessary to first transform the kernel to a more manageable form. This transformation is provided by the *singular value decomposition.*

3.2 Singular Value Decomposition

Singular value decomposition (SVD) is a powerful tool in linear algebra for solving sets of linear equations, *least squares* (LS) problems, and constructing *pseudo-inverse* solutions when the exact solution doesn't exist. According to SVD theorem, any arbitrary $m \times n$ matrix K can be decomposed into a diagonal matrix $\Sigma_{m\times n}$ and two left and right unitary matrices $U_{m\times m}$ and $V_{n\times n}$:

$$K_{m\times n} = U_{m\times m} \begin{pmatrix} \sigma_{11} & 0 & \cdots \\ 0 & \sigma_{22} & \\ \vdots & & \ddots \end{pmatrix}_{m\times n} V^{\dagger}_{n\times n} \tag{3.5}$$

Any simultaneous substitution of ith with jth rows of U, V and σ_{ii} with σ_{jj} in Σ results in a valid SVD of the original matrix K. Because of this arbitrariness in the order of singular values, SVD transformation is conventionally defined in a way that singular values decrease from top-left to the bottom-right corner of the transformed matrix Σ. Since the rows of unitary matrices U and V are nothing but the left and right eigenvectors of the matrix K (including null vectors), the SVD can be rewritten in a more explicit form :

$$K_{m\times n} = \sum_{i=1}^{\min\{m,n\}} \vec{u}_i \sigma_{ii} \vec{v}_i^{\dagger} \tag{3.6}$$

Because the left and right eigenvectors of K form two orthonormal basis vectors for m- and n- dimensional spaces that K acts between, the solution to any LS problem of the form $\vec{f} = K\vec{g}$ can be written as:

$$\vec{g} = \sum_{i=1}^{\min\{m,n\}} \sigma_{ii}^{-1} (\vec{u}_i . \vec{f})\, \vec{v}_i \tag{3.7}$$

Accordingly, the pseudo-inverse matrix K^{-1} is defined as:

$$K^{-1} = V(\Sigma^{-1})^{\dagger} U^{\dagger} \tag{3.8}$$

where Σ^{-1} is a matrix whose non-zero, diagonal elements are the reciprocal of the diagonal elements of Σ. Since the pseudo-inverse of an invertible square matrix hap-

pens to be exactly the inverse matrix, the pseudo-inverse matrix can be considered as a generalized inverse matrix. In fact, Eq. 3.7 is the definition of *Moore-Penrose generalized inverse* matrix. Ortho-normality of the right and left eigenvectors of the matrix ensures that the answer obtained from Eq. 3.7 gives the best fit to the data vector $\vec{f}$, in the sense of having the least possible mismatch norm.

Instability emerges in constructing the solution $\vec{g}$ from the data $\vec{f}$ when the kernel K is ill-conditioned. A matrix is considered ill-conditioned when it has a big *condition number*. The condition number for any matrix is defined as the ratio of relative error introduced in $\vec{g}$ by adding a perturbation vector $\vec{n}$ to $\vec{f}$, to the relative error in $\vec{f}$:

$$\text{Cond}(K) = \frac{\|K^{-1}\vec{n}\|/\|K^{-1}\vec{f}\|}{\|\vec{n}\|/\|\vec{f}\|} \tag{3.9}$$

By virtue of SVD, the condition number can be expressed only in singular values as the ratio of the biggest to the smallest non-zero singular value of K as following:

$$\text{Cond}(K) = \frac{\sigma_{\max}}{\sigma_{\min}} \tag{3.10}$$

Clearly, a bigger condition number of the kernel K in the linear inverse problem $K\vec{g} = \vec{f}$ results in a more severe instability in the solution $\vec{g}$. In fact all small singular values give rise to the amplification of components with many sign changes which is analogous to the high frequency amplification effect of the original un-discretized inverse integral equation (Eq. 3.1). Zero singular values in the SVD of any matrix are the indication of the linear dependence of corresponding rows or columns of the matrix. The number of such zero singular values defines the dimensionality of the null subspace of the matrix. Accordingly, very small singular values also translate into very weak linear independence of the associated rows or columns of the matrix which is considered as *numerical rank deficiency*. The root of this amplification effect of small singular values can be readily seen from the presence of inverse singular values in the plain LS solution (Eq. 3.7). Components amplified by small singular values are nothing but corresponding right and left eigenvectors to those singular values which are numerically linearly dependent.

A Gaussian noise vector with a correlation matrix proportional to unity is a totally random vector with no correlation between its components, or a *white noise*. Such a noise vector may contain components corresponding to eigenvectors associated with small singular values that are responsible for instability. Because of the presence of these components, the effect of adding noise to the data $\vec{f}$ may severely affect the obtained solution $\vec{g}$. Besides noise, finite precision of numerical computations that results in a round-off error can yield a similar effect. Thus, in practice, solving a severely ill-posed problem even in the absence of noise by LS methods is merely impossible.

3.3 Variational Regularization

Generally, regularization is the process of approximating an ill-posed problem by a family of neighbouring well-posed ones. This approximation can be done either by varying the discretized kernel of the ill-posed problem to get a well-behaved kernel that defines a well-posed problem, or by confining the solution space to avoid mapping to noise components. As a result of this approximate nature of regularizations, there will always be an error associated with any regularization known as *regularization error*. Variational regularizations are those that rely on regularizing the ill-posed problem by modifying the kernel. Usually in regularization algorithms the adherence of the approximated problem to the original ill-posed problem is controlled by one or several parameters known as *regularization parameters*. The final pseudo-inverse solution to an ill-posed problem is constructed by choosing a regularization parameter or a set of parameters that gives the best compromise between the noise-filtering effect of the regularization and the regularization error. Because of the presence of the regularization error, most of the time in the form of systematic rather than random shifts in the results, confidence interval estimation is not feasible. However, it is possible to neglect the regularization error and define the confidence interval from the noise amplitude in the regularized solution.

3.3.1 Truncated Singular Value Decomposition

The simplest way of regularizing a linear inverse problem is by modifying the Moore-Penrose generalized inverse operator so that it can accommodate the numerical rank deficiency of the kernel. The origin of instability in the solution of a linear inverse ill-posed problem is the presence of a cluster of small singular values in the SVD of the kernel. In constructing the Moore-Penrose inverse operator of the kernel, we may consider these small singular values in addition to the null subspace represented by the singular values that are zero, thus generating a generalized inverse operator (a pseudo-inversion operator) that is likely to be well-behaved. This is equivalent to filtering the singular values of the kernel prior to constructing the generalized inverse operator. The filtering can be performed by imposing a step filter or simply by truncating the singular values smaller than some threshold value. This way of regularizing a linear ill-posed problems is known as *truncated singular value decomposition* (TSVD). The threshold value or the index of the smallest unfiltered singular value σ_{ii} plays the role of a discrete regularization parameter in the TSVD regularization.

The shortcoming of TSVD method is in its inflexibility in filtering the singular values that usually results in a big regularization error. This is particularly problematic when the ill-posedness of the problem is due to a continuum of gradually decaying singular values instead of a distinct cluster of small singular values, or, more technically, when the concept of numerical rank deficiency fails to describe the ill-posed behavior of the kernel, TSVD fails to give good results [42].

3.3.2 Tikhonov Regularization

Tikhonov regularization is a class of regularizations having a common structure. Because of its flexibility and effectiveness in treating a variety of linear inverse problems, Tikhonov regularization has been widely adopted and is the most widespread regularization technique in dealing with linear ill-posed inverse problems. It can be approached in two ways, either as the most general form of regularizations based on filtering singular values of the kernel or as an optimization problem.

The basic idea in any Tikhonov regularization is to minimize the following expression:

$$\Psi(\lambda) = \|\vec{f} - K\vec{g}\|^2 + \lambda\|L\vec{g}\|^2 \tag{3.11}$$

where L is a constraint matrix that imposes a desired property on the sought ideal solution, and λ is the regularization parameter. Minimizing $\Psi(\lambda)$ with respect to $\vec{g}$ results in the following pseudo-inverse solution for the problem that depends only on the regularization parameter λ [42]:

$$\vec{g}(\lambda) = (K^T K + \lambda L^T L)^{-1} K^T \vec{f} \tag{3.12}$$

In this way, the formidable task of finding the pseudo-inverse solution reduces to a minimization problem that depends only on one parameter, λ. Choosing a large λ biases $\vec{g}(\lambda)$ to satisfy the imposed expectation through L while solutions obtained from choosing a small λ retain compatibility with the data $\vec{f}$ by minimizing the mismatch norm $\|\vec{f} - K\vec{g}\|$. In a way analogous to the Moore-Penrose generalized inverse, a regularization operator $R(\lambda)$ is sometimes defined:

$$\vec{g}(\lambda) = R(\lambda)\vec{f}$$

where for Tikhonov regularizations this regularization operator can be identified explicitly in terms of L and K as [42]:

$$R(\lambda) = (K^T K + \lambda L^T L)^{-1} K^T. \tag{3.13}$$

It is not possible or easy to come up with a constraint matrix L that gives the best description of the ideal solution, for an arbitrary inverse problem. There exists a class of *smoothing* constraint matrices that can be applied in regularizing most of ill-posed problems irrespective of their specific details, especially those that originate in physical measurements. These smoothing matrices are discrete approximations of derivative operators and generally target the severe noise amplification of ill-posed problems by demanding a smooth regularized solution. Among these smoothing matrices, discretized version of the 0^{th} ($L_0 = I$) and 2^{nd} derivative operators are particularly important for their simple interpretation. The corresponding matrix to the 2^{nd} derivative operator (L_2) is closely related to the discretized curvature integral of a curve. Hence, choosing L_2 in Eq. 3.11 results in a regularized solution with the least

possible curvature. The L_2 constraint matrix can be represented as:

$$L_2 = \begin{pmatrix} 1 & -2 & 1 & & \\ & \ddots & \ddots & \ddots & \\ & & 1 & -2 & 1 \end{pmatrix}_{(n-2),n} \tag{3.14}$$

Imposing the L_0 matrix, which is known as the minimum norm constraint, is equivalent to imposing $F_\lambda(\sigma) = \frac{\sigma}{\sigma^2+\lambda^2}$ filter on the singular values (σ_{ii}) of the kernel [43]. The L_0 norm targets the severe noise amplification without making any further assumption about the properties of the ideal solution to the problem, so it can be applied in regularizing a broad range of linear ill-posed inverse problems. It should be noticed that when the solution is expected to be smooth with strong correlation between adjacent points, imposing the L_2 constraint gives better results compared to the L_0 constraint. Also, as can be expected from the analogy with the discretized curvature integral, imposing the L_2 constraint gives better results for finer-grid discretized solutions.

To gain a deeper insight into Tikhonov regularization and the origin of Tikhonov expression in Eq 3.11, suppose the amplitude of the noise superimposed on the data, $\|\vec{\sigma}_{\text{noise}}\|$, is known. Using Lagrange's method of undetermined multipliers, the ideal solution $\vec{g}$ can be determined through imposing constraint matrix L and finding a solution that minimizes the mismatch a constraint $\|\vec{f} - K\vec{g}\|^2 - \|\vec{\sigma}_{\text{noise}}\|^2 = 0$.

$$min\left\{(\|\vec{f} - K\vec{g}\|^2 - \|\vec{\sigma}_{\text{noise}}\|^2) + \lambda\|L\vec{g}\|^2\right\}_{\vec{g},\lambda} \tag{3.15}$$

The exact solution will then satisfy the following two equations:

$$\begin{aligned} \vec{g}(\lambda) &= (K^T K + \lambda L^T L)^{-1} K^T \vec{f} \\ \|\vec{f} - K\vec{g}(\lambda)\|^2 - \|\vec{\sigma}_{\text{noise}}\|^2 &= 0 \end{aligned} \tag{3.16}$$

In practice, the specific $\vec{\sigma}_{\text{noise}}$ may not available, but since it only enters into the determination of the Lagrange's multiplier, the regularization problem is reduced to finding a proper choice of the regularization parameter, for a given L. This observation not only explains why Tikhonov regularization is robust and flexible but also suggests a way to choose an optimal regularization parameter in Tikhonov regularizations, namely, through the use of the discrepancy principle.

3.4 Regularization Parameter Selection Methods

An essential part of any regularization algorithm is the selection of an optimal regularization parameter. Since finding the exact regularization parameter requires knowing the exact solution, an approximate value of the exact regularization parameter is sought through the investigation of the pseudo-inverse solution as a function of

regularization parameter. Consequently, the final regularized solution may contain regularization error due to choosing a regularization parameter slightly different from the exact one, in addition to the regularization errors associated with the presence of the noise.

3.4.1 Discrepancy Principle

Discrepancy principle is the most widely-used method of choosing regularization parameters based on the noise-level estimation. If an ill-posed problem is self-consistent in the sense that there exists an exact solution $\vec{g}_{\text{exact}}$, such that $K\vec{g}_{\text{exact}} = \vec{f}_{\text{exact}}$, then the optimal value of the regularization parameter would be the one that satisfies the following criterion:

$$\|\vec{f} - K\vec{g}(\lambda)\| = \delta_e \tag{3.17}$$

where δ_e is the estimated error in data $\vec{f}$ and should be less or at most equal to $\|\vec{\sigma}_{\text{noise}}\|$. For a discrete regularization parameter of the TSVD, the smallest index i should be chosen that satisfies $\|\vec{f} - K\vec{g}(i)\| \leq \delta_e$.

3.4.2 L-curve Criterion

L-curve is a powerful and convenient graphical tool not only in determining the optimal regularization parameter but also in analyzing the behavior of discrete ill-posed inverse problems. L-curve is the plot of the square of residual norm (*i.e.*, $\|\vec{f} - K\vec{g}(\lambda)\|^2$) versus the square of the imposed constraint norm[1] $\|L\vec{g}(\lambda)\|^2$ on the *log-log* scale for all allowed regularization parameters λ [42]. For regularizations with a continuous regularization parameter the L-curve is a continuous curve while for discrete regularizations such as TSVD the L-curve consists of a discrete set of points. The name arises because of a characteristic L-shape appearance typical of this plot, with a distinct corner separating vertical and horizontal regions of the curve (Fig. 3.1) [42].

Over-regularizing by choosing too large a value for the regularization parameter results in a small solution constraint norm but a large residual norm, and hence points at the far right region of the curve. On the other hand, poorly regularized solutions corresponding to choosing too small a value of the regularization parameter result in the noise components entering the solution, a case of a small residual norm and a large solution constraint norm. These un-regularized or poorly regularized solutions are located in the top left region of the L-curve, close to the vertical axis. The exact regularization parameter λ_{exact}, which by definition gives the best trade-off between the two solution and residual norms, is anticipated to be at the corner of the L-curve. Therefore, finding the optimal regularization parameter λ_{opt} as a good approximation to λ_{exact} reduces to a precise characterization of the corner in the L-curve [43].

[1]For TSVD or iterative regularizations, the solution norm or other measures may be used instead of the constraint norm.

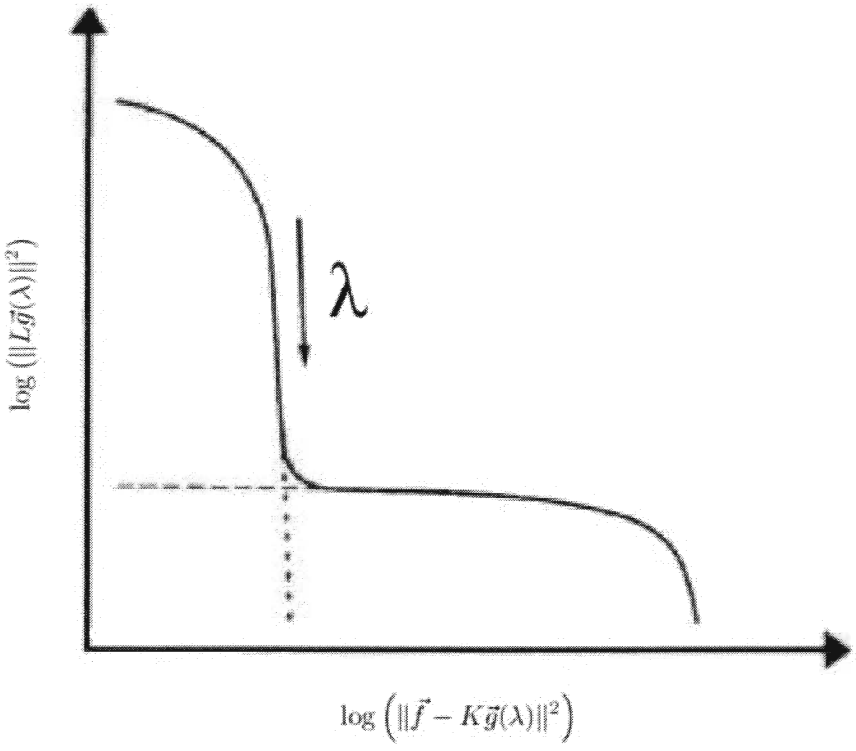

Figure 3.1: **L-curve**, poorly regularized solutions corresponding to choosing small λ have a big constraint norm and a small residual norm are located at the vertical part of the curve while over regularized solutions resulted from choosing big values for regularization parameter are located at the horizontal part of the curve.

To achieve this [44], the point of maximum curvature of the L-curve is taken to correspond to the optimal regularization parameter. If the coordinates of points on the L-curve, parameterized by λ, are given by $X(\lambda)$, $Y(\lambda)$, then:

$$X(\lambda) = \log(\|\vec{f} - K\vec{g}(\lambda)\|^2) \quad , \quad Y(\lambda) = \log(\|L\vec{g}(\lambda)\|^2) \tag{3.18}$$

and assuming that $X(\lambda)$, $Y(\lambda)$ vary smoothly with λ, the curvature function of the L-curve $\kappa(\lambda)$ is:

$$\kappa(\lambda) = \frac{X''(\lambda)Y'(\lambda) - Y''(\lambda)X'(\lambda)}{(X'(\lambda)^2 + Y'(\lambda)^2)^{\frac{1}{2}}} \tag{3.19}$$

where $(')$ denotes differentiation with respect to λ.

3.5 Iterative Regularizations

The goal in any regularization algorithm is to avoid the presence of amplified noise components in the pseudo-inverse solution. In non-iterative regularization techniques such as Tikhonov or TSVD this goal is pursued through kernel variation. Alternatively it is possible to use iterative methods, keeping the kernel intact while constraining possible solutions so as to avoid mapping the noise. However, both the mathematical formulation and the practical implementation of solutions based on the constrained solution space is not easy.

Iterative methods differ from non-iterative methods in several important way [42]:

- Iterative methods don't alter the kernel. Since the matrix-vector multiplication and the saxpy[2] operation (*i.e.*, $a \leftarrow a + b$) are the only operations in iterative methods, in regularizing ill-posed inverse problems by iteration there is no need for determining the SVD of the kernel.

- The main issues in iterative methods are the convergence and the rate of convergence. Iterative methods such as *Landweber method* in finite iteration are almost insensitive to the presence of noise in data.

- Since the generalized inverse of the kernel or the reciprocal of its singular values are not used into constructing the iterative solution, mapping the noise may take many iterations, particularly when the signal-to-noise ratio (SNR) is high[3].

- Iterative methods are the only methods of choice in problems where matrix representation of the kernel is not available and only the effects of the matrix-vector products (*i.e.*, $K\vec{g}$ and $K^{\dagger}\vec{g}$) are defined.

[2]Saxpy is a basic algebraic operation which is the combination of scalar multiplication and vector addition

[3]"The CG [conjugate gradient] method often produces iteration vectors in which the spectral components associated with the large eigenvalues tend to converge faster than the remaining components" [42, P.142]

3.5.1 Landweber Iteration Method

One of the regularization methods based on iteration is the *Landweber iteration*. It is a classical iteration method that was originally developed for finding the solution of large-scale well-posed problems but was found to have regularization effects as well. Landweber iteration method is based on transforming the "normal equation",

$$K^\dagger K\vec{g} = K^\dagger \vec{f}, \tag{3.20}$$

into its equivalent fixed point equation:

$$\vec{g}^{(k)} = \vec{g}^{(k-1)} + \omega K^\dagger(\vec{f} - K\vec{g}^{(k-1)}) \quad k = 1, 2, ... \tag{3.21}$$

where $g^{(0)}$ is the starting vector or the initial guess (usually taken to be zero) and ω is a real parameter satisfying $0 < \omega < 2\|K^\dagger K\|^{-1}$ to ensure non-expansivity of the fixed point operator $1 - K^\dagger K$, and hence, the convergence of the iteration [45],[42]. The iteration index, k, is the discrete regularization parameter in Landweber iteration method which its optimal value can be determined by regularization parameter selection methods such as the discrepancy principle or L-curve.

In the classical Landweber iteration (Eq. 3.21), the pseudo-inverse solution, $\vec{g}$, is subjected to no constraint. To improve the regularizing effect of the classical Landweber iteration method and make it a more flexible tool, desired properties of the pseudo-inverse solution may be imposed at each iteration as following [42]:

$$\vec{g}_{(k)} = \mathbf{P}\left(\vec{g}^{(k-1)} + \omega K^\dagger(\vec{f} - K\vec{g}^{(k-1)})\right) \tag{3.22}$$

where $\mathbf{P}$ is a projection operator that imposes the so-called "hard constraints".

The main disadvantage of the Landweber iteration method is its slow convergence rate that necessitates many iterations. To overcome this limitation, other faster iteration methods and in particular *conjugate gradient-based* methods can be applied in regularizing ill-posed inverse problems.

3.5.2 Conjugate Gradient Iteration Method

Currently there is a lots of interest in CG-based regularization methods mostly for their efficiency in dealing with large-scale problems. Like the Landweber iteration method, the conjugate gradient (CG) method was originally designed for solving large-scale linear equations with positive definite, symmetric matrices. These restrictions on the kernel in an arbitrary problem can be satisfied by transforming the linear equation,

$$\vec{f} = K\vec{g}, \tag{3.23}$$

to its corresponding normal equation of the problem:

$$K^\dagger \vec{f} = K^\dagger K\vec{g} \tag{3.24}$$

Denoting the CG error at each iteration step by:

$$\eta(\vec{g}^{(k)}) = (\vec{g}_{LS} - \vec{g}^{(k)})^{\dagger} K^{\dagger} K (\vec{g}_{LS} - \vec{g}^{(k)}) \tag{3.25}$$

where $\vec{g}_{LS}$ is the sought least square solution to the problem, then the CG iterate $\vec{g}^{(k)}$ can be written as [42, 46]:

$$\vec{g}^{(k)} = \vec{g}^{(0)} + \sum_{i=1}^{k-1} \frac{\eta(\vec{g}^{(i)}) - \eta(\vec{g}^{(k)})}{\|K^{\dagger}(\vec{f} - \vec{g}^{(i)})\|^2} K^{\dagger}(\vec{f} - \vec{g}^{(i)}) \tag{3.26}$$

An important property of the iterates $\vec{g}^{(k)}$ in the CG method is the orthogonality of corresponding residual vectors,

$$r^{(k)} = K^{\dagger}\vec{f} - K^{\dagger}K\vec{g}^{(i)}, \tag{3.27}$$

which with zero starting vector, $\vec{g}^{(0)} = 0$, results in the monotonic growth of the solution norm $\|\vec{g}^{(k)}\|$ with k. This, along with the monotonic behavior of the residual norm $\|\vec{f} - K\vec{g}\|$, is a crucial criterion that ensures the reliability of the L-curve method in finding the optimal truncation index, k_{t} [42].

There exist several mathematically equivalent implantation of the CG algorithm which are merely five simple statements for each iteration. However, it has been experimentally determined that one of them that usually referred to as CGLS (or in some literature CGNE) is the most stable one. The CGLS implementation of the CG method can be stated as [42]:

$$\begin{aligned}
\alpha_k &= \|K^{\dagger}\vec{r}^{(k-1)}\|^2 / \|K\vec{d}^{(k-1)}\|^2 \\
\vec{g}^{(k)} &= \vec{g}^{(k-1)} + \alpha_k \vec{d}^{(k-1)} \\
\vec{r}^{(k)} &= \vec{r}^{(k-1)} - \alpha_k K\vec{d}^{(k-1)} \\
\beta_{(k)} &= \|K\vec{r}^{(k-1)}\|^2 / \|K\vec{r}^{(k-1)}\|^2 \\
\vec{d}^{(k)} &= K^{\dagger}\vec{r}^{(k)} + \beta_{(k)}\vec{d}^{(k-1)}
\end{aligned} \tag{3.28}$$

where $\vec{r}^{(k)}$ is the residual vector and $\vec{d}^{(k)}$ is an auxiliary n-vector (n is the dimensionality of $K^{\dagger}K$). The CGLS algorithm is initialized with the starting vector $\vec{g}^{(0)}$ which results in following initial values for $\vec{r}^{(0)}$ and $\vec{d}^{(0)}$:

$$\vec{r}^{(0)} = \vec{f} - K\vec{g}^{(0)} \quad , \quad \vec{d}^{(0)} = K^{\dagger}\vec{r}^{(0)} \tag{3.29}$$

3.6 Successful Pseudo-Inversion

Successful pseudo-inversion in ill-posed inverse problems critically depends on applying the appropriate regularization method to the inversion process. The ill-posedness of different ill-posed inverse problems are usually different in nature and severity, and the fact that regularization algorithms inherently are not definite tools, which necessitates knowing the behavior of the problem in hand to be able to determine the effective regularization method.

To achieve an effective extraction of the anisotropy distribution and relaxation parameters from partially-relaxed powder spectra, it is necessary to first investigate the mathematical structure of the involved convolution integrals in more details. Particularly, properties such as non-linearity, the size of the problem, the behaviour of the discretized kernel are of prime importance in devising the effective pseudo-inversion procedure.

Chapter 4

Extracting the Relaxation Rates

Extracting relaxation rates from partially-relaxed powder spectra is an extension and generalization of conventional de-Pakeing. In practice, due to the so-called "dead time" of the receiver which is an instrumental limitation in NMR experiments, FID observation starts later than $\tau = 0$, typically offer a delay of about several microseconds. Echo sequences do allow one to bypass this limitation [4], but may result in some tiny distortions due mainly to the orientation-dependent transverse relaxation. Thus, experimentally obtained spectra might not represent the ideal spectra at $\tau = 0$. Extracting the anisotropy distribution from such partially-relaxed powder spectra using conventional de-Pakeing, may result in systematic errors. Being able to de-Pake a set of several partially-relaxed powder NMR spectra simultaneously while accounting for relaxation, not only offers access to the valuable information contained in the spectral densities, but also results in much better estimates for anisotropy and orientation distributions.

4.1 De-Pake

As was mentioned in the Introduction, deuterium NMR powder spectra are the convolution of the orientation and anisotropy distributions,

$$f(\omega) = \int g(\nu) \left[p(\beta) \frac{\partial \beta}{\partial \omega} \right] d\nu, \tag{4.1}$$

where $\omega = \nu P_2(\cos\beta)$. Linearity with respect to the anisotropy distribution is the key feature of the above convolution integral that allows for applying pseudo-inversion algorithms to de-Pake the powder spectra.

In practice, since the assumption of a random powder distribution of domain orientations may not strictly hold, the orientation distribution has to be determined at the same time. Unlike the anisotropy distribution, the determination of the orientation distribution in practice is done by choosing from a class of physically reasonable distributions. In the case of vesicular model membranes, considering the elongation of a vesicle under the effect of the strong magnetic field of the spectrometer, the following general forms can be expected for the orientation distribution of the vesicle [9]:

$$p_E(\beta) \propto \frac{\sin(\beta)}{[1 - (1 - \kappa)\cos^2(\beta)]^2} \tag{4.2}$$

in which κ is a parameter that describes the elongation of the vesicle and uniquely characterizes any distribution of this form. This class of distributions, known as the *ellipsoidal model* is based on the assumption that there is a strong correlation between adjacent domains; this tends to neglect thermal fluctuations [47]. On the other hand, assuming a weak correlation between the orientation of adjacent domains leads to the *Boltzmann model* with the following generic form:

$$p_B(\beta) \propto \sin(\beta) \exp[\kappa \cos^2(\beta)] \tag{4.3}$$

Here κ is inversely proportional to the temperature and $\cos^2(\beta)$ indicates the orientation-dependence of interaction energy between the membrane domains and the magnetic field. $\kappa = 0$, which corresponds to high temperatures, results in totally random distribution of domains while, on the other hand, $|\kappa| \gg 1$ gives rise to perfect order [47]. Other physically reasonable models can be considered. An essential feature of all such models should be their ability to vary significantly the shape of the distribution as a function of κ.

Eq. 4.1 is bilinear in the two anisotropy and orientation distributions. Its discretized version can be rewritten explicitly in the two discretized distributions as:

$$f^i = \mathcal{K}^i_{j,k} p_j g_k \tag{4.4}$$

where $\mathcal{K}$ is independent of the two distributions and is related to the scaling relation of the de-Pake problem, *i.e.*, the $P_2(\cos\beta)$ scaling relation. For linearly-independent orientational distributions, it is likely that the true distribution defines a consistent kernel (physically and mathematically) with the powder spectrum $\vec{f}$. The effect of choosing an orientation distribution p^{trial} other than the true one p^{true} adds a component g^{error} to the true anisotropy distribution g^{true}, given by the following equation:

$$\mathcal{K}^i_{j,k}(p^{\text{true}}_j - p^{\text{trial}}_j) g^{\text{true}}_k = \mathcal{K}^i_{j,k} p^{\text{trial}}_j g^{\text{error}}_k$$

Most of the time this component leads to non-physical features in the extracted anisotropy distribution $g^{\text{true}} + g^{\text{error}}$ such as negativity which is the indication of inconsistency between the chosen model based on choosing p^{trial} for the orientation distribution and the spectrum. Therefore, the best estimate for the anisotropy distribution, $g(\nu)$, and orientational distribution parameter, κ, from a class of orientation distributions can be found simultaneously, by examining all orientational distribution choices and selecting the one that gives the best match and the most physically plausible result [9].

4.2 Partially Relaxed Powder Spectra

Partially-relaxed powder spectra can be described by modifying the convolution integral of Eq. 4.1 as follows:

$$f(\omega,\tau)=\sum_i \int g^{(i)}(\nu)\left[p(\beta)\frac{\partial\beta}{\partial\omega}\right] e^{-\frac{\tau}{T^{(i)}(\beta)}}\, d\nu \tag{4.5}$$

where $g^{(i)}(\nu)$ is the contribution of the ith molecular site (the ith doublet in the case of ^{2}H NMR) to the anisotropy distribution $g(\nu)$:

$$g(\nu)=\sum_i g^{(i)}(\nu) \tag{4.6}$$

and $\frac{1}{T^{(i)}(\beta)}$ is the relaxation rate associated with it, a domain at an angle β from the $\hat{z}$ axis of the lab frame. The relaxation rate $\frac{1}{T^{(i)}(\beta)}$ is related to the three relaxation parameters which can be either $J^{(i)}_{0,0}(0)$, $J^{(i)}_{1,1}(\omega_0)$, and $J^{(i)}_{2,2}(2\omega_0)$ or $C^{(i)}_0$, $C^{(i)}_2$, and $C^{(i)}_4$ as coefficients of respectively Eq. 2.44 or Eq. 2.46 for ith carbon position, depending on the parameterization chosen.

Multiple doublets, with their own orientation-dependent relaxation rates, scaled through the $P_2(\cos\beta)$ by the powder superposition of domains, which itself may have been partially skewed by the alignment in the magnetic field all provide overlapping contributions to Eq. 4.5, making the inverse problem intractable. Still, although non-linear exponential dependence on the orientation-dependent relaxation rates hinders the calculations, it does not make it impossible to deal with. In the case of a single labeled site where for ^{2}H NMR the anisotropy distribution contains only one doublet, the problem can be solved like a conventional de-Pake problem but with three additional relaxation parameters.

If the unrelaxed spectrum at $\tau = 0$ were available, it would become possible to determine $g^{(i)}(\nu)$ distributions and thus potentially to solve the inverse problem either by searching the relaxation parameter space by the brute force or through methods such as descending gradient. However, in practice the spectrum at $\tau = 0$ is not experimentally accessible. Typically the transverse relaxation rate in lipids is of the order of tens of microseconds which does result in systematic distortions in the spectra.

4.2.1 Linearization

Progress can be made if the problem is linearized. This is usually done by approximating the non-linear equation in the neighborhood of a point by its derivative at that point. In the case of extracting the anisotropy distribution and the relaxation parameters from partially relaxed spectra the exponential dependence on relaxation parameters suggests solution through linearization around $\tau = 0$. The derivative of Eq. 4.5 with respect to τ at $\tau = 0$ is:

$$\left.\frac{df(\omega,\tau)}{d\tau}\right|_{\tau=0}=\sum_i \int -\frac{1}{T^{(i)}(\beta)}\, g^{(i)}(\nu)\left[p(\beta)\frac{\partial\beta}{\partial\omega}\right] d\nu \tag{4.7}$$

which is linear in both $g^{(i)}(\nu)$ distributions and in the relaxation parameters. The bilinear form of the above equation in unknown quantities still poses the same difficulties as the original problem (Eq. 4.5). However, it might be possible to use the spectrum at the smallest accessible τ to find approximate $g^{(i)}(\nu)$ distributions, and then from that, and from Eq. 4.7, the relaxation parameters. Solving the problem in this way not only is very sensitive to the presence of noise in the the spectrum corresponding to the shortest τ value, but also it does not use the information contained in the partially-relaxed spectra at τ values comparable to the relaxation time T. One way to make a better use of the available data is to observe the spectra at several short τ values where linear approximation to the exponentials is still valid. A more robust and general form of numerical derivation can be implemented through polynomial interpolation. In fact, the most accurate way of performing numerical calculations such as calculation of derivatives and integration in numerical analysis is based on polynomial interpolation [48]. In this way not only all the information contained in the available partially-relaxed spectra is used, even at τ values where linear approximation to the exponential fails, but also the true spectrum at $\tau = 0$ can be obtained by extrapolation.

4.2.2 Vandermonde and Newton Interpolations

Vandermonde interpolation is one of several numerical interpolation methods of finding a polynomial that goes exactly through a set of given data points. Obviously the number of parameters in determining the polynomial should not exceed the number of data points to ensure the uniqueness of the polynomial. Given a set of points $(\tau_l, f(\tau_l))$ for $l = 0, \ldots, (n-1)$, Vandermonde interpolation, maps this set of n points to a set of n coefficients of monomials,

$$P(\tau) = \sum_{l=0}^{n-1} a_l \frac{\tau^l}{l!} \tag{4.8}$$

where a_l are the interpolation coefficients and $P(\tau)$ is the polynomial replacing the data.

This interpolated polynomial is expected to regenerate data the points at any given τ_l. From this criterion and from the fact that the polynomial is a linear combination of unknown interpolation coefficients, the Vandermonde transformation matrix that maps the data points to the polynomial coefficients can be explicitly written as:

$$\begin{pmatrix} f(\tau_0) \\ f(\tau_1) \\ \vdots \\ f(\tau_{n-1}) \end{pmatrix} = \begin{pmatrix} 1 & \tau_0 & \ldots & \tau_0^{n-1} \\ 1 & \tau_1 & \ldots & \tau_1^{n-1} \\ \vdots & \vdots & \ddots & \vdots \\ 1 & \tau_{n-1} & \ldots & \tau_{n-1}^{n-1} \end{pmatrix}_{n,n} \begin{pmatrix} a_0 \\ a_1 \\ \vdots \\ a_{n-1} \end{pmatrix} \tag{4.9}$$

This transformation matrix is in principle invertible, but it has a high condi-

tion number that rapidly grows with the size of the matrix, n. Thus, it is severely ill-conditioned. As the matrix dimensionality increases the last columns rapidly become numerically dependent, especially when the entries in these columns exceed the precision of the machine, where the round-off errors occur and they become exactly dependent. Such high powers of τ should be avoided.

There exist other interpolations which map data points to coefficients of Newton polynomials instead of monomials as in the Vandermonde interpolation. For a set of points $(\tau_l, f(\tau_l))$ with $l = 0, \ldots, (n-1)$ Newton polynomials are defined as:

$$\begin{aligned} n_1(\tau) &= 1 \\ n_j(\tau) &= \prod_{k=0}^{j-1}(\tau - \tau_k) \qquad j = 2, \ldots, (n-1) \end{aligned} \tag{4.10}$$

The most famous and widely adopted of interpolations based on the above Newton polynomials is *Newton's interpolation* which has an upper triangular transformation matrix:

$$\begin{pmatrix} n_1(\tau_0) & 0 & \ldots & 0 \\ n_1(\tau_1) & n_2(\tau_1) & & \\ \vdots & \vdots & \ddots & \\ n_1(\tau_{n-1}) & n_2(\tau_{n-1}) & \ldots & n_{n-1}(\tau_{n-1}) \end{pmatrix}_{n,n} \tag{4.11}$$

This form significantly simplifies numerical calculations, particularly in large-scale problems. The Vandermonde and Newton interpolations are in essence the same and are related by a unitary transformation of the change of basis from the Newton polynomials to monomials. However, in practice Newton's interpolation is less ill-posed than the Vandermonde interpolation [48].

4.2.3 Linearizing the Problem by the Vandermonde Interpolation

Interpolating Eq. 4.5 with respect to τ by the Vandermonde interpolation gives:

$$f(\omega, \tau) = \sum_{l=0}^{n-1} a_l(\omega)\frac{\tau^l}{l!} \tag{4.12}$$

with coefficients $a_l(\omega)$:

$$a_l(\omega) = \sum_i \int (-\frac{1}{T^{(i)}(\beta)})^l g^{(i)}(\nu) \left[p(\beta)\frac{\partial\beta}{\partial\omega}\right] d\nu. \tag{4.13}$$

Through this interpolation, partially-relaxed spectra are transformed into new distributions $a_l(\omega)$. Two of these $a_l(\omega)$ coefficients are particularly important: $l = 0$

and $l = 1$ which are linear in both anisotropy and orientation-dependent relaxation rates:

$$a_0(\omega) \equiv f(\omega, 0) = \int g(\nu) \left[p(\beta) \frac{\partial \beta}{\partial \omega} \right] d\nu$$

$$a_1(\omega) = \sum_i \int (-\frac{1}{T^{(i)}(\beta)}) g^{(i)}(\nu) \left[p(\beta) \frac{\partial \beta}{\partial \omega} \right] d\nu \tag{4.14}$$

The distribution that corresponds to $l = 0$ is the extrapolated spectrum at $\tau = 0$ which in turn can be used to determine κ (the orientation distribution parameter) and the anisotropy distribution $g(\nu)$; and then $g^{(i)}(\nu)$ distributions can be determined by separating the peaks. With the help of $g^{(i)}(\nu)$ and the orientation distribution $p(\beta)$, a straightforward numerical deconvolution leads to the extraction of relaxation parameters from the distribution of the second coefficients $a_1(\omega)$.

It is possible to use the Newton interpolation instead of the Vandermonde interpolation and at the end translate everything back by the unitary transformation that transform Newton interpolation matrix to Vandermonde matrix or, alternatively, by directly calculating $a_0(\omega)$ and $a_1(\omega)$ from the Newton interpolation polynomials, $n_j(\tau)$, and their coefficients, $c_j(\omega)$, as follows:

$$a_0(\omega) = \sum_{j=0}^{n} c_j(\omega) n_j(0)$$

$$a_1(\omega) = \sum_{l=0}^{n} c_j(\omega) \frac{d}{d\tau} n_j(\tau)|_{\tau=0} \tag{4.15}$$

However, the general outline of the calculational strategy remains the same.

4.2.4 Limitations

Normally obtaining an NMR spectrum requires repeating a numbers of scans to achieve an acceptable signal-to-noise ratio which, depending on the concentration of nuclei of interest in the sample, may take a long time. This limits the number of partially-relaxed spectra that can be observed. On the other hand, linearizing Eq. 4.5 replaces the first two coefficients in the exact expansion of exponential decays with the first two coefficients of the polynomial obtained from the interpolation. The accuracy of this approximation depends on two factors: the number of points in τ (the number of observed spectra), and the longest observed τ. These two factors can be combined in a single criterion as:

$$(\frac{\tau}{T_{\min}})^n / n! \ll 1 \tag{4.16}$$

where n is the number of observed spectra and $\frac{1}{T_{\min}}$ is the relaxation rate of the fastest relaxation. Eq. 4.16 represents a mathematical prescription of what constitutes a set of exponential data that can be successfully analyzed through inversion.

4.2.5 Regularizing the Extraction of Relaxation Parameters

In the presence of noise, the procedure outlined above requires three regularizations. First and the most crucial of all is regularizing the interpolation. Interpolating the data either by Vandermonde or Newton interpolation is very vulnerable to noise and can yield a significant regularization error. The other two regularizations are associated with the determination of the anisotropy and orientation distributions from the extrapolated spectrum at $\tau = 0$ and the extraction of relaxation parameters from $a_1(\omega)$, which both depend on the result of the interpolation. In fact, the greatest challenge in regularizing this extraction problem arises from the application of successive regularizations. The extracted regularization parameter at the end is critically dependent on the effectiveness of the previous two regularizations.

Although Newton's interpolation matrix is numerically less ill-posed than the Vandermonde matrix, using Vandermonde interpolation allows for imposing a simple constraint on the solution which can be very advantageous in the regularization. As seen in Eq. 4.13, the coefficients of the monomials interpolating a combination of exponentially decaying functions are expected to be alternatively positive and negative. It is likely the reason why using direct, variational regularization methods such as TSVD and Tikhonov regularizations for noise levels higher than 0.1% results in either a poorly regularized interpolation that translates into huge uncertainty in extracted relaxation parameters, or introduces a big regularization error that again biases the final result (results not shown). Of course imposing the appropriate sign on the solution of the interpolation, in principle, is expected to result in very accurate results, but implementing such algorithms requires a direct search of the constrained solution space which is not feasible for problems of non-trivial sign.

The failure of variational regularization methods in properly regularizing the interpolation necessitates using iterative methods. As described in the previous chapter, iterative methods are essentially independent of the SVD of the kernel. At the same time, the Vandermonde and Newton interpolation matrices are equivalent to within a unitary transformation, and so there is no difference between them in implementing an iterative algorithm. The Landweber iteration method allows for imposing hard constraints, but because iterative regularizations are fundamentally path-dependent methods in the solution space, imposing the appropriate sign of the expected solution as a hard constraint in this problem may prevent the convergence of the iteration. Among all of the regularization methods mentioned in the previous chapter, CG was found to be the best way of regularizing the interpolation. The only problem with the CG method is that since it has a very fast convergence rate, effective regularization requires a proper choice of the truncation index. Despite the fact that the L-curve criterion is not very successful in determining the optimal regularization parameter

in regularizations with discrete regularization parameter, but it still can be used to approximate the optimal truncation index in the CG method.

To determine the anisotropy distribution and the $g^{(i)}(\nu)$ distributions from $a_0(\omega)$ (the extrapolated powder spectrum at $\tau = 0$), conventional de-Pake can be applied. Typically, doublets corresponding to carbon positions close to the end of the hydrocarbon chains of lipids are well resolved and separate. While those corresponding to carbon positions in the upper half of the chain are tend to overlap. As described at the end of Chapter 2, the carbon positions on the upper half of the hydrocarbon chains of lipids constitute the plateau region in both the segmental order and relaxation profiles. Since the relaxation rates are almost the same within the plateau, all unresolved doublets can be treated as a single position, of appropriately higher spectral intensity. A series of paired Gaussian peaks can then be used to fit to the anisotropy distribution. The Gauss-Newton method is the most widely used numerical tool in fitting and non-linear least squares problems [49]. The advantage of using this method is that it allows one to impose constraints such as constant area of the peaks or equal widths, and to make some assumptions about the positions of the peaks [4, 24].

The final step is the determination of relaxation parameters from the distribution of the second coefficients of the interpolated partially-relaxed spectra, $a_1(\omega)$. Since this determination is a very delicate problem and does not tolerate the regularization error arising in Tikhonov regularizations, iterative methods should be applied instead. Unlike the interpolation, extracting regularization parameters can be performed by the Landweber method that allows for imposing non-negativity constraint in each iteration. Low convergence rate of the Landweber iteration method reduces the sensitivity of the obtained regularized solution to the choice of the truncation index. To determine the truncation index in this regularization, the discrepancy principle can be used.

4.3 Summery of the Numerical Strategies

To summarize, the following numerical approach has been devised as a suitable numerical strategy of inverting a series of partially-relaxed NMR spectra as defined by Eq. 4.5 (Table. 4.1). The implementation of this extraction procedure was done in "SCILAB" [50] environment which is a vector based programming language suitable for this type of numerical calculations [9].

DePaking:

$$f(\omega) = \int g(\nu) \left[p(\beta)\frac{\partial\beta}{\partial\omega}\right] d\nu$$

$\downarrow$

Include relaxation:

$$f(\omega,\tau) = \int g(\nu) e^{-\tau/T(\beta,\nu)} \left[p(\beta)\frac{\partial\beta}{\partial\omega}\right] d\nu$$

$\downarrow$

For a multi-site linearized superposition:

$$g(\nu) = \sum_i g^{(i)}(\nu)$$
$$e^{-\tau/T(\beta,\nu)} = \sum_i \sum_l \left(\frac{1}{T^{(i)}(\beta)}\right)^l \frac{\tau^l}{l!}$$

$\downarrow$

Input, 2D data:

$$f(\omega,\tau) = \sum_i \int g^{(i)}(\nu) e^{-\tau/T^{(i)}(\beta)} \left[p(\beta)\frac{\partial\beta}{\partial\omega}\right] d\nu$$

$\downarrow$

Polynomial approximation in τ:

$$a_l(\omega) = \sum_i \int g^{(i)}(\nu) \left(\frac{1}{T^{(i)}(\beta)}\right)^l \left[p(\beta)\frac{\partial\beta}{\partial\omega}\right] d\nu$$

$\downarrow$

Extracting $g(\nu)$ from $a_0(\omega)$:

$\downarrow$

Finding $g^{(i)}(\nu)$ from $g(\nu)$:

$\downarrow$

Extracting relaxation parameters from $a_1(\omega)$:

$$C_0^i, \quad C_2^i, \quad C_4^i$$

Table 4.1: **The summery of the extraction procedure**

Chapter 5

Numerical Experiments

To test the numerical inversion procedure outlined in the previous chapter, two simulated partially-relaxed spectral data sets were developed and tested, under a variety of random noise condition. Both sets were based on the experimentally measured ^{2}H NMR relaxation parameters for perdeuterated hexamethylbenzene [4, 51] and for chain deuterated 1-palmitoyl-2-oleoyl-sn-glycero-3-phosphocholine (POPC) lipid [24].

In each case, experimentally-determined anisotropy distributions, a single splitting in the case of HMB, and a set of 15 splittings forming a typical bilayer order-parameters profile for POPC, were used to generate the $\tau = 0$ powder spectrum. The experimentally measured relaxation rates and their parameters C_0, C_2, and C_4 [24] were then used to generate a series of 16-32 partially-relaxed spectra, to form a 2D NMR data set. Random Gaussian noise was added, with 0.1%-10% relative amplitude to the powder spectrum, and the resulting data sets were subjected to the inversion process as outlined above. In general, inversion results are in excellent agreement with inputs used to generate the data sets. To help analyze the performance of the numerical procedure, the results in the following sections are presented in terms of the difference between the "true" inputs and the "calculated" results of the inversion.

5.0.1 Hexamethylbenzene results

HMB is a ring-shape molecule with 6 CH_3 groups (Fig. 5.2) whose ^{2}H NMR spectrum has characteristics similar to a single-site-labeled lipid sample. The anisotropy distribution of HMB, is a doublet separated by $33.7\,kHz$ corresponding to $S_{CD} \approx 0.1$ [4]. The relaxation parameters reported in [4] in terms of the coefficients of the Legendre functions (Table 5.1) have been obtained from measuring the relaxation rate at three regions of the powder spectra: the centre, shoulder and the edge which are correspond to $\beta = 54.74°$, $\beta = 90°$, and $\beta = 0°$ respectively. The orientation dependence of the

c_0	c_2	c_4
18.9	14.9	−0.56

Table 5.1: **HMB relaxation parameters** (all values in s^{-1})

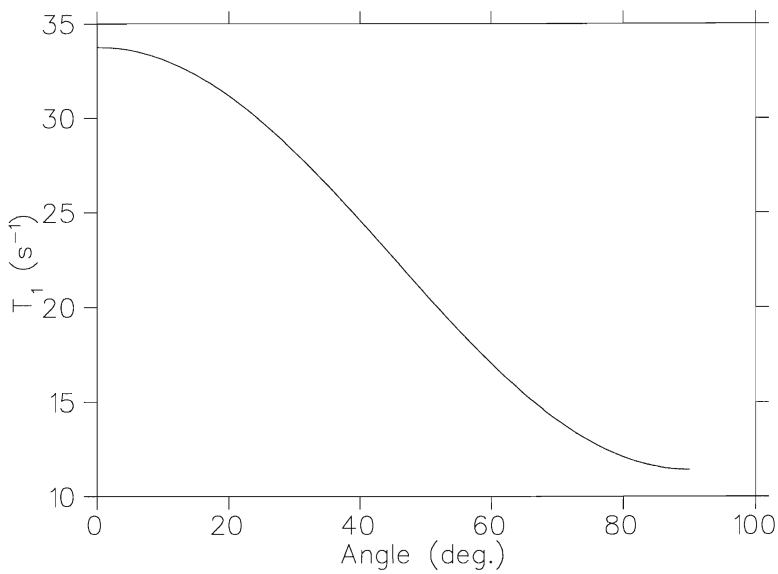

Figure 5.1: **Orientation dependence of HMB relaxation rates**, β is the angle between the c_6 axis of symmetry of the HMB molecule and the magnetic field of the spectrometer (Fig. 5.2).

longitudinal relaxation rate for HMB based on the reported relaxation parameters is given in Fig. 5.1. A set of HMB powder spectra was simulated for $\tau = 0$ to $\tau = 1s$ as shown in Fig. 5.3. From this simulation, 16 spectra corresponding to equispaced τ values starting at $\tau =$ 5ms, 5ms apart, were used as data to extract the three relaxation parameters. Six noise levels were examined by adding a random vector with vanishing mean and 0.1%, 0.2%, 0.5%, 1%, 5%, and 10% relative amplitudes to the data. To determine the confidence intervals for each noise level, the extraction process was repeated 100 times using different random noise vectors, and the resulting averages and their standard deviations reported as shown in Fig. 5.4 and Table 5.2.

5.0.2 1-palmitoyl-2-oleoyl-sn-glycero-3-phosphocholine (POPC) results

Unlike HMB, direct measurement of the relaxation parameters for POPC were not available in the literature. For testing purposes, a relation based on the motional model of HMB in [4] was again used to generate the relaxation parameters from the available relaxation rates. There are experimentally measured relaxation rates at two

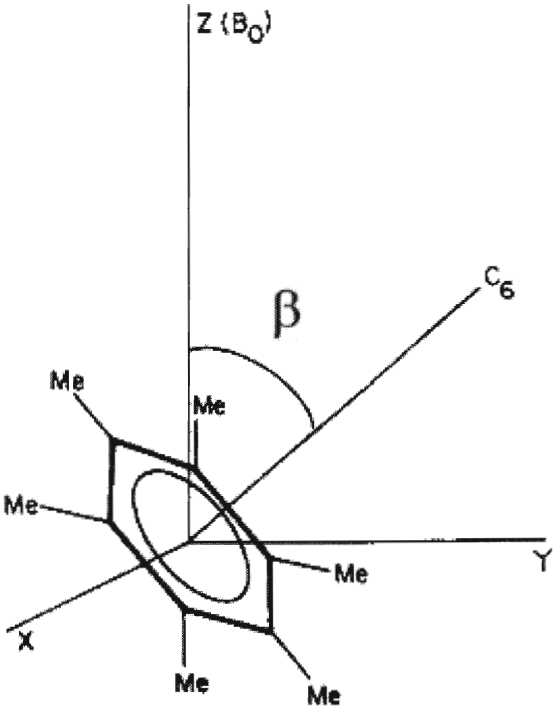

Figure 5.2: **HMB Orientation**, Me indicates the position of the six methyl groups. Reproduced from [52].

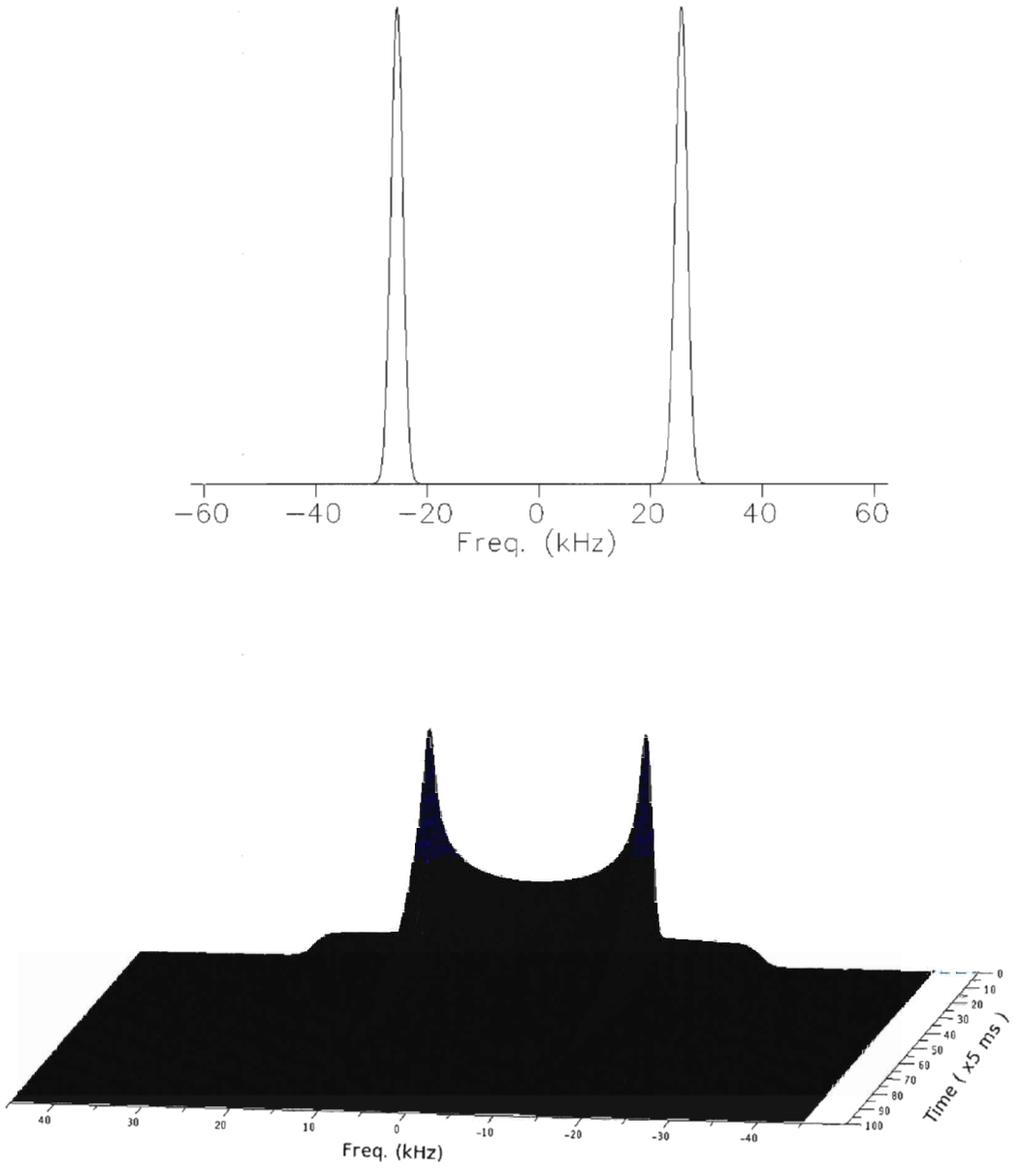

Figure 5.3: **Simulated HMB powder spectrum relaxation**, the above anisotropy distribution along with relaxation parameters of Table 5.1 were used to simulate the relaxation.

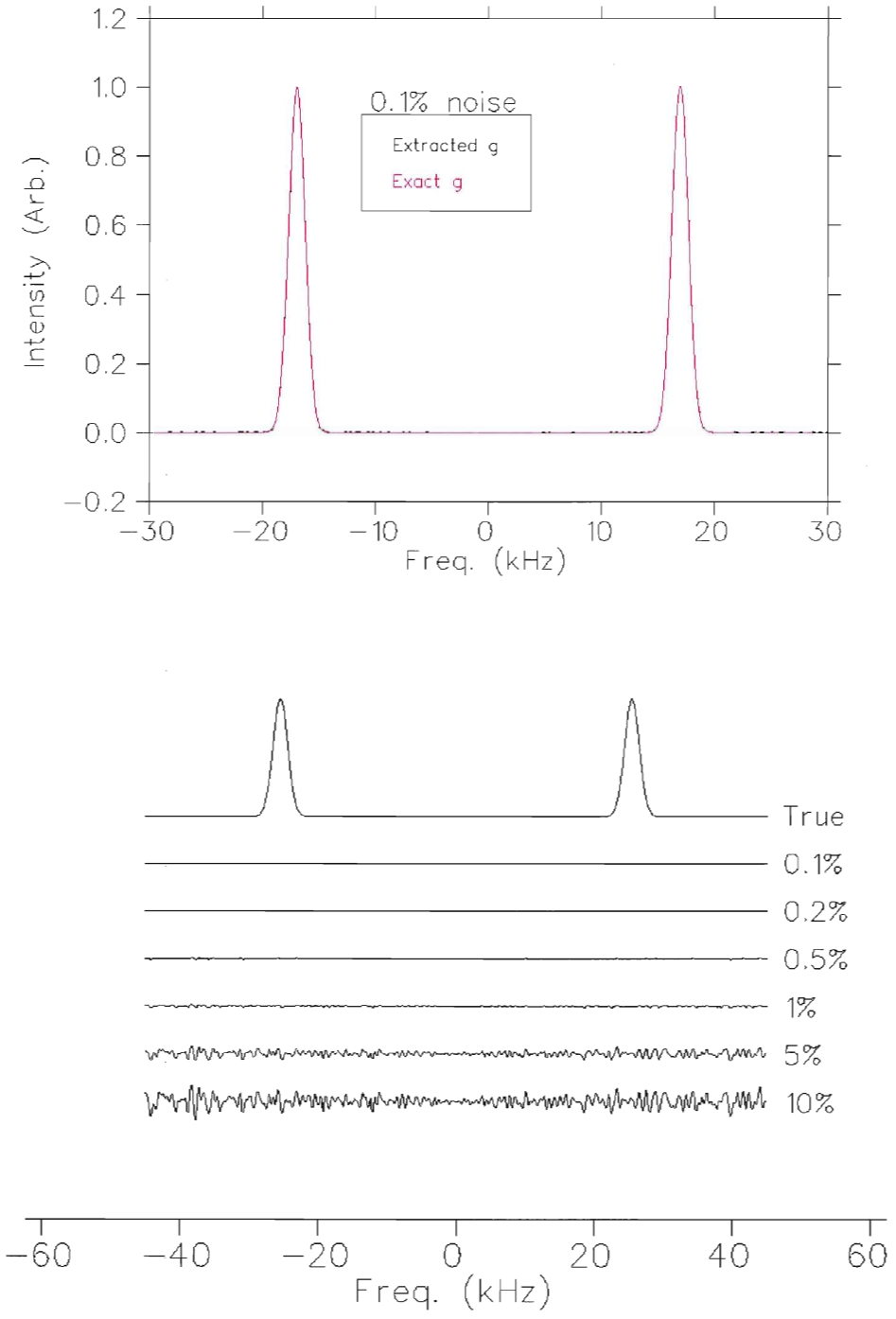

Figure 5.4: **Extracted anisotropy distribution for HMB data set** in the presence of 0.1%, 0.2%, 0.5%, 1%, 5%, and 10% noise. The top figure represents the exact and extracted anisotropy distributions in the presence of 0.1% noise and the bottom figure represents the exact anisotropy distribution with the mismatches between the extracted distributions for different noise levels and the exact one.

	c_0	c_2	c_4
Exact	18.9	14.9	−0.56
Extracted from 0.1%	18.8 ± 0.005	14.7 ± 0.02	-0.64 ± 0.02
Extracted from 0.2%	18.8 ± 0.01	14.7 ± 0.04	-0.64 ± 0.04
Extracted from 0.5%	18.8 ± 0.03	14.7 ± 0.1	-0.62 ± 0.09
Extracted from 1%	18.8 ± 0.056	14.7 ± 0.22	-0.59 ± 0.19
Extracted from 5%	18.78 ± 0.27	14.29 ± 1.08	-0.53 ± 0.68
Extracted from 10%	18.75 ± 0.55	13.16 ± 1.96	-0.48 ± 0.98

Table 5.2: **Extracted relaxation parameters from data in the presence of** 0.1%, 0.2% 0.1%, 0.5%, 1%, 5%, 10% **noise with their standard deviations** (all values in s^{-1}).

orientations (typically 0° and 90°), from experiments with oriented bilayers, but the determination of three relaxation parameters, whether in terms of the coefficients of Legendre polynomials or the spectral densities themselves at $\beta = 0$, requires the knowledge of relaxation rates at least at three distinct orientations. The relaxation profiles reported in [24] along with the following model were used to generate realistic relaxation parameters and to test inversion algorithm:

$$\frac{1}{T_1}(\beta) = 34\xi^2 \left(1 + 0.79P_2(\cos\beta) - 0.03P_4(\cos\beta)\right) \tag{5.1}$$

where $34\xi^2 = \frac{1}{T_1}$ [4, p.93]. No claim that this is, indeed, the relaxation behaviour in POPC is being made. However, a successful inversion to obtain back the relaxation behaviour of Eq. 5.1 would be a reassurance that the method used would report the true dependence when applied to the appropriate experimental data.

The re-calculated profiles of relaxation parameters are shown in Fig. 5.5. A closer look reveals that this relaxation profile does not manifest the plateau region, contrary to what was discussed at the end of Chapter 2. These relaxation quantities have been obtained from a fully deuterated, oriented bilayer where, due to the congestion of resonance peaks, the relaxation rates of each carbon position are not separable. It has been assumed in [24] that the profile of relaxation rates and the segmental order profile are linear in carbon position. Also it should be noted since, the relaxation rate of the last carbon position has been measured originally in [24], an extrapolated the relaxation profile of the second half of the chain was used. This extrapolated relaxation rate for the terminal CH_3 group may not be valid. The simulation of the POPC powder spectrum relaxation for $\tau = 0$ to 200 ms is shown in Fig. 5.5.

The results for extracted anisotropy distributions (the mismatches), are shown in Fig 5.6. 16 spectra corresponding to τ values from 1ms to 16ms were used to extract the relaxation rates for 0.1%, 0.2%, and 0.5% noise levels, and for each noise level 100

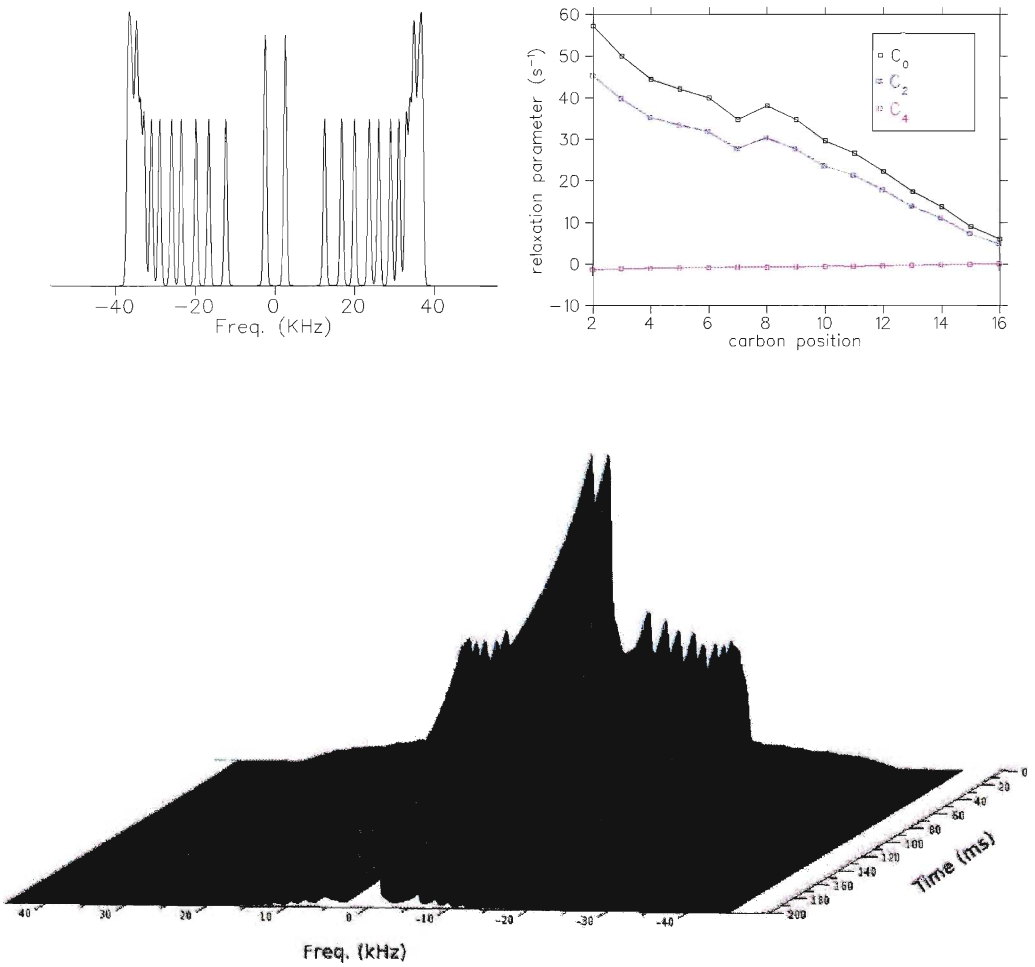

Figure 5.5: **Relaxation of the POPC powder spectrum**, the anisotropy distribution (the top left figure) along with the obtained relaxation parameters (the top right figure) were used to simulate the relaxation of the POPC powder spectra (the bottom figure).

different noise realizations were averaged to establish the confidence intervals. The results are shown in Figures 5.7, 5.8, and 5.9.

Overall, the agreement of the results of these inversion with the model parameters used in generating the test data sets is excellent. An examination of the stability of the inversion in the presence of an increases random noise in the data shows a proportional, non-catastrophic, loss of stability, an evidence of a successful regularization of the inversion problem. A decrease of signal-to-noise ratio (SNR) in the data can be compensated for by an increase in the number of data sets used. For example, inversion results from 32 partially-relaxed spectra spaced by 2ms and starting from 1ms in the presence of 1%, 5%, and 10% noise are given in Figures. 5.10, 5.11, and 5.12; they are comparable to those obtained earlier, from a smaller data set at a higher SNR. Note that experimentally, SNR grows as a square root of the experimental time, while increasing the number of τ values is directly proportional to it.

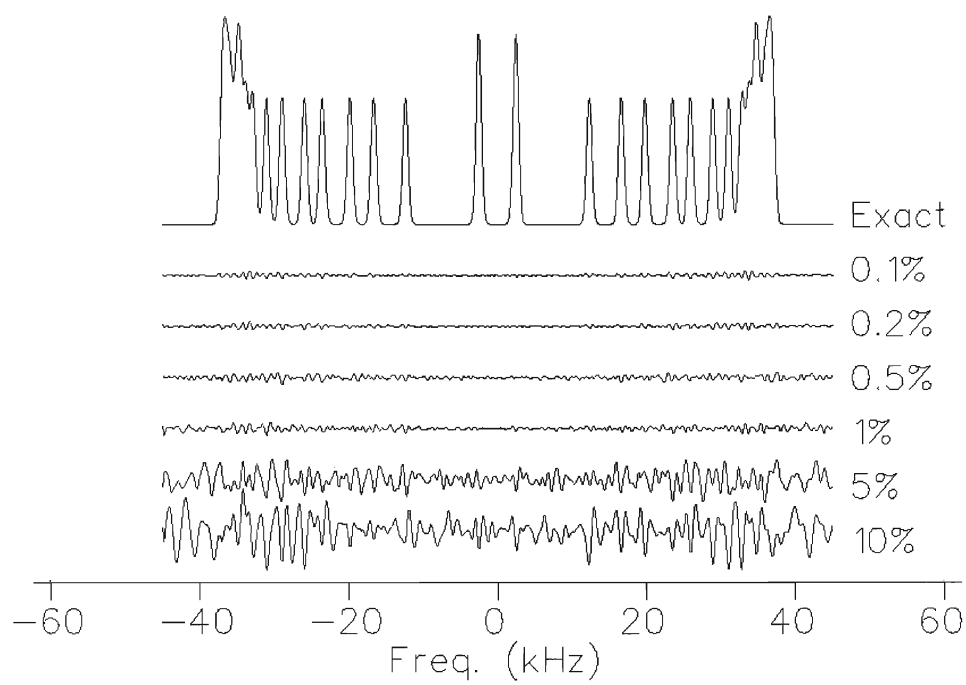

Figure 5.6: **Extracted anisotropy distribution for POPC data set**, the exact anisotropy distribution and the mismatch between the extracted anisotropy distribution and the exact one for six tested noise levels are represented.

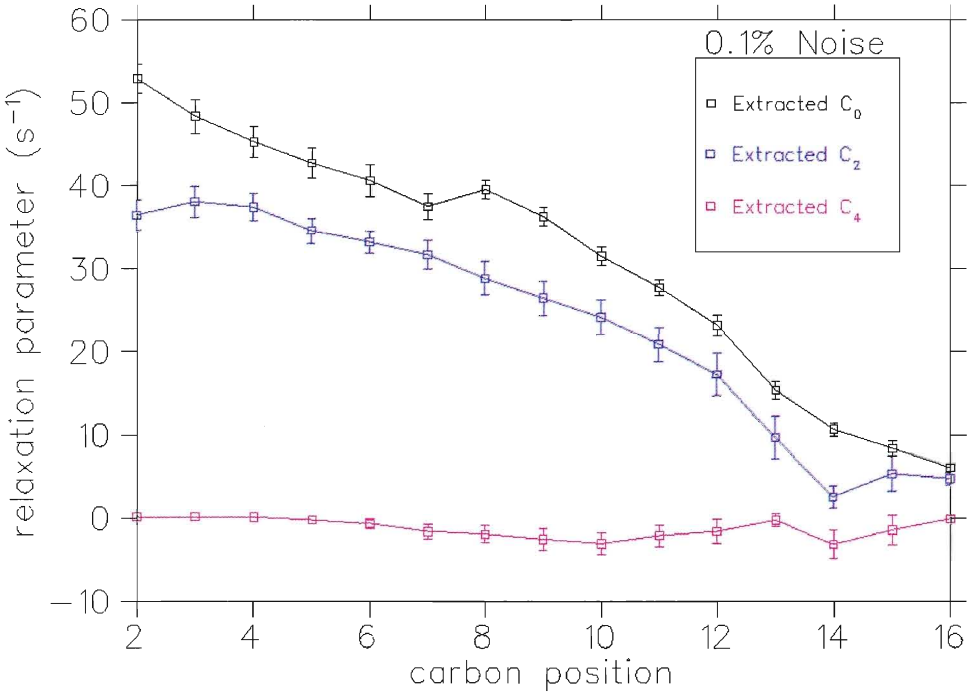

Figure 5.7: **Extracted relaxation parameters from POPC data set in the presence of** 0.1% **noise**, 16 spectra partially-relaxed spectra were used for this noise level.

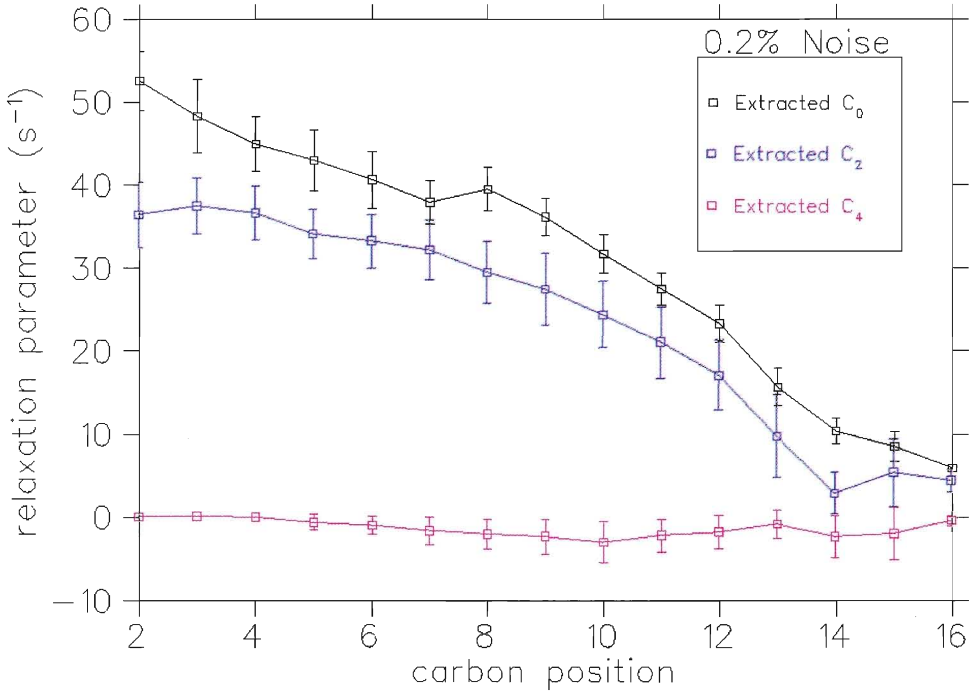

Figure 5.8: **Extracted relaxation parameters from POPC data set in the presence of** 0.2% **noise**, 16 spectra partially-relaxed spectra were used for this noise level.

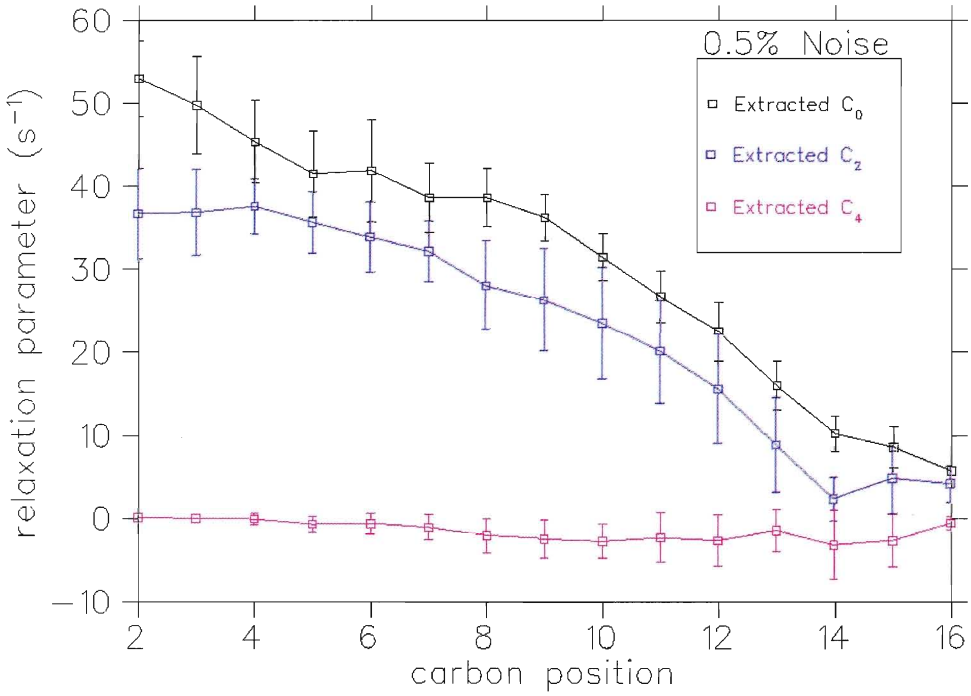

Figure 5.9: **Extracted relaxation parameters from POPC data set in the presence of** 0.5% **noise**, 16 spectra partially-relaxed spectra were used for this noise level.

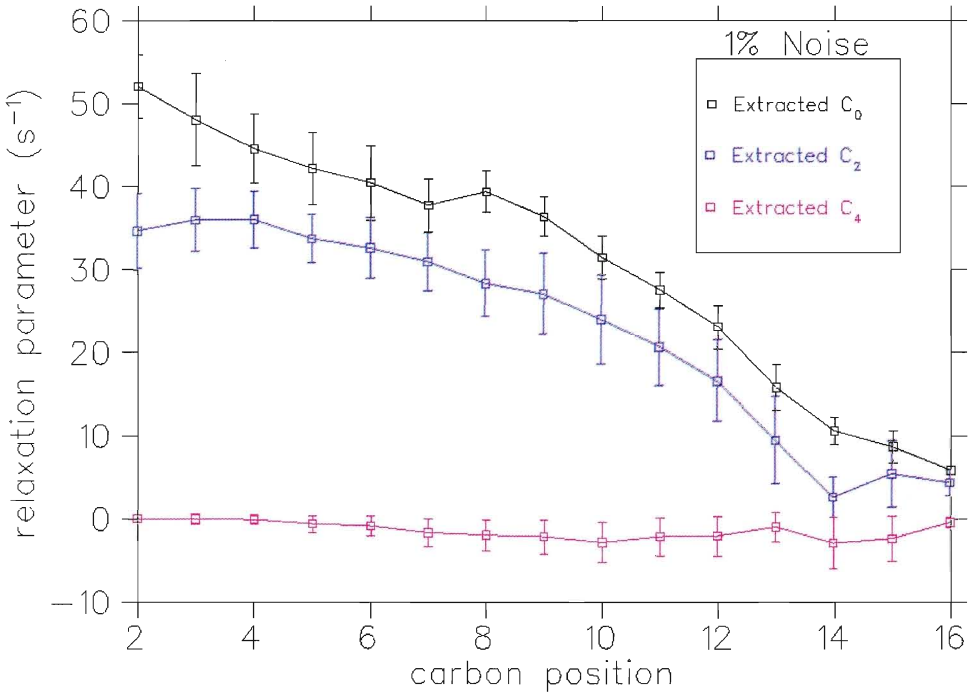

Figure 5.10: **Extracted relaxation parameters from POPC data set in the presence of** 1% **noise**, 32 spectra partially-relaxed spectra were used for this noise level

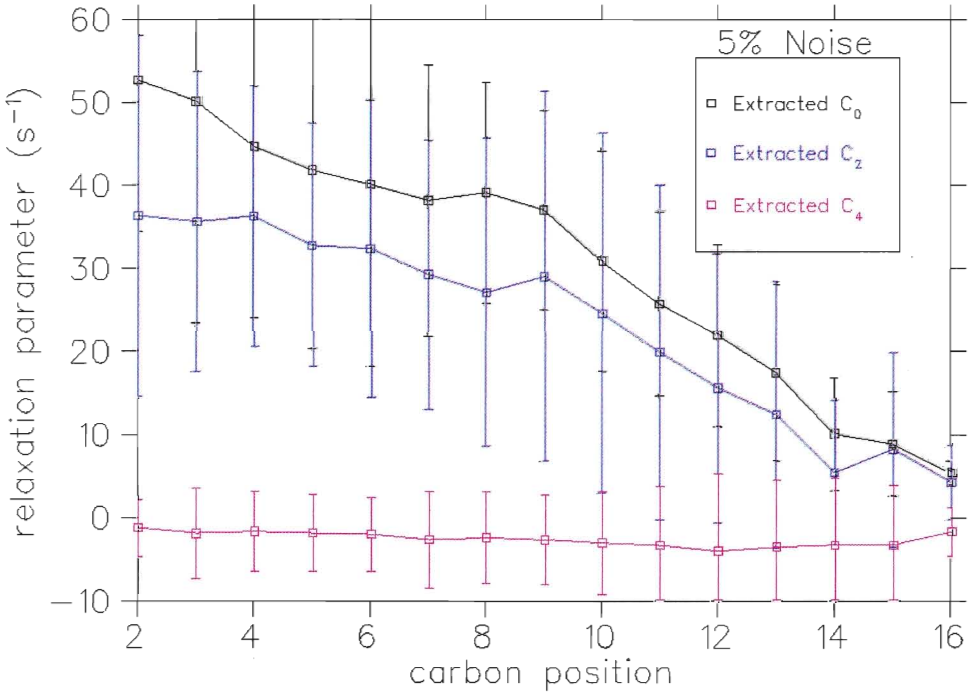

Figure 5.11: **Extracted relaxation parameters from POPC data set in the presence of** 5% **noise**, 32 spectra partially-relaxed spectra were used for this noise level.

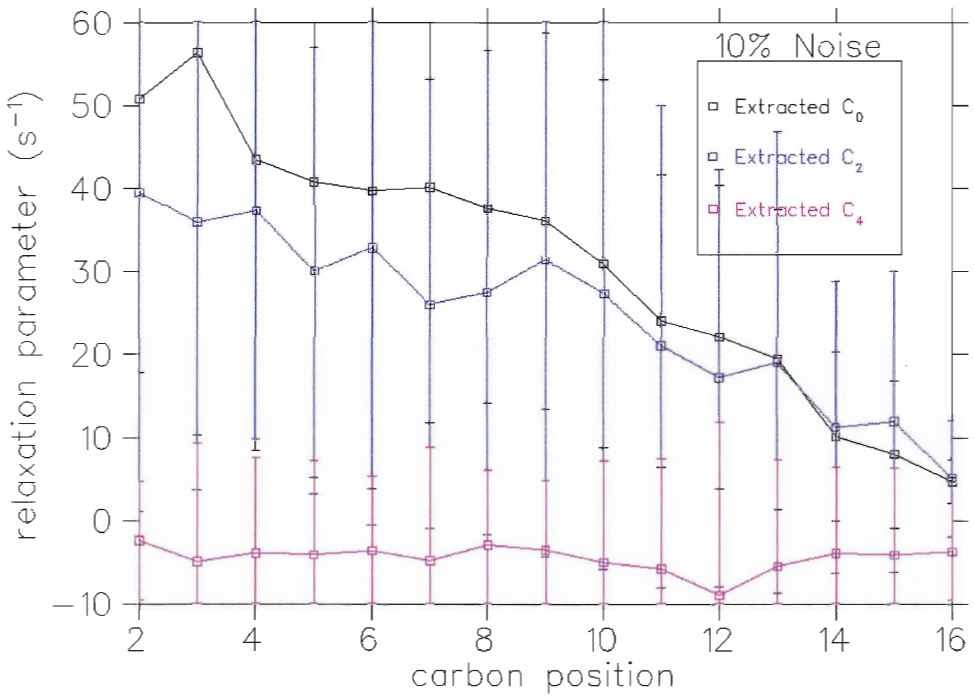

Figure 5.12: **Extracted relaxation parameters from POPC data set in the presence of** 10% **noise**, 32 spectra partially-relaxed spectra were used for this noise level.

Chapter 6

Concluding Remarks

In preceding chapters, the orientation-dependent relaxation phenomenon in deuterium NMR spectra of lipid bilayers was described. Fundamentally, it is the nature of molecular motions that determines the correlation times, spectral densities, and in turn, the observed dependence of relaxation rates on the Larmor frequency, temperature, and the position on the chain. New basis functions for the orientation dependence of the longitudinal relaxation rate, $\frac{1}{T_1}$, under the assumption of the short correlation time regime were introduced. For the purpose of numerical inversion and NMR data analysis, several regularization techniques along with other numerical methods were combined to propose a model-free extraction algorithm based on linearization through interpolation.

It was shown that it is practically possible to tackle numerical difficulties arising from the orientation-dependence of relaxation rates in de-convolving powder spectra and thus to extend the conventional de-Pakeing problem to partially-relaxed NMR powder spectra by deploying appropriate inverse-problem algorithms. The reliability of the proposed extraction algorithm was examined against simulated data based on experimentally measured relaxation rates from oriented bilayer samples of POPC and powder samples of HMB. Although the emphasis of this work was on lipid molecules in the L_α phase, as long as axial symmetry of the EFG tensor and the general features of molecular motions hold, the results remain directly applicable to other systems. This was confirmed in the case of HMB. In addition, since relaxation due to other mechanisms such as dipolar interaction can be cast in exactly the same mathematical form as that of quadrupolar relaxation [53] and the fact that this extraction algorithm is model-free, it can be applied to other relaxation mechanisms as well.

It was found that the accuracy of extracted relaxation rates crucially depends on the noise level, the number of partially-relaxed spectra used as input, the value of the longest observed τ value as compared to the fastest relaxation time, and the number of extracted relaxation parameters being sought. To some extent, the accuracy of estimated relaxation rates can be improved by increasing the number of observed spectra. The overall deviation of results from the exact relaxation parameters due to the regularization error can be diminished by improving the criterion of Eq. 4.16, namely, either by decreasing the value of the longest observed τ value or increasing the number of used partially-relaxed spectra in the extraction. The anisotropy distributions recovered even in the presence of 1% noise are remarkably accurate, and this signifies that the precision essential for extracting experimental relaxation rates has been achieved.

In the course of this project, iterative regularizations based on iteration methods such as CG and Landweber were found less perturbative (compared to Tikhonov and TSVD regularizations) and more efficient which would probably be of great potential interest in future work. These methods are particularly important for their ability of dealing with large-scale problems that may naturally arise in treating other 2D deconvolution problems in NMR. Since they do not rely on SVD and consist of elementary operations, they are immediately implementable in non-matrix-based programming environments.

The newly-developed basis functions for the orientation dependence of the longitudinal relaxation rate differ from conventionally used ones, such as first three even Legendre polynomials. This new basis (Eq. 2.45) emerges naturally from the orientation dependence of the spectral densities under the assumption that the correlation time of motions is very short which is in part justified by the longitudinal relaxation rate of the order of tens of milliseconds. The basis functions in this new basis are not orthogonal, but since the experimentally observed $P_4(\cos\beta)$ is very small (~ 0.03 in HMB), coefficient of compared to those of $P_0(\cos\beta)$ and $P_2(\cos\beta)$, this suggests that the orientation-dependence of relaxation rates has no $\cos^4\beta$ contribution. This of course, is one of the features of the proposed basis, and this indicants confirmation of its suitability is gratifying.

Examination of experimental data lays beyond the scope of this project, but all of the successful numerical testing performed is and assurance that the relaxation parameters extracted from the experimental data will represent the true value of the molecular motion in biomembranes and similar anisotropic systems.

Bibliography

[1] K.F. King M.A Bernstein and X.J. Zhou. *Handbook of MRI Pulse Sequences.* Elsevier Academic Press, San Diego, 2004.

[2] National Institute of Standards and **http://physics.nist.gov** Technology.

[3] D.A. Dougherty E.V. Anslyn. *Modern Physical Organic Chemistry.* University Science Books, Sausalito, California, 2004.

[4] E. Sternin. *Some Mechanisms of Transverse Nuclear Magnetic Relaxation in Model Membranes.* PhD thesis, University of British Columbia, 1988.

[5] M.F. Brown and J. Seelig. *J. Chem. Phys.*, 70:5045–5053, 1978.

[6] M.F. Brown. *J. Chem. Phys.*, 77:1576–1562, 1982.

[7] M.F. Brown. *J. Chem. Phys.*, 80:2832–2836, 1983.

[8] T.L. James. *Nuclear Magnetic Resonance in Biochemistry: Principles and Applications.* Academic Press, New York, 1975.

[9] E. Sternin. *A Chapter for Membrane Lipid Protocols.* Humana Press, Inc., 2005.

[10] J. Seelig. *Q. Rev. Biophys.*, 3:353–418, 1977.

[11] G.N. Nicholoson S.J. Singer. *Science*, 175:720–731, 1972.

[12] S.V. Dvinskikh C. Hgberg A.P. Lyubartsev H. Zimmermann D. Sandstrm V. Castro, B. Stevensson and A. Maliniak. *Biochim. Biophys. Acta.*, 1778:2604–2611, 2008.

[13] A.R. Martin F.L. Rose G.E. Davies, J. Francis and G. Swain. *Brit. J. Pharmacol.*, 9:192–196, 1954.

[14] **http://www.avantilipids.com**.

[15] **http://www.chem.ucalgary.ca/research/groups/rauk/index.html**.

[16] B. Klsgen. *Conformation of Fluid Lipid Membranes. In: Lipid bilayers: structure, fluctuation and interaction.* Springer, New York, 2000.

[17] P.R. Bergethon. *The Physical Basis of Biochemistry.* Springer, New York, 1998.

[18] D. Rognan G. Folkers H. Hltje, W. Sippl. *Molecular Modeling.* WILEY-VCH GmbH & Co. KGaA, Weinheim, 2003.

[19] D. A. Grabowski J. Honerkamp S. Muller J. Winterhalter, D. Maier and C. Schmidt. *J. of Chem. Phys.*, 110:4035–4046, 1999.

[20] M. Bloom K.T. Whittall, E. Sternin and A. McKay. *J. Magn. Reson.*, 84:64–71, 1989.

[21] M. Bloom E. Sternin and A. McKay. *J. Magn. Reson.*, 55:274–282, 1983.

[22] B. Mdler H. Schfer and F. Volke. *J. Magn. Reson.*, 116:145–149, 1995.

[23] M. Bloom H. Schfer, B. Mdler and E. Sternin. *Biophys. J.*, 74:1007–1014, 1998.

[24] C. Morrison. *Theory of the General Orientation Dependence of ^2H NMR Spin-Lattice Relaxation and Experiments on Model Membranes.* PhD thesis, University of British Columbia, 1993.

[25] T.D.W. Claridge. *High-Resolution NMR Techniques in Organic Chemistry.* Elsevier, Oxford, 2009.

[26] M.H. Levitt. *Spin Dynamics.* John Wiely & Sons, West Sussex, 2001.

[27] C.P. Slichter. *Principles of Magnetic Resonance.* Springer-Verlag, New York, 1990.

[28] K. Schmidt-Rohr and H.W. Spiess. *Multidimensional Solid-State NMR and Polymers.* Academic Press, San Diego, 1994.

[29] L.C. Biedenharn and J.D. Louck. *Angular Momentum in Quantum Physics.* Addison-Wesley, 1981.

[30] A. Abragam. *The Principles of Nuclear Magnetism.* Oxford University Press, London, 1961.

[31] M. Goldman. *J. Magn. Reson.*, 149:160–187, 2001.

[32] B. Fain. *Irreversibilities in Quantum Mechanics.* Kluwer Acadamic Publisher, New York, 2002.

[33] K.R. Jeffrey. *Bulletin of Magnetic Resonance.*, 3:69–82, 1981.

[34] M.F. Brown. *J. Magn. Reson.*, 35:203–215, 1978.

[35] U. Henriksson M.F. Brown, A. Salmon and O. Soderman. *Molecular Physics*, 69:379–383, 1990.

[36] B. Halle. *J. Phys. Chem.*, 95:6724–6733, 1991.

[37] T.M. Alam T.P. Trouard and M.F. Brown. *J. Chem. Phys.*, 101:5229?5261, 1994.

[38] B. Cornell F. Separovic and R. Pace. *Chemistry and Physics of Lipids*, 107:159–167, 2000.

[39] J.C. Santamarina and D. Fratta. *Discrete Signals and Inverse Problems.* John Wiley & Sons, West Sussex, 2005.

[40] V.Y. Arsenin A.N. Tikhonov. *Solutions of Ill-Posed Problems.* Winston, New York, 1977.

[41] J. Hadamard. *Lectures of the Cauchy Problem in Linear Partial Differential Equation, Vol. 3.* Yale University Press, New Haven, 1923.

[42] P.C. Hansen. *Rank-Deficient and Discrete Ill-Posed Problems.* Siam, Philadelphia, 1998.

[43] C.R. Vogel. *Computational Methods for Ill-Posed Problems.* Siam, Philadelphia, 2002.

[44] D.P. O'Leary P.C. Hansen. *SIAM J. on Sci. Comput.*, 14:1487–1503, 1993.

[45] M. Hanke W. Engl and A. Neubauer. *Regularization of inverse problems.* Kluwer Academic Publisher, Boston, 1996.

[46] M.R. Hestenes and E. Stiefel. *J. of Res. of the Nat. Bur. of Stand.*, 49:409–436, 1952.

[47] B. Mdler H. Schfer and E. Sternin. *Biophys. J.*, 74:1007–1014, 1998.

[48] G. Dahlquist and A. Bjorck. *Numerical Methods in Scientific Computing, Volum I.* Siam, Philadelphia, 2008.

[49] A. Bjorck. *Numerical Methods for Least Squares Problems.* Siam, Philadelphia, 1996.

[50] **http://www.scilab.org/** .

[51] P. Rignell. *An experimental study of the General Orientation Dependence of Spin-Lattice Relaxation Rates in a spin 1 single crystal system of HMB.* PhD thesis, University of British Columbia, 1994.

[52] L. Sterna J. Tang and A. Pines. *J. Magn. Reson.*, 41:389–394, 1980.

[53] D.A. Torchia and A. Szabo. *J. Magn. Reson.*, 49:107–121, 1982.